Doctoral School in Cognitive and Brain Sciences

Universita' Degli Studi Di Trento

GRAY MATTER COVARIANCE NETWORKS IN THE MOUSE BRAIN

Marco Pagani

Center for Neuroscience and Cognitive Systems,

Istituto Italiano di Tecnologia

Advisors:

Alessandro Gozzi

Angelo Bifone

a mamma e papà, come sempre

“Faber est suae quisque fortunae”

Gaio Sallustio Crispo (86-34 a.C.)

Declaration of authorship.

I confirm that this is my own work and the use of all material from other sources has been properly and fully acknowledged.

Table of Contents

Acknowledgments

The project presented in this thesis would have never been possible without the precious contribution of those who provided invaluable support and insights into the MRI investigations I carried out during my PhD course. Thank you very much for all the time, energy and competence you all have dedicated to these studies, and in general, to guiding me on my path in neuroimaging with MRI.

First of all, I would like to express my sincere gratitude to my two advisors, for being stimulating and always open to discuss data, methods and results. In particular, I thank **Alessandro Gozzi** who offered me the opportunity to develop this and other research projects in his group, in a friendly and inspiring working atmosphere, from the very first days when I joined the Functional Neuroimaging Laboratory. With passion, constancy and ability, he followed the development of this work and he guided me to deal with the extremely intriguing and complex field of mouse brain imaging. For these and many other reasons, I am genuinely excited to continue facing the fascinating challenges of investigating connectivity alterations in autism during my post-doc under his supervision. In the same way, I thank **Angelo Bifone** for giving solid theoretical and methodological inputs to the project, but also for providing financial support throughout the duration of my PhD. I would also like to express my gratitude to **Lorella Battelli** and **Stefano Panzeri** who were part of the multi-disciplinary oversight committee that provided precious feedbacks on my work.

Among the lab members, I thank all current and former colleagues, Post-docs, Phd and Master students who shared these three years of passionate MRI research with me. Special thanks go to **Alberto Galbusera** for his tireless commitment in acquiring the vast majority of the data presented in this work. I am also grateful to **Adam Liska**, **Daniel Gutierrez** and **Manuel Blesa** for providing a never-ending source of constructive ideas, concepts and points of view on complementary imaging modalities, but also

to **Alessia de Felice**, **Carola Canella**, **Anna Aksiuto**, **Nayome Rey Calvo**, **Gergely David**, **Taufiq Naseef** and **Camilla Robol** for being supporting colleagues and friends.

Of course, my biggest thanks to my family Angela, Roberto, Fabio and Alessandra and all the close relatives and friends I have in Saronno, Milano, Rovereto and Altavilla Milicia for making my life so extraordinary.

List of Abbreviations

AAL: Automated Anatomical Labelling

ANTs: Advanced Normalization Tools

B6: C57BL/6J Mouse Strain

BTBR: BTBR T+Itpr3tf/J Mouse Strain

DiReCT: Diffeomorphic Registration Based Cortical Thickness

Cb: Cerebellum

CC: Corpus Callosum

Cpu: Caudoputamen

CSF: Cerebrospinal Fluid

DHyp: Dorsal Hypothalamus

dPFC: Dorsal Prefrontal Cortex

EPM: Elevated Plus Maze

FSL: FMRIB Software Library

FLASH: Fast Low Angle Shot

GM: Gray Matter

HPC: Hippocampus

Hyp: Hypothalamus

ICA: Independent Component Analysis

ITI: Inter-Trial Interval

LTh: Lateral Thalamus

mPFC: Medial Prefrontal Cortex

M1: Primary Motor Cortex

MRI: Magnetic Resonance Imaging

MWM: Morris Water Maze

n3-PUFA: Omega-3 Polyunsaturated Fatty Acid

OB: Olfactory Bulbs

OF: Orbitofrontal Cortex

PFA: Paraformaldehyde

RARE: Rapid Acquisition with Relaxation Enhancement

Rh: Rhinal Cortex

RS: Retrosplenial Cortex

rs-fMRI: Resting State Functional Magnetic Resonance Imaging

scMRI: Structural Covariance Magnetic Resonance Imaging

SPM: Statistical Parametric Mapping

SyN: Symmetric Image Normalization

T2W: T2 weighted

TBM: Tensor Based Morphometry

Th: Thalamus

V1: Primary Visual Cortex

VBM: Voxel Based Morphometry

WM: White Matter

Abstract

The presence of networks of correlation between gray matter volumes of brain regions - as measured across subjects in a group of individuals - has been consistently described in several human studies, an approach termed structural covariance MRI (scMRI). Complementary to prevalent brain connectivity modalities like functional and diffusion-weighted imaging, this approach can provide valuable insight into the mutual influence of regional trophic and plastic processes occurring between brain regions.

Previous investigations highlighted coordinated growth of these regions within specific structural networks in healthy populations and described their derangement in pathological states. However, a number of fundamental questions about the origin and significance of these couplings remains open and the mechanisms behind the formation of scMRI networks are still poorly understood. To investigate whether analogous scMRI networks are present in lower mammal species amenable to genetic and experimental manipulation such as the laboratory mouse, I coupled high resolution morpho-anatomical MRI with network-based approaches on a large cohort of genetically-homogeneous wild-type mice (C57Bl6/J). To this purpose, I first developed a semi-automated pipeline enabling reliable Voxel Based Morphometry (VBM) of gray matter volumes in the mouse. To validate this approach and its ability to detect plastic changes in brain structures, I applied it to a cohort of aged mice treated with omega-3 polyunsaturated fatty acids (n3-PUFA). This study revealed that treatment with n3PUFA, but not isocaloric olive oil preserved gray matter volume of the hippocampus and frontal cortices, an effect coincident with amelioration of hippocampal-based spatial memory functions. I next employed VBM to investigate scMRI networks in inbred mice using a seed-based approach. In striking resemblance with human findings, I observed the presence of homotopic (i.e. bilateral)

architecture in several scMRI cortical and subcortical networks, a finding corroborated by Independent Component Analyses. Subcortical structures also showed highly symmetric inter-hemispheric correlations, with evidence of distributed antero-posterior networks in diencephalic regions of the thalamus and hypothalamus. Hierarchical cluster analysis revealed six identifiable clusters of cortical and sub-cortical regions corresponding to previously described neuroanatomical systems. This work documents for the first time the presence of homotopic cortical and subcortical scMRI networks in the mouse brain, and is poised to pave the way to translational use of this species to investigate the elusive biological and neuroanatomical underpinnings of scMRI network development and its derangement in neuropathological states.

Keywords

Structural Covariance Networks; Magnetic Resonance Imaging, Voxel Based Morphometry, Mouse Brain

1. Structural Covariance Networks of the Brain

1.1. Background

“Segregation” vs “integration” represents a long-standing controversy that has polarized neuroscientists in opposite and complementary views in the challenge of studying, modelling and explaining the structural and functional architecture of the human brain. On the one hand, the theory of segregation emphasizes the role of highly specialized brain areas - i.e. the brain has different modules that are specialized for different functions. By contrast, the theory of interactionism stresses the role of communication between brain units to produce organized and integrated networks that underlie virtually unlimited brain states and behaviors.

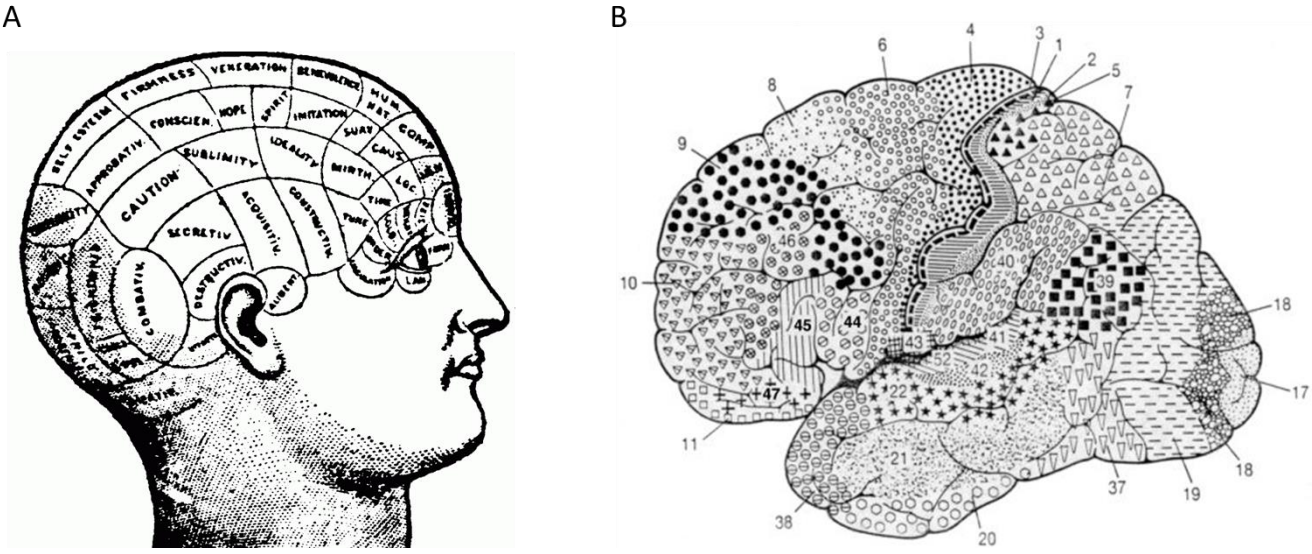

Figure 1. From phrenology to cytoarchitecture. *According to phrenology, character and emotions were located in specific districts of the brain (A). After one century, Brodmann classified the cerebral cortex in regions defined by their histological compositions and cell organization (B).*

Historically, early contributions had the merit of shedding light on the functional specialization of brain areas. For example, Franz Joseph Gall associated the uneven geography of the skull to the pressure exerted from more developed brain districts (Gall, 1818). Although this naïve

theory had no scientific basis, it prepared the ground for following studies aimed at mapping "which part of the brain does what". A first step towards this direction was made by the French neurologist Paul Broca, who identified the anatomical localization of a highly specialized brain function like the language by post-mortem studies on patients with aphasia (Broca,1865). Also, the studies of Korbinian Brodmann (Brodmann 1909) were fundamental to postulate an association between histological properties of the cortex and brain functions (**Figure 1**). Throughout the twentieth century, these early findings gave a great impulse to modern neuroscience that, in turns, provided unparalleled amount of evidence on the association between single neuroanatomical substrates and brain functions.

However, it is now clear that the brain does not work as a segregated collection of single units and the simple one-to-one correspondence between structure and function is not sufficient to explain its enormous complexity. For example, although the application of brain mapping techniques on patients produced a tremendous quantity of data both in healthy and patient populations, the etiology and neurobiology of brain disorders is far from being convincingly described in terms of regional dysfunction. The increasing awareness of these intrinsic methodological limitations shifted the perspective of the scientific community, spurring the development of integrative approaches aimed at describing the brain's structural and functional connectivity. According to this view, the interplay within and among highly specialized areas is mediated by connections, intended as a pattern of anatomical links or statistical dependencies among distinct specialized units. From the micro to the macroscale, the units may correspond to individual neurons, populations of neurons, or entire brain regions. Connectivity patterns are constituted by structural links such as synapses or fiber pathways, or may represent statistical/causal relationships between the activity of neurons or synchronized spontaneous blood fluctuations among brain regions.

Many of these conceptual advancements have been made possible by the usage of non-invasive neuroimaging techniques like magnetic resonance imaging (MRI), which allow to obtain high-resolution three-dimensional reconstructions of the brain. Since their advent, MRI-based methods have emerged as valuable tools to study the topology of the brain and the elusive interplay between segregation and integration (Bullmore and Sporns 2009). To date, the vast majority of MRI mapping of brain connectivity is based on two main techniques, diffusion weighted MRI and resting state functional MRI. Diffusion weighted MRI (**Figure 2**) is a technique that exploits the anisotropic diffusion of water molecules in myelinated fibers to map the organization of white matter pathways connecting different brain districts.

Figure 2. White matter fiber architecture of the brain. *Diffusion MRI is sensitive to water molecules that diffuse preferentially along fiber tracts, i.e. groups of axons. Different from post-mortem dissection and chemical tracing, that are still the gold standard for the identification of axonal connections, diffusion MRI provides information about the position and the integrity of fiber tracts in vivo. Fibers with similar orientation are shown in the same color (http://www.humanconnectomeproject.org).*

Resting state functional MRI is based on statistically correlated low frequency hemodynamic

fluctuations between brain regions and is used to map the functional architecture of the brain in no task conditions.

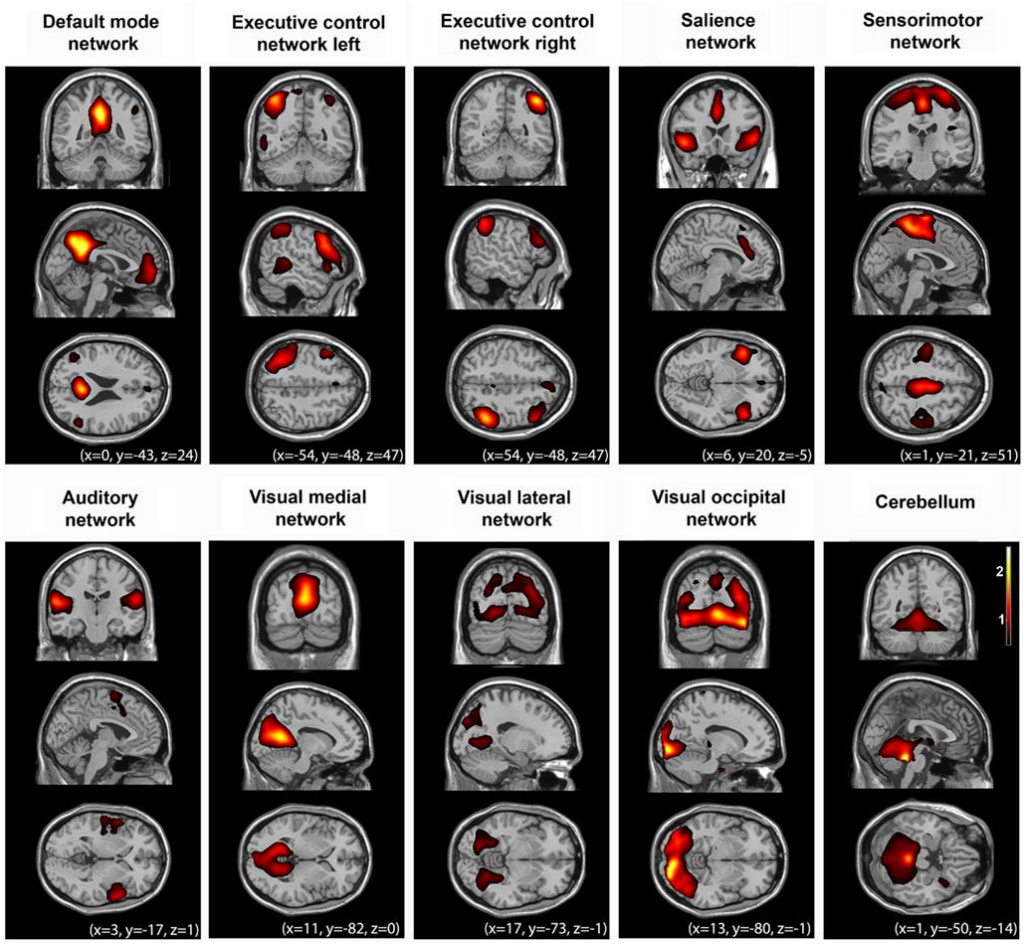

Figure 3. Multiple cerebral networks can be identified with functional MRI in healthy subjects during resting state. *In healthy subjects performing no specific task ("resting state"), time courses of voxels within functionally connected regions of the brain exhibit high correlation coefficients. These networks reflect "higher-order" cognitive (i.e., default mode, left and right executive control, salience networks), and "lower-order" sensorimotor, and sensory (i.e. auditory, visual) function. (Heine, Soddu et al. 2012).*

Importantly, MRI is highly versatile and these two popular modalities have been recently complemented by a novel class of measurements that provide an alternative index of coupling between brain areas at the population level. The main idea behind these measurements is that regions that are anatomically connected could express structural covariance in their growth

dynamics (Mechelli, Friston et al. 2005). According to this hypothesis, inter-individual differences in size (or thickness) of a brain region could have a statistical association with inter-individual differences in size (or thickness) of other brain regions across subjects. Intuitively, a simple but robust approach to probe the existence of structural covariance is to assess the correlation between the size of one brain region and that of another brain region in a population of subjects. For instance, if a significant correlation between the size of the left and right motor cortex was observed in a population of subjects, we could infer that these two regions exhibit coordinated growth dynamics and then are part of the same anatomical or structural covariance (scMRI) network (**Figure 4**). The presence of this sort of coupling could thus expand the concept of brain connectivity by incorporating population level trophic influences that gray matter regions such as the cortex, basal ganglia and hippocampus exhibit on each other and then complement white matter-based (e.g. DTI) or hemodynamic based measurements of connectivity.

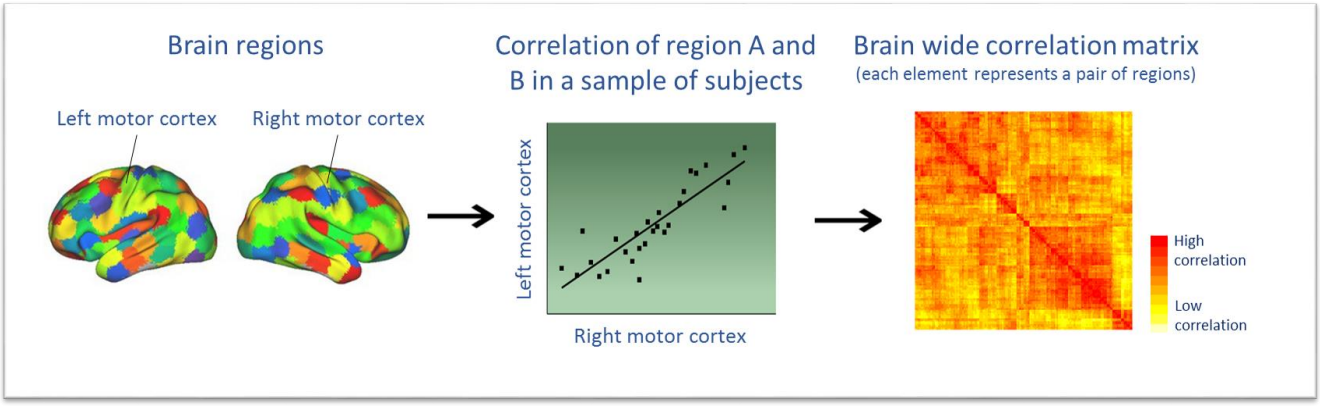

Figure 4. Structural covariance (scMRI) networks of the human brain. *If we find a statistical association between the size of two brain regions, for example between the left and the right motor cortex, in a population of subjects, these two brain districts show a coordinated volumetric expansion or contraction and therefore constitutes two units of a scMRI network. Commonly, the linear dependence between these two datasets is expressed by the Pearson's correlation coefficient, although independent component analysis, graphs and cluster analysis could be used.*

The existence of scMRI coupling in humans was proved in a seminal study carried out on a large cohort of healthy subjects (Mechelli, Friston et al. 2005), where robust patterns of positive correlation were identified between mean gray matter volumes of primary sensory-motor, emotional and cognitive areas, and their homotopic regions in the contralateral hemisphere. Symmetric patterns were consistently observed in males and females, with gender related brain asymmetries limited only to the amygdalar network (**Figure 5**).

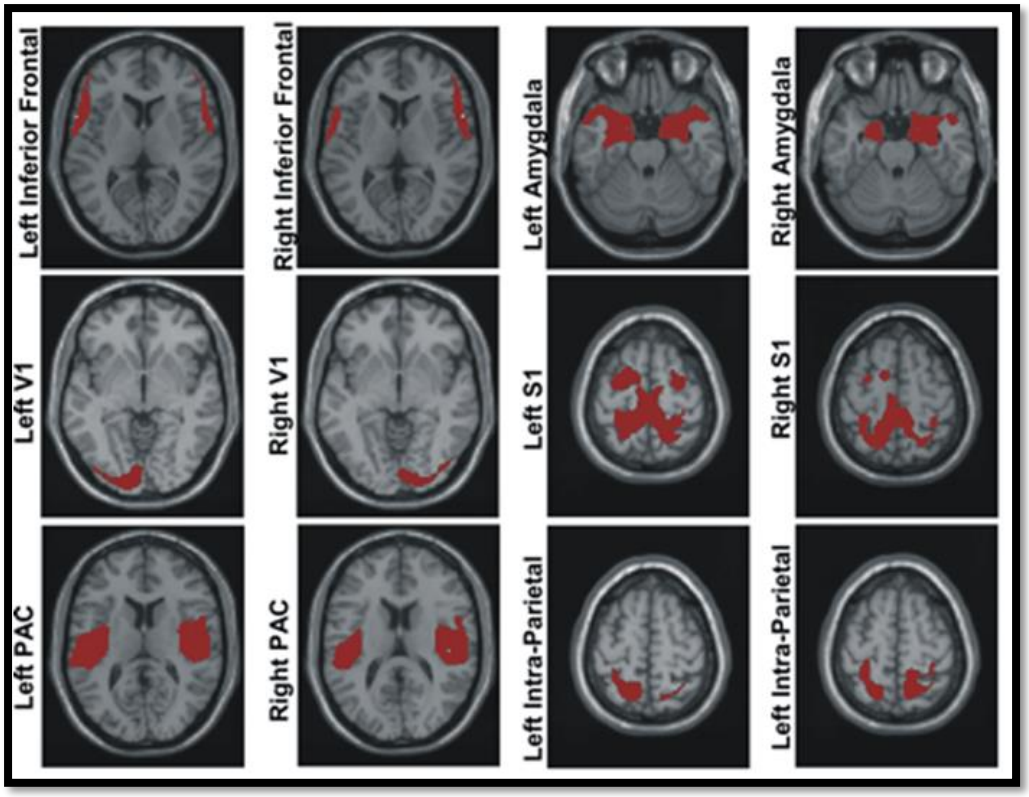

Figure 5. Homotopic scMRI in the healthy population. *Seed based analysis revealed for the first time in the literature the existence of homotopic scMRI networks between 12 regions of interest and their mirror regions in the contralateral hemisphere (Mechelli, Friston et al. 2005).*

Since its description, scMRI has been employed by a number of investigators who have provided an important source of information about inter-regional connectivity (Alexander-Bloch, Raznahan et al. 2013). While the determinants underlying the establishment and distribution of structural covariance networks remain still poorly understood, a role of genetic,

developmental, aging and experience related plasticity has been described by previous investigations (Mechelli, Friston et al. 2005, Evans 2013).

Covariance between brain regions was first described within the visual (Andrews, Halpern et al. 1997) and motor (White, Andrews et al. 1997) systems in early *post mortem* studies. However, the extensive usage of computer-automated analysis of morphoanatomical MRI has multiple advantages compared to *post mortem* studies and provided valuable insights in the understanding of structural covariance. In particular, MRI enables *in vivo* investigation of gray matter networks, it can be carry out on a multitude of individuals in a relatively limited time, and it also allows the investigation of these networks at high-resolution and on multiple brain regions (Alexander-Bloch, Raznahan et al. 2013).

Exploiting these advantages of MRI, an increasing amount of findings have been produced on structural connectivity, suggesting a consistent degree of overlap between scMRI networks and cognitive functions. For instance, the gray matter volume of the hippocampus showed significant correlations with that of the contralateral hippocampus, amygdala, rhinal and orbitofrontal cortices, a set of brain regions involved in memory and spatial navigation tasks. Moreover, studies on emotion and empathic responses produced evidence of extensive correlations between the thickness of anterior insula and multiple regions within the cerebral mantle (Bernhardt, 2013). Albaugh and colleagues (Albaugh, Ducharme et al. 2013) described a network of cortical regions, including prefrontal, orbitofrontal and parietal cortices, whose thickness was anti-correlated with the volume of the amygdala. Altogether, these results provide evidence of scMRI coupling among brain regions involved in emotion regulation. Further, anterior and posterior areas devoted to the processing of language in the left hemisphere were found to be strongly correlated in terms of cortical thickness (Lerch, 2006). Even though a relation between covariance patterns and functional-cognitive systems in the

brain has been reported in the literature, only very few studies have investigated the establishment and evolution of scMRI networks from a neuro-developmental perspective. One study monitored the growth trajectory of normally developing cohort of subjects across childhood and adolescence (Zielinski, 2010), reporting early development of primary sensory and motor networks and their overexpansion during early adolescence, with a subsequent reduction to the extent of the adult scMRI patterns (**Figure 6**).

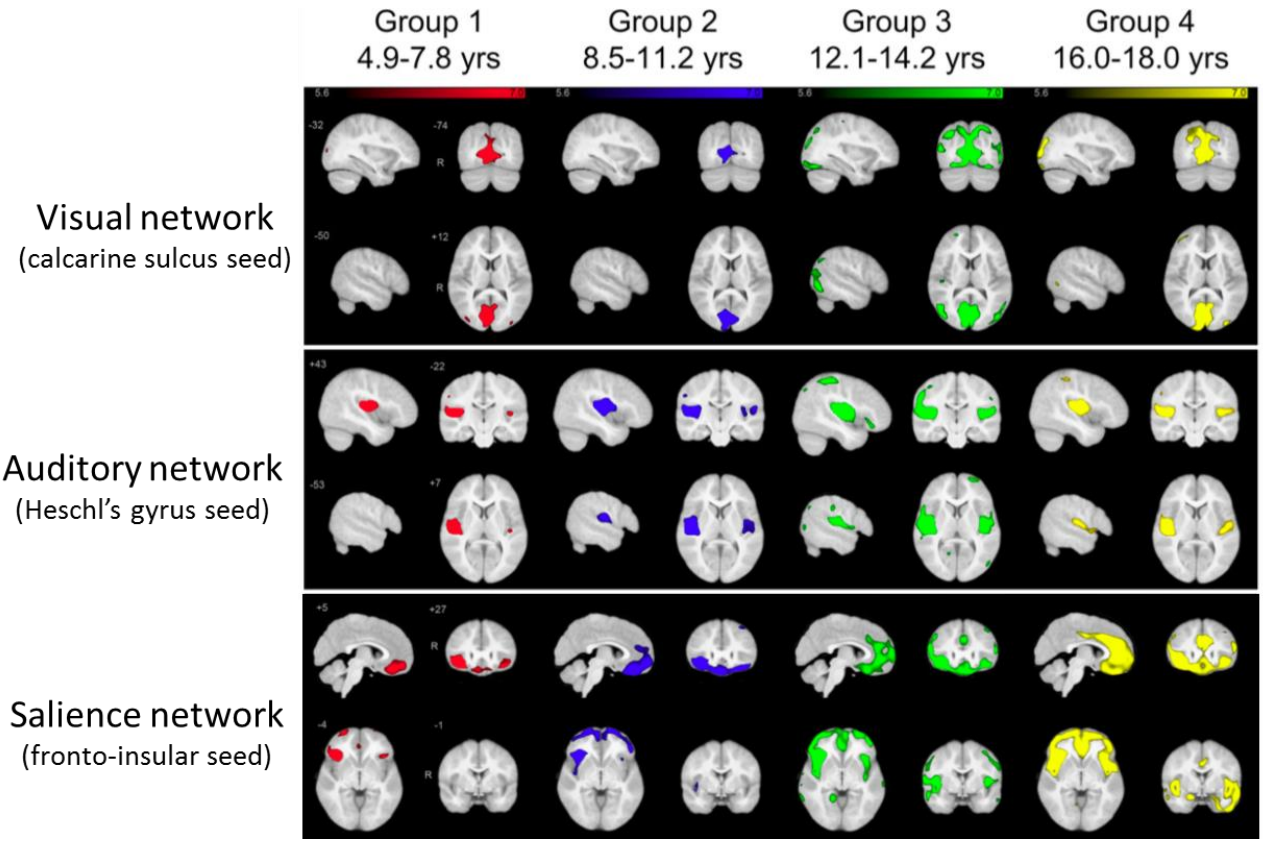

Figure 6. Development of scMRI networks in children and adolescents. *Visual, auditory and other sensory-motor scMRI networks are already well developed in early childhood and expands in early adolescence before pruning to a more restricted topology resembling adult intrinsic connectivity network patterns. In contrast, cognitive scMRI networks - including the homolog of the functional salience network - are not fully developed in children and mature to an adult distributed topology only during adolescence (Zielinski, 2010).*

On the other hand, language, social, emotional and cognitive networks were found to be

underdeveloped in early childhood and exhibited increasingly distributed topology in older children (Zielinski, Gennatas et al. 2010). Also, the findings of later studies support the hypothesis that across-subjects structural correlation between anatomical regions may reflect to a certain extent longitudinal maturational trajectories of those regions, as measured by change of volume across development as the age increase (Alexander-Bloch, Raznahan et al. 2013). This observation is of particular importance in the interpretation of results produced in cross-sectional studies because it is in line with the view that regions that are correlated in size across-subjects, also show a volumetric correlation during development (**Figure 7**).

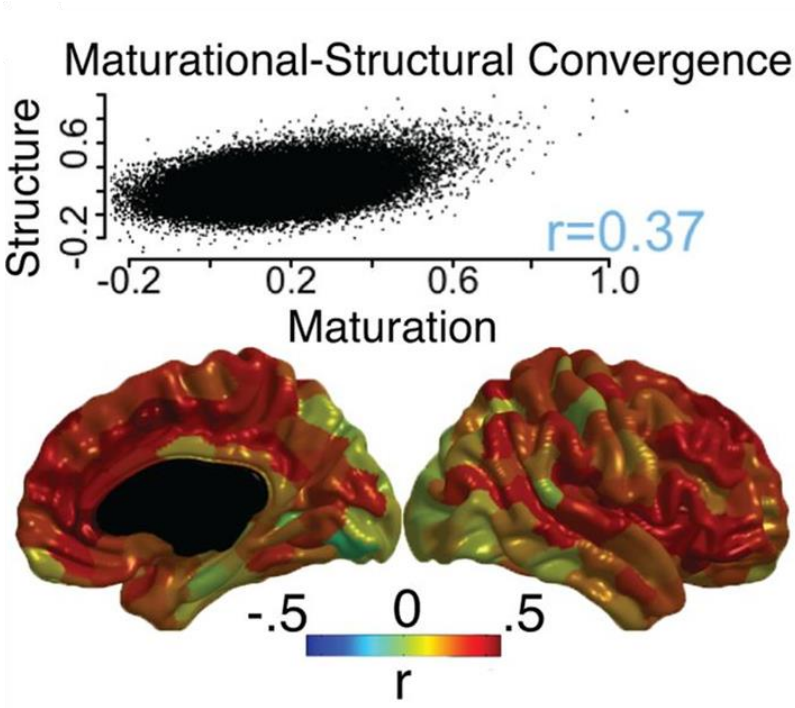

Figure 7. Association between scMRI, maturational coupling, and functional connectivity. *The correlation between scMRI and maturational coupling, across all pairs of brain regions (scatterplot) and for each region separately (Alexander-Bloch et al., 2013).*

Intriguingly, the architecture of structurally based networks was found to partially overlap with well-known functionally defined brain networks (He, Chen et al. 2007, Zielinski, Gennatas et al. 2010, Zielinski, Anderson et al. 2012), supporting the view that the architectural organization of

gray matter scMRI between brain structures reflects functional connectivity. For example, a distributed network of regions co-varying with the volume of the posterior cingulate cortex was found (He, Chen et al. 2008, Zielinski, Gennatas et al. 2010) closely resembling the functional default mode network described by Greicius (2003). Also, an anatomical homolog of the functional salience network (Seeley et al., 2007) was recently identified (Zielinski, Anderson et al. 2012).

Further, clustering of the insula into sub-regions revealed overlapping boundaries when the clustering is based either on task free functional connectivity or on grey matter scMRI, suggesting the intriguing hypothesis that functional coupling may somewhat reflect structural covariance (Kelly, Toro et al. 2012). The correspondence between brain structural and functional networks is in line with results obtained with graph analysis that reported a strong convergence of scMRI and resting state functional connectivity, especially in terms of global efficiency (Alexander-Bloch et al., 2013). However, a recent study challenges this view and suggests that rs-fMRI and scMRI likely capture different aspects of brain function and maturation, since the degree of correspondence between the two modalities varies considerably across seed regions (Reid, Hoffstaedter et al. 2016). These discrepancies call for additional research into the determinants of this phenomenon and its relationship with functional network coupling.

Recently, scMRI has also been applied to clinical populations and offered initial insights into the abnormal structural organization of scMRI networks in brain disorders. Two recent studies on autism spectrum disorders report a reduced extension of the structural salience network of autistic patients (Zielinski, 2012) (**Figure 8**) and decreased covariance in the autistic group relative to controls (Valk, Di Martino et al. 2015), corroborating the current view that autism is a “connectivity disorder”.

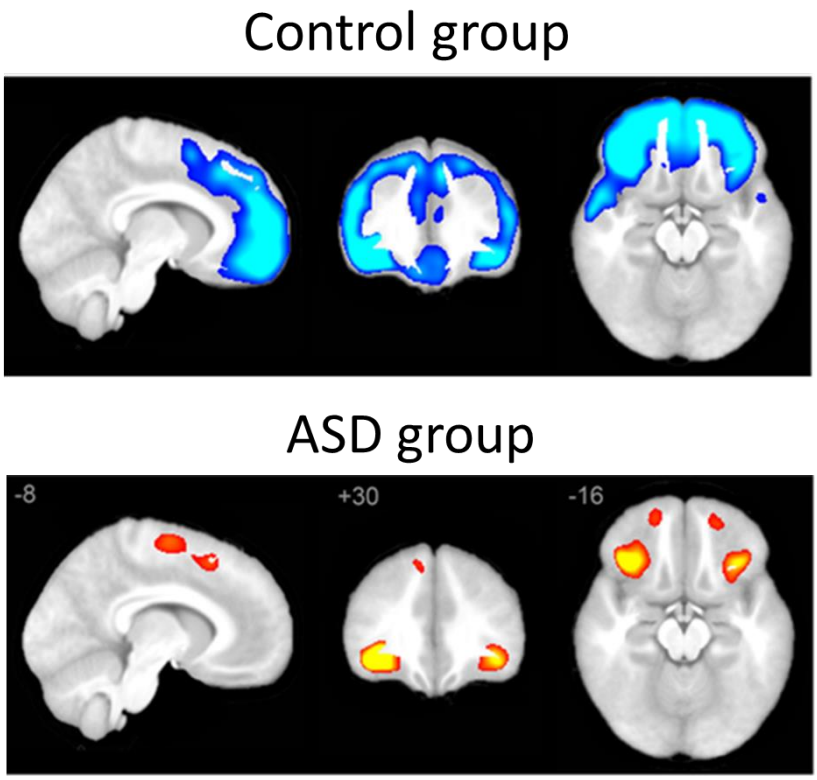

Figure 8. scMRI maps of the structural homolog of the salience network in autism and controls. *Autistic patients exhibit reduced structural covariance patterns in the sc-MRI salience network (Zielinski, Anderson et al. 2012).*

A more recent study also suggests the application of scMRI networks to identify specific patterns of reduced gray matter volume in patients with frequent auditory verbal hallucinations compared to non-hallucinating schizophrenic patients (Kubera, Sambataro et al. 2014). In Alzheimer's disease, patients showed decreased scMRI between homotopic parietal regions and increased correlations compared to healthy controls in several other regions, including temporal, cingulate and medial frontal cortex (He, Chen et al. 2008). These initial studies highlight the possibility of using scMRI networks as population based signature of brain disorders and development which can complement univariate regional mapping.

1.2. Can We Map Structural Covariance Networks in the Mouse?

The application of scMRI has generated new insights on the trophic development of gray matter

correlations between brain regions in healthy and diseased populations. However, a number of fundamental questions about the origin and significance of these networks remains open and the mechanisms behind the formation of scMRI networks are still poorly understood, also due to the impossibility to employ interventional approaches to causally probe the emergence of these correlated response in human populations.

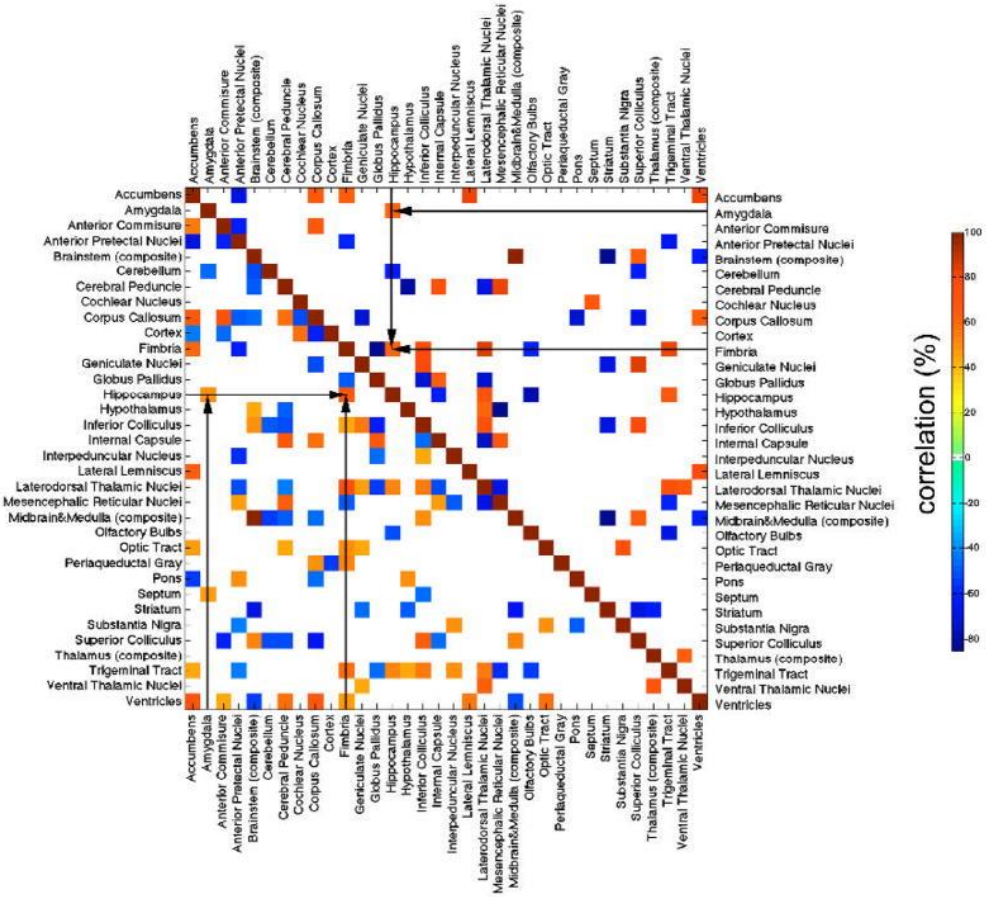

Figure 9. Preliminary description of scMRI networks in the mouse brain. *Significant volumetric correlations were described among components of the limbic system, including hippocampus, amygdala and fimbria in the BXD mouse strain. The area under the diagonal illustrates the cross-correlation map for (N=22) individuals (Badea, Johnson et al. 2009).*

For example, recent evidence has linked genetic polymorphisms with the development of specific functional and anatomical networks (Pezawas, Meyer-Lindenberg et al. 2005),

however, the genetic determinants underlying the emergence of these networks remain poorly understood. Moreover, although correlations between cortical gray matter thickness and structural connectivity have been described (Lerch, Worsley et al. 2006), with recent estimates suggesting that white matter MRI connectivity explains approximately 35–40% of the thickness correlations across the cerebral cortex (Gong, He et al. 2012), whether anatomical covariance requires intact axonal connectivity, or can develop in the face of altered connectional substrates like in the case of congenital callosal alterations or white matter abnormalities (Tyszka, Kennedy et al. 2011, Sforazzini, Bertero et al. 2016), remains to be determined. Finally, although both genetic and environmental factors have been identified to play a role in shaping these networks (Schmitt, Lenroot et al. 2008, Schmitt, Lenroot et al. 2009, Rimol, Panizzon et al. 2010), the relative contribution of these components is poorly understood and it is not clear what is the relative contribution of genetic influence, development and aging, or experience-related plasticity to the establishment of scMRI “connectivity” (Evans 2013).

Brain imaging research in simple model organisms like the laboratory mouse, where genetic and environmental conditions can be tightly controlled, could help to clarify the mechanisms underlying the emergence of covariance networks and increase both the clinical value of scMRI for neuropsychiatric patients and the capacity to test specific network hypotheses about disease mechanisms (Alexander-Bloch, Giedd et al. 2013). Possibly more significant, showing the existence of scMRI networks in inbred mice would lead to the application of this technique on transgenic mice that model a variety of human brain diseases, thus making it possible to elucidate the relation between genetic deletions and derangement of scMRI networks in brain disorders. The ever-increasing repertoire of transgenic mice available to preclinical community may be employed to model a variety of human brain diseases, thus allowing the investigation of neurobiological determinants underlying the reorganization of scMRI networks in

pathological conditions.

Despite the great interest in this approach, the application of scMRI mapping to animal models has been so far very limited, with only preliminary demonstration of its application in non-human primate research (Alexander, Chen et al. 2008, Spocter, Hopkins et al. 2010). One of such studies reported the effects of aging in a non-human primate model (Alexander, Chen et al. 2008), where reductions of gray matter volumes were found in prefrontal regions and in the superior temporal sulcus. An exploratory scMRI analysis in rodents has been previously reported (Badea, Johnson et al. 2009), leading to the identification of a large putative limbic network. However a fine grained description of homotopic cortical and subcortical scMRI analogous to those previously reported in humans (**Figure 9**) has not so far been described in rodents.

1.3. The Scope of this Thesis

The main aim of the set of studies presented in this thesis is to probe the presence and map the topology of scMRI networks in the mouse brain to enable investigations of the factors determining the genesis of scMRI, and its altered expression in disease states. An essential prerequisite for a reliable mapping of scMRI is the development of robust VBM assessment of gray matter volumes in the mouse brain. To this purpose, we morphed a mouse gray matter VBM pipeline based on ANTs advanced image processing tools originally developed for human neuroimaging studies (Pagani, Damiano et al. 2016). We next validated this VBM pipeline in a study aimed to evaluate the trophic gray matter effect of dietary supplementation with omega-3 polyunsaturated fatty acids (n3-PUFA). The approach revealed robust gray matter volumetric increase in the hippocampus and medial prefrontal cortex (mPFC) in mice treated with n3-PUFA compared to the isocaloric control group (Cutuli, Pagani et al. 2016), thus contrasting the natural loss of gray matter which has been associated to aging.

Having showed that our methods can detect plastic gray matter volumetric changes, we next applied VBM to map local gray matter volumes and scMRI networks in a large cohort of genetically homogeneous inbred C57Bl6/J mice. In agreement with findings of human studies, our results highlighted that gray matter scMRI coupling emerge in the mouse brain. Specifically, whole brain voxel-wise correlation maps based on seed region analysis revealed the existence of homotopic scMRI networks in primary and associative cortical as well as subcortical brain regions. The bilateral topology of the cortical networks was further confirmed in an unbiased fashion with source based morphometry based on independent component analysis (ICA). Using hierarchical agglomerative clustering, we also show that communities of brain regions sharing similar patterns of scMRI form plausible clusters overlapping with well-known neuroanatomical districts, providing evidence that scMRI networks overlap with the anatomical organization of the brain. The observation of scMRI networks in genetically homogeneous C57Bl/6 inbred mice further suggests that reduced environmental stimulation is sufficient to morph these correlational networks, in keeping with the emerging view of a key role of environmental factors in shaping scMRI.

1.4. Main Contributions of this Work

The study of scMRI networks and gray matter volumetric alterations in transgenic mice - where a wide repertoire of genetic, molecular and cellular manipulations can be readily implemented - is poised to complement human research by enabling the understanding of genetic and environmental underpinnings in normal subjects and in genetic models of neuropsychiatric disorders.

The main contributions of this work are methodological and neurobiological. Methodological contributions include:

I. Development and validation of semi-automated gray matter VBM and volumetric anatomical labelling methods to map gray matter, cortical thickness and brain volumes in the mouse brain.

II. A proof of concept validation of this approach and its validation in a system model amenable to trophic remodeling (with nPUFA dietary supplementation)

III. Implementation of hypothesis-driven and data-driven network approaches to describe scMRI topology, producing new powerful translational tools for gray matter connectivity investigations in studies with transgenic mice.

From a more neurobiological standpoint, the contributions of the present work are:

I. By using VBM, we showed that n-3 PUFA dietary supplementation counteracts the natural brain atrophy related to aging in hippocampus and medial prefrontal cortex, and that this effect is behaviorally relevant.

II. In line with findings in humans, we describe for the first time that the architecture of scMRI networks in the mouse brain is homotopic, with gray matter regions in one hemisphere exhibiting positive correlations with their counterpart in the opposite hemisphere.

III. The identification of scMRI networks in genetically homogeneous C57BL/6 inbred mice corroborates the emerging view of a key role of environmental factors in shaping these correlational networks.

IV. Our work supports the use of mice in future studies to generate hypotheses about derangement of anatomical covariance in pathological states of clinical relevance.

All the contributions presented in this thesis have been published in the form of peer-reviewed manuscripts and conference communications (Chapter 2, 3 and 4). The structure of the present thesis comprises a description of the brain morphometry methods

implemented and validated for the mouse brain (Pagani, Damiano et al. 2016) (Chapter 2), followed by a proof of concept of these methods in a study aimed at testing the efficacy of omega3 in counteracting the brain atrophy and cognitive decline related to aging (Cutuli, Pagani et al. 2016) (Chapter 3). The identification and description of scMRI network mapping (Pagani, Bifone et al. 2016) is reported in Chapter 4, followed by conclusions of the thesis (Chapter 5). The last two sections include a complete list of the references and the publication list.

2. Voxel Based Morphometry in the Mouse Brain

All the material presented in this chapter has been recently published in the article "**Pagani M**, Damiano M, Galbusera A, Tsaftaris SA, Gozzi A (2016). Semi-automated registration-based anatomical labelling, voxel based morphometry and cortical thickness mapping of the mouse brain, *Journal of Neuroscience Methods*, 11:62-73."

Morphoanatomical MRI methods have recently begun to be applied in the mouse. However, substantial differences in the anatomical organization of human and rodent brain prevent a straightforward extension of clinical neuroimaging tools to mouse brain imaging. As a result, the vast majority of the published approaches rely on tailored routines that address single morphoanatomical readouts and typically lack a sufficiently-detailed description of the complex workflow required to process images and quantify structural alterations. Here we provide a detailed description of semi-automated registration-based procedures for voxel based morphometry, cortical thickness estimation and automated anatomical labelling of the mouse brain. The approach relies on the sequential use of advanced image processing tools offered by ANTs, a flexible open source toolkit freely available to the scientific community.

To illustrate our procedures, we described their application to quantify morphological alterations in socially-impaired BTBR mice with respect to normosocial C57BL/6J controls, a comparison recently described by us and other research groups. We show that the approach can reliably detect both focal and large-scale gray matter alterations using complementary readouts. No detailed operational workflows for mouse imaging are available for direct comparison with our methods. However, empirical assessment of the mapped inter-strain differences is in good agreement with the findings of other groups using analogous approaches. The detailed operational workflows described here are expected to help the implementation of rodent morphoanatomical methods by non-expert users, and ultimately promote the use of these tools across the preclinical neuroimaging community.

2.1. Background

A deep understanding of the genetic, physiological and anatomical underpinnings of brain disease is essential for the development of improved therapies. A milestone towards this goal is the generation of genetically modified mouse lines that recapitulate targeted genetic mutations in experimentally controlled studies. Genetically modified mouse lines permit to relate genetic mutations to clinically relevant endophenotypes without the complexity of genetic heterogeneity and the uncontrolled impact of gene-gene and gene-environment interactions in adult human populations (Nestler and Hyman 2010).

MRI methods offer a privileged point of view to study genetically altered mouse models of neuropsychiatric disorders in many respects. First, the use of comparable imaging readouts in men and mice permits a cross-species comparison of brain endophenotypes of translational relevance, thus enhancing the transfer of information from and to the clinic. At the same time, MRI readouts can also be employed to assess the extent to which mouse models of central nervous system pathology replicate neuroimaging findings observed in clinical populations, informing preclinical researchers on the translational validity of these models. Moreover, high resolution morphometric MRI, achievable at ultra-high field strength or in *ex vivo* formalin-fixed samples (Lerch, Gazdzinski et al. 2012, Tucci, Kleefstra et al. 2014) can be employed to obtain a fine-grain assessment of structural brain alterations that could serve as a convenient surrogate for labor intensive manual morphometric measurements in *ex vivo* brain slice preparations, with the additional advantage of being non-invasive and multi-dimensional.

Structural MRI based imaging methods - such as voxel based morphometry (VBM) of gray matter (GM), cortical thickness mapping and anatomical labelling - have been widely employed to study brain morphology in human populations (Mueller, Keeser et al. 2012). The application of analogous readouts to map genetically determined brain alterations in transgenic mouse

lines has been recently proposed, an effort collectively referred to as MRI phenotyping (Johnson, Ali-Sharief et al. 2007, Borg and Chereul 2008, Lerch, Sled et al. 2011). Recent improvements in MRI sequences and hardware, together with the development of fixation protocols for *ex vivo* imaging of stained brain specimens (Lerch, Gazdzinski et al. 2012), have made it possible the acquisition of artefact-free and high resolution – with a voxel size less than 80 µm – mouse brain volumes even at relatively low magnetic field strengths. This efforts have resulted in the publication of several examples or the application of morphoanatomical imaging to transgenic mouse models (Yushkevich, Piven et al. 2006, Lerch, Carroll et al. 2008, Sawiak, Wood et al. 2009, Xie, Yang et al. 2010).

The development of standardized preprocessing and analytical pipelines for human imaging data, and their implementation in popular software toolkits such as such as FMRIB Software Library (FSL) (Jenkinson, Beckmann et al. 2012), Statistical Parametric Mapping (SPM) (Friston, Holmes et al. 1994) and Advanced Normalization Tools (ANTs) (Avants, Tustison et al. 2009), have been instrumental to the widespread use of MRI in human brain research. However, substantial differences in the dimensions and anatomical organization of the human and rodent brain prevent a straightforward extension of these tools to morphoanatomical mouse brain mapping. As a result, several research groups have developed tailored procedures for the preprocessing and analyses of morphoanatomical brain MRI readouts in mouse models (Nieman, Bock et al. 2005, Delatour, Guegan et al. 2006, Johnson, Ali-Sharief et al. 2007, Borg and Chereul 2008, Sawiak, Wood et al. 2009, Lee, Ruffins et al. 2010, Lerch, Sled et al. 2011, Badea, Gewalt et al. 2012, Sawiak, Wood et al. 2013). However, the vast majority of the published approaches typically address single morphoanatomical readouts (e.g., VBM or anatomical labelling or cortical thickness), and lack a detailed description of the complex

workflow and computational parameters required to process, analyze and quantify structural MRI alterations, thus complicating the implementation of these procedures by non-expert users.

To begin to address these issues, here we provide a detailed methodological description of a semi-automated operational workflow for VBM, cortical thickness estimation and automated anatomical mapping of the mouse brain. To simplify and streamline operations, we based image processing mainly on ANTs (Avants, Tustison et al. 2009), a flexible and powerful open source toolkit freely available to the scientific community. Importantly, our approach has been recently applied by our research group to map fine-grain brain anatomy alterations in different mutant mouse lines (Dodero, Damiano et al. 2013, Minervini, Rusu et al. 2014, Sannino, Gozzi et al. 2014, Tucci, Kleefstra et al. 2014, Lassi, Priano et al. 2015) and to describe scMRI large-scale networks between gray matter regions in wild-type mice (Pagani, Bifone et al. 2016), with excellent agreement between MRI and manual morphometric measurements (Sannino, Gozzi et al. 2014), exhibiting corresponding morphoanatomical features in mice and reference clinical populations (Tucci, Kleefstra et al. 2014, Cutuli, Pagani et al. 2016). Below, we provide a detailed description of our procedural workflow and show its capabilities by describing its application to quantify morphological alterations in socially-impaired BTBR T+Itpr3tf/J mice with respect to normosocial C57BL/6J controls (Dodero, Damiano et al. 2013, Squillace, Dodero et al. 2014), a comparison that has been recently described by our research group (Dodero et al., 2015) and others (Ellegood, Babineau et al. 2013), thus permitting an empirical cross-laboratory assessment of the validity of our findings.

2.2. Materials and Methods

2.2.1. Ethical Statement

All *in vivo* studies were conducted in accordance with the Italian law - D.L. n° 116, 1992, Ministero della Sanità, Roma - and following the recommendations in the Guide for the Care and Use of Laboratory Animals of the National Institutes of Health. The animal research protocol was approved by the Animal Care Committee of the Istituto Italiano di Tecnologia (Permit Date 07-2012). All surgical procedures were performed under deep anesthesia.

2.2.2. Sample Preparation and MR Acquisition

High-resolution morphoanatomical T2-weighted MR imaging of mouse brains was performed in paraformaldehyde (4% PFA; 100 ml, Sigma, Milan) fixed specimens, a procedure employed to obtain high-resolution images with negligible confounding contributions from physiological or motion artefacts (Cahill, Laliberté et al. 2012). Sample preparation and MRI acquisition of BTBR T+Itpr3tf/J (BTBR) and C57BL/6J (B6) mice has been recently described in previous work (Dodero, Damiano et al. 2013, Sforazzini, Bertero et al. 2014, Sforazzini, Schwarz et al. 2014) and is briefly summarized here. Male BTBR (N=9, 15-26 weeks old) and age-matched control B6 (N=9) mice were deeply anaesthetized with an intraperitoneal Avertin injection (375 mg/Kg, Sigma, Milan) and their brains were perfused in situ via cardiac perfusion. The perfusion was performed with phosphate buffered saline followed by paraformaldehyde (4% PFA; 100 ml). Both perfusion solutions were added with a Gadolinium chelate (Prohance, Bracco, Milan) at a concentration of 10 and 5 mM, respectively, to shorten longitudinal relaxation times (Lerch, Gazdzinski et al. 2012).

A multi-channel 7.0 Tesla MRI scanner (Bruker Biospin, Milan) was used to acquire anatomical images of the brain, using a 72 mm birdcage transmit coil, a custom-built saddle-shaped

solenoid coil for signal reception, and the following imaging parameters: 3D RARE spin-echo sequence, TR=550 ms, TE=33 ms, RARE factor=8, echo spacing 11ms, matrix size of 192x 170x170 and voxel size of 0.09 mm (isotropic), with a total acquisition time of 4 hrs and 25 mins.

2.2.3. Image Preprocessing and Analysis

A detailed description of the image processing workflow employed to create a study based template, to estimate cortical thickness, and to perform automated anatomical labelling and VBM is reported below for structural images acquired at 7 Tesla. We refer to our approach as "registration-based" as several preprocessing and estimation steps (e.g. cortical thickness) are executed via a combination of affine and symmetric diffeomorphic transformations as implemented in antsRegistration command (Avants, Tustison et al. 2014). The tool entails the application of affine registration with twelve degrees of freedom to coarsely normalize the overall shape of a source image to a reference image. Afterwards, a non-linear transformation is applied to create a differentiable and invertible diffeomorphic map which locally aligns source and reference image by adjusting for local inter-individual morphological differences.

Flowcharts are provided as a visual reference to guide the description of each computational step, where light grey shading denotes image inputs, dark grey shading denotes the final output and computational processes are outlined in the form of rectangular boxes. All the computational steps have been carried out using tools and algorithms implemented within the ANTs toolkit (version 1.9 *http://sourceforge.net/projects/advants/*) and employed to process 3D RARE morphoanatomical images acquired at 7 Tesla with the image sequence parameters described above. The parameter employed for the preprocessing steps were optimized in pilot assessments using both empirical (e.g. segmentation) and quantitative approaches (e.g. registration).

Image Preprocessing

Basic image preprocessing includes bias field correction and skull stripping (**Figure 10**). As a first step, all the images are corrected for intensity non-uniformity using N3BiasFieldCorrection, an automated algorithm implemented within the ANTs toolkit using 50 fitting levels. This step reduces bias field signal related to the reception profile of MRI receive coils, a low frequency amplitude modulation of the signal that produces regional variation in voxel intensity as a function of coil proximity. The correction of this bias is an important pre-requisite for subsequent intensity based MR image processing, such as tissue segmentation.

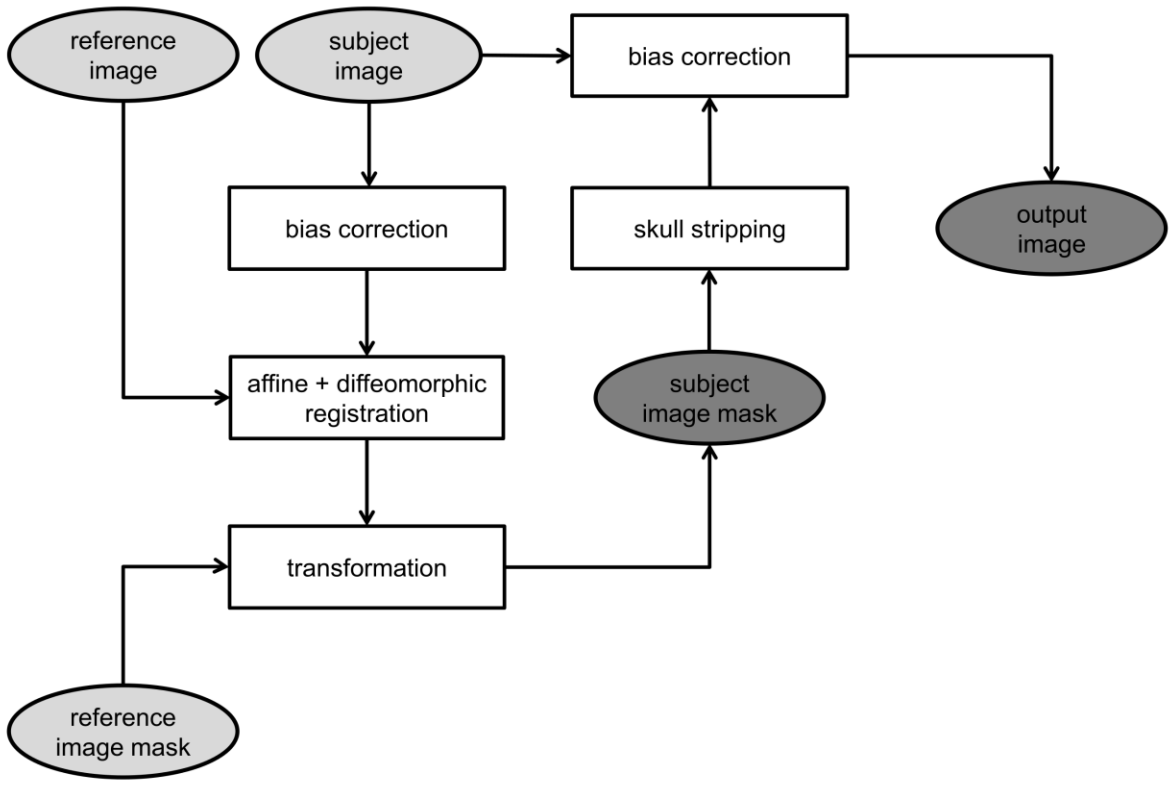

Figure 10 Preprocessing workflow. *Each MRI subject image undergoes a first correction for intensity non-uniformity bias using the N3BiasFieldCorrection. To create individual subject masks, a masked representative reference subject is registered to each subject, and the transformation of this registration is then applied to the reference subject mask. The application of this mask permits to remove most extra brain tissue. Non-uniformity bias is subsequently estimated for individual masked brains. The preprocessing procedure outputs a skull-stripped bias-corrected image and a companion binary brain mask for each subject.*

Skull stripping is required to remove extra brain tissue, thus crucially improving the accuracy of subject-to-template registration. In order to automate skull-stripping and avoid tedious and error-prone manual segmentation, an automatic registration-based approach to skull stripping was devised. This is carried out by registering the bias adjusted MRI volumes to a skull stripped reference image using an affine and diffeomorphic registration algorithm. The skull stripped reference image should ideally be chosen from the study population or from comparable experiments of the same laboratory.

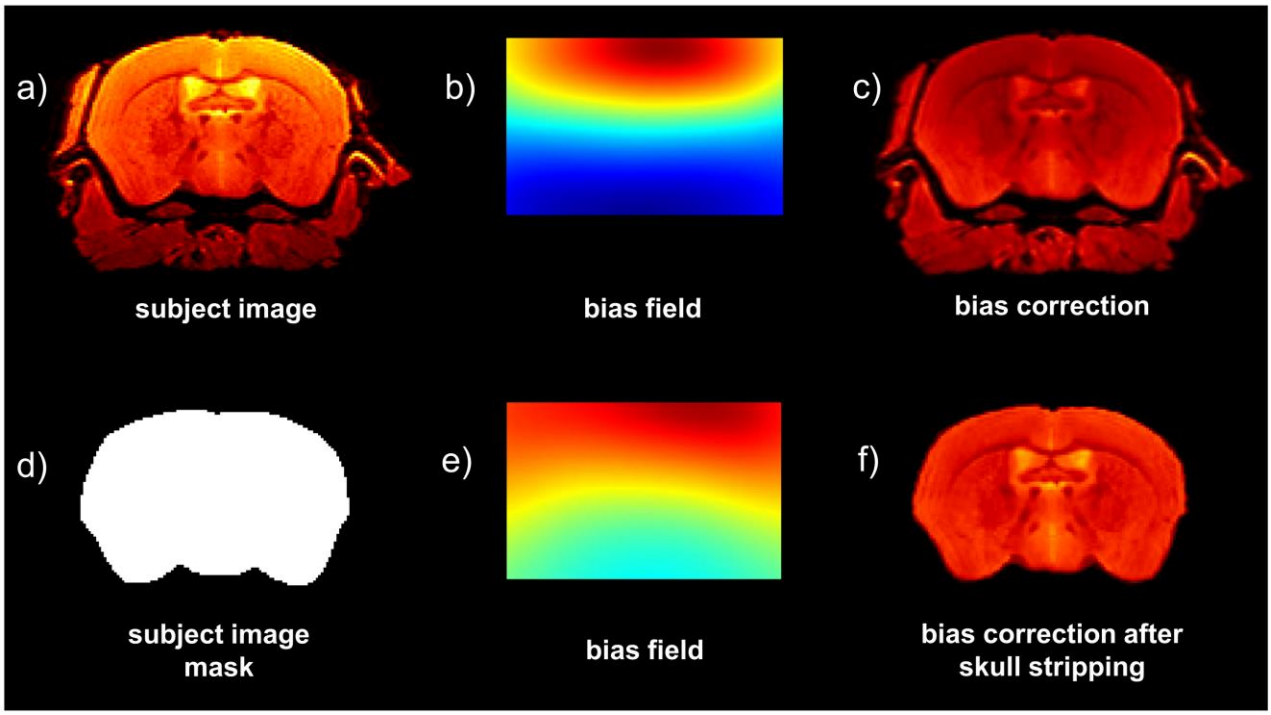

Figure 11 Preprocessing results. *In this illustrative example, the original subject image (a) is bias corrected before (b) and after (e) skull stripping (d). Note the improved bias field correction after skull stripping (f) with respect to the bias correction prior skull stripping (c), especially in the ventral part of the brain and in the ventricles. Voxels intensity is represented in shades of red to magnify image contrast.*

A companion brain binary mask of the reference image can be segmented manually. While potentially labor intensive in high resolution brain images, this process can be performed only once, and it is instrumental to automating skull stripping for all the subsequent subjects and

analyses. After the registration, the diffeomorphic map is applied to non-linearly transform the brain mask of the reference image into the subjects' space using WarpImageMultiTransform. The subject's brain mask is then applied to each original subject image to obtain skull stripping. An additional bias correction is subsequently performed on the skull stripped subject image to achieve a more accurate estimation of the bias field, devoid of the contribution of non-brain related protrusions.

An illustrative example of the advantage of performing two independent bias corrections, (before and after skull stripping, respectively) is reported in (**Figure 11**). Even though the first step does not flawlessly compensate for signal inhomogeneity in all brain regions (i.e. the ventral areas of the brain and in the ventricles), its use provides a first normalization of signal intensity that results in an improved the accuracy of registration based estimation of brain mask, and the removal of brain extra tissue. After this skull stripping step, the bias field of the original subject image is re-estimated, leading to a more accurate bias correction. The results of this first-pass skull stripping are typically visually inspected for imperfections, usually present in a minority of subjects, which can be easily manually corrected, for example using the brushtool of ITKsnap (Yushkevich, Piven et al. 2006). For each subject, the result of preprocessing is a skull stripped and bias corrected brain image, exhibiting uniform contrast within the same tissue class, and its binary mask.

Study Based Template

A critical element in our approach is the construction of a study based template to establish a common reference space for all the subsequent analyses. In cross-sectional mouse studies, the most adopted experimental designs for mouse phenotyping with transgenic lines, this involves the creation of an average template from a reference population, typically the control subjects (B6 in this study). This leads to the generation of a template recapitulating

neuroanatomical features of “healthy” or reference population, avoiding the combination of conflicting morphoanatomical traits which could affect subsequent computational steps (e.g. segmentation). For example, the use of both normo-callosal B6 and acallosal BTBR mice for template creation would result in a chimeric image exhibiting a blurred and hypo-intense corpus callosum, a feature that could negatively affect the quality of subsequent segmentation priors. The creation of different templates for different studies can help minimizing confounding effects related, for instance, to perfusion, age, sex and brain sizes.

Study-based template creation was implemented via the use of the buildtemplateparallel script available within the ANTs toolkit (Avants, Yushkevich et al. 2010). This script entails an automated and iterative intensity-based registration approach to automatically create a study based template using a predefined list of subjects (Kovacevic, Henderson et al. 2005). A representative subject is selected as initial reference and each subject is linearly registered to the reference subject using an affine transformation. After intensity averaging all registered images to obtain a first linear group average, an iterative five-generation multi-scale non-linear alignment process is performed using a Greedy Syn diffeomorphic registration algorithm (Avants, Epstein et al. 2008) with a maximum of 120 iterations for each step. This process entails an initial diffeomorphic registration of each subject to the reference linear group average to obtain individuals’ warps using cross correlation as similarity metric. These warps are then averaged and applied to the template to update its shape and conform it to the population shape. The process is iteratively repeated four more times, by using as reference the warped template from the previous iteration. The final outcome is an average template volume exhibiting clear structural boundaries, incorporating fine grain neuroanatomical descriptions of the reference population, and reduced intensity variation.

Anatomical Labelling

The assessment of subtle anatomical differences in gross morphology via manual delineation of brain structures is a laborious and time consuming task that may introduce intra- and inter-observer bias (Badea, Gewalt et al. 2012).

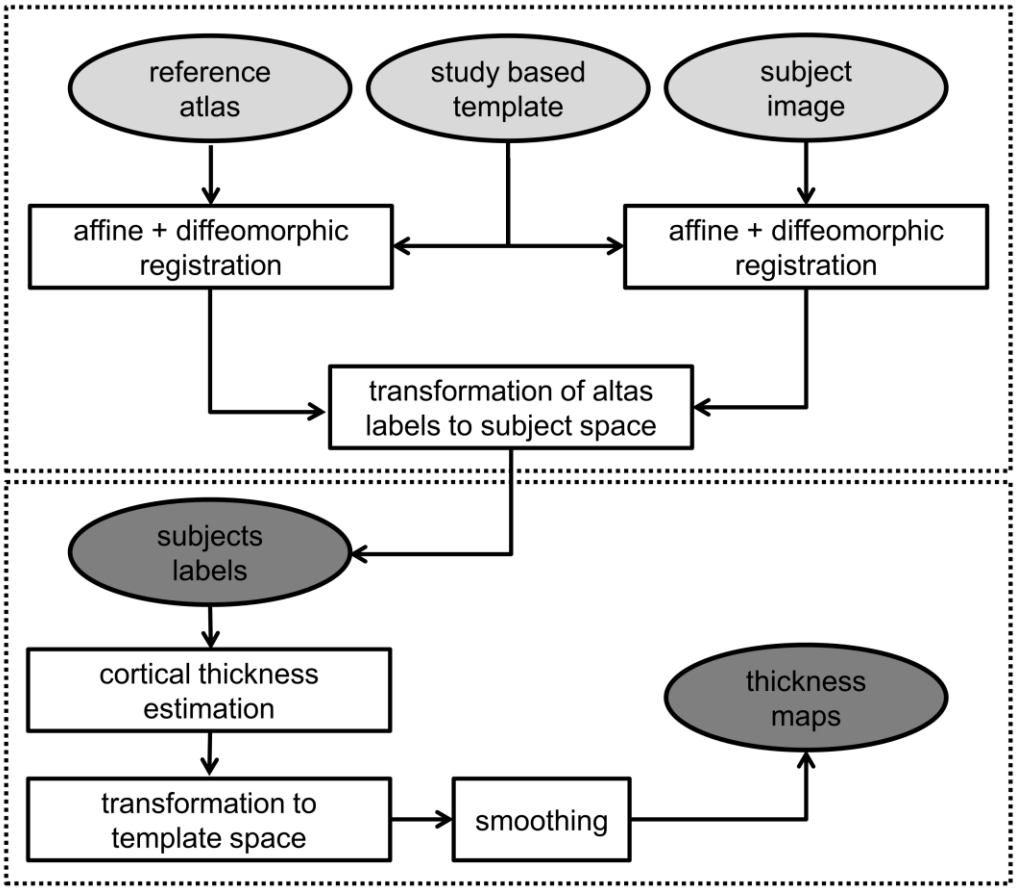

Figure 12. Automated anatomical labelling and cortical thickness estimation. *Upper box: Anatomical labels of the MRI atlas are registered into each subject space via the study based template through a combination of linear and diffeomorphic mapping, using antsRegistration and WarpImageMultiTransform. A propagation of the labels from the MRI atlas to each subject space is then performed via the study based template. Lower box: Anatomical labels of the cortical mantle in the subject space are merged together to build a unified cortical label. This cortical label and subject brain mask of the subjects are used to create the inputs needed to estimate the cortical thickness using DiReCT. The obtained cortical thickness maps are eventually warped again into the study based space and smoothed for subsequent statistical comparison.*

The procedures described here allows for volumetric estimation via anatomical labelling, a procedure whereby brain regions can be labelled and classified depending on their anatomical location. The process employed in our workflow relies on the availability of preprocessed images, a study-based template and two neuroanatomical labelled reference MRI atlases for cortical (Ullmann, Watson et al. 2013) and subcortical (Dorr, Lerch et al. 2008) areas, respectively. The output of automated anatomical labelling is a fine-grained projection of a given anatomical label in the subject's coordinate space. The anatomical labels thus registered can be used both to measure the volume of anatomical regions of interest for cross-strain statistical comparison, or as intermediate input for further analyses, such as cortical thickness estimation (**Figure 12**). The volume of specific anatomical regions in individual subjects is computed using a template based anatomical labelling strategy (Avants, Yushkevich et al. 2010). As previously reported in the literature, the propagation of labels from the anatomical labelled atlas to the subject space is more accurate when performed via the study based template to minimize variation due to registration errors (Jia, Yap et al. 2011). To this purpose, a composition of affine and diffeomorphic (SyN) registration between the reference neuroanatomical atlas and the study based template is performed to project the anatomical labels in the coordinate system of the study based template (Avants, Tustison et al. 2009) For the anatomical images and RARE sequence used in this study we adopted cross correlation as similarity metric, with a window radius of 5 and a gradient step length of 0.25. The optimization was performed over four resolutions for both transformations with a maximum of 100 iterations for the coarse levels and 10 at the full resolution.

A simple propagation of the neuroanatomical labels mapped in the study-based template space to the subjects' space can then be achieved via the registration of each subject to the study based template and the subsequent propagation of the labels to each subject. The efficiency

of the registration procedures can evaluated using the Dice coefficient (DiceAndMinDistSum command from ImageMath), which quantifies the overlap between a manually defined label and the same label resulting from our automated labelling, in the subject space (Dice 1945). Label volumes can then be easily computed using tools included in several MRI software packages (e.g. LabelStats command from ImageMath, or FSL's fslstats).

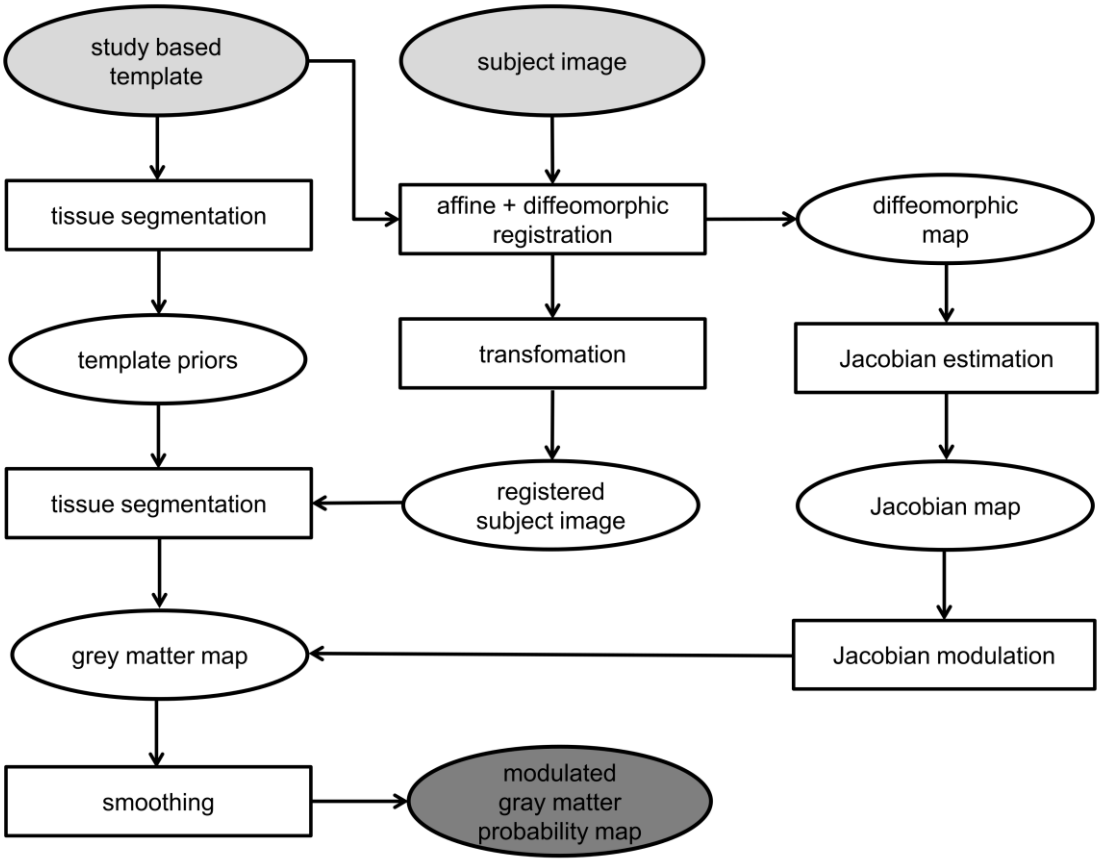

Figure 13. VBM. *Each preprocessed subject image is mapped on the study based template space through a combination of linear and diffeomorphic mapping, using antsRegistration and WarpImageMultiTransform. Registered volumes are segmented using the study based template priors. Grey matter probability maps for each subject are then modulated using Jacobian maps obtained from the registration process and smoothed for subsequent statistical comparison.*

Voxel Based Morphometry

VBM is a whole-brain technique for characterizing regional brain volume and differences in tissue concentration, in particular GM, across subjects. In our procedure, it consists of five main steps (**Figure 13**). First, a study based template is created using brain anatomical images from reference population described above. Second, the original images of the two groups of subjects are registered to the study based template via the same affine and diffeomorphic mapping used for anatomical labelling.

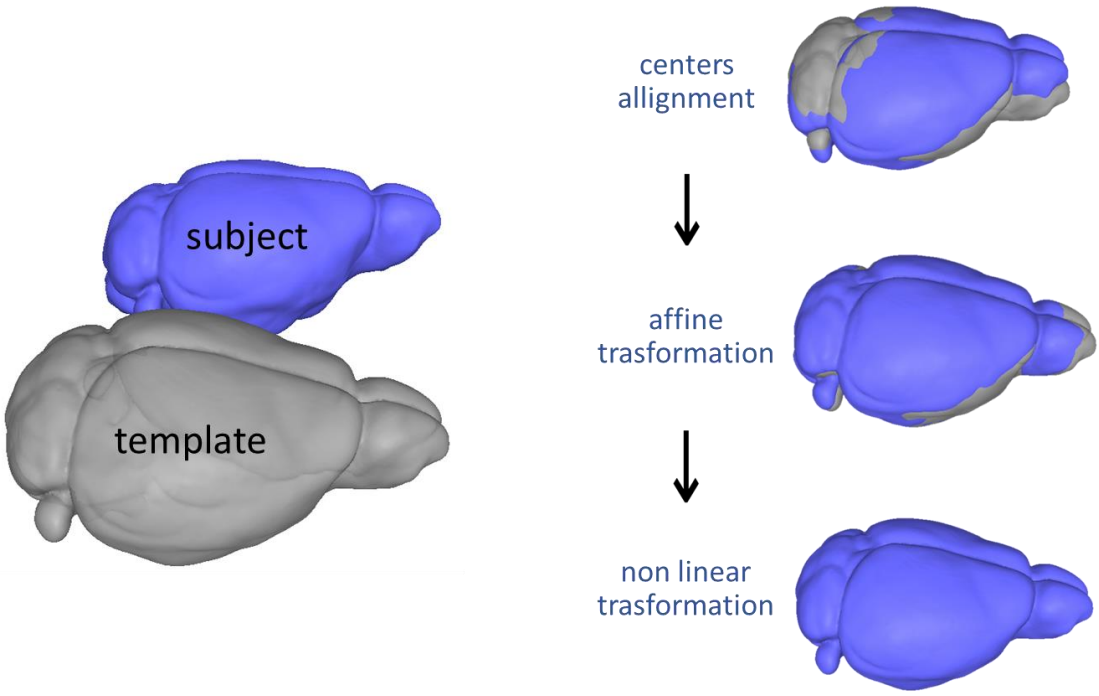

Figure 14. Registration of mouse brains to the study based template. Each preprocessed subject image is registered to a common reference space, i.e. the study based template space by using a set of linear and diffeomorphic transformation.

Third, spatially normalized images are segmented using a Markov Random Field model, implemented by the Atropos command of the ANTs toolkit (Avants, Tustison et al. 2011). To classify tissues we applied a smoothing factor of 0.0125, a radius of 1 and the maximum number of iterations was set at 10. The separation of GM (i.e. the readout of interest) from white matter

(WM) and cerebrospinal fluid (CSF) is improved by initializing the process with the study based template, previously segmented using standard k-means clustering included in the Atropos command (**Figure 15, B-C**). The procedures described here allows for volumetric estimation via anatomical labelling, a procedure whereby brain regions can be labelled and classified depending on their anatomical location. The process employed in our workflow relies on the availability of preprocessed images, a study-based template and two neuroanatomical labelled reference MRI atlases for cortical (Ullmann, Watson et al. 2013) and subcortical (Dorr, Lerch et al. 2008) areas, respectively. The output of automated anatomical labelling is a fine-grained projection of a given anatomical label in the subject's coordinate space. The anatomical labels thus registered can be used both to measure the volume of anatomical regions of interest for cross-strain statistical comparison, or as intermediate input for further analyses, such as cortical thickness estimation (**Figure 12**).

The volume of specific anatomical regions in individual subjects is computed using a template based anatomical labelling strategy (Avants, Yushkevich et al. 2010). As previously reported in the literature, the propagation of labels from the anatomical labelled atlas to the subject space is more accurate when performed via the study based template to minimize variation due to registration errors (Jia, Yap et al. 2011). To this purpose, a composition of affine and diffeomorphic (SyN) registration between the reference neuroanatomical atlas and the study based template is performed to project the anatomical labels in the coordinate system of the study based template (Avants, Tustison et al. 2009). For the anatomical images and RARE sequence used in this study we adopted cross correlation as similarity metric, with a window radius of 5 and a gradient step length of 0.25. The optimization was performed over four resolutions for both transformations with a maximum of 100 iterations for the coarse levels and 10 at the full resolution.

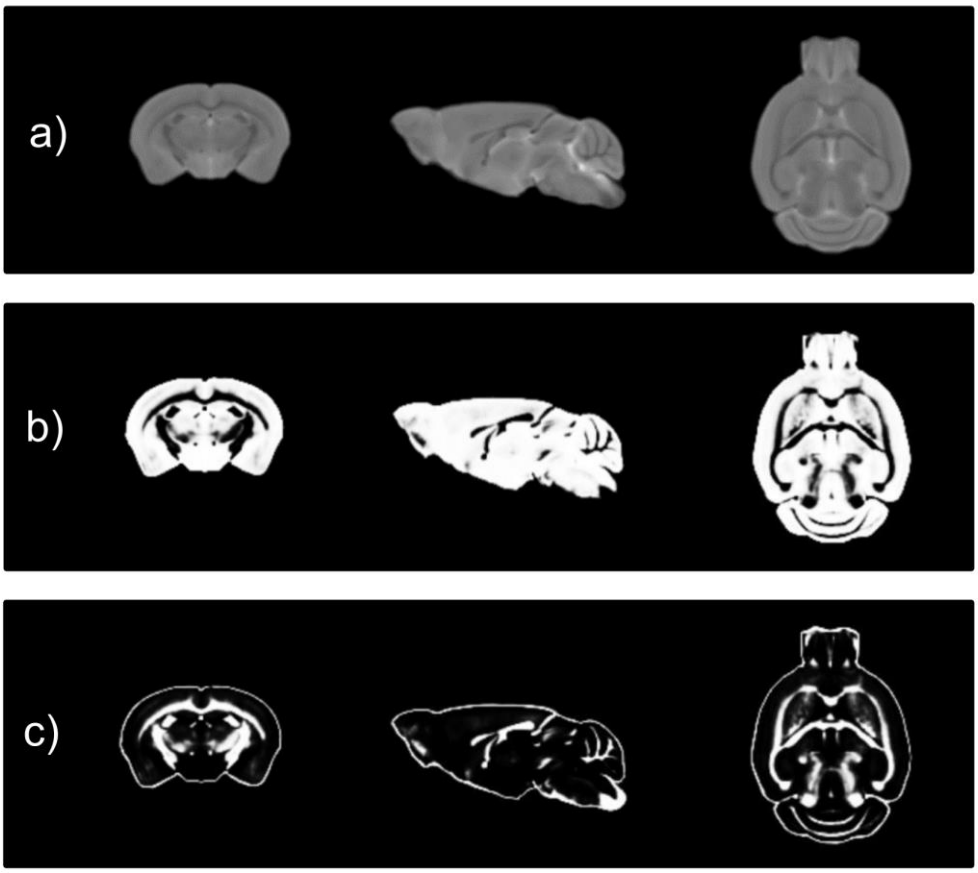

Figure 15. Study based template and tissue segmentation. *Orthogonal slice view of a study based template of the B6 mice population obtained using the iterative diffeomorphic registration process of the buildtemplateparallel script and its corresponding tissue segmentation (a). The template is segmented using Atropos in 6 different tissue classes which are used as a-priori information for individual estimation of gray matter in VBM. The different tissue classes of the template are combined to obtain gray matter (b) and non gray matter components (c, white matter, plus ventricular regions and CSF).*

This step is especially critical and it is therefore here described in greater detail. In pilot work, we explored the number of tissue classes leading to optimal separation of GM from non-GM components (WM plus CSF). A canonical three-class segmentation of *ex vivo* mouse brain using Atropos results in inefficient GM/WM segmentation, leading to an overestimation of WM fraction at the expense of GM (**Figure 16**).

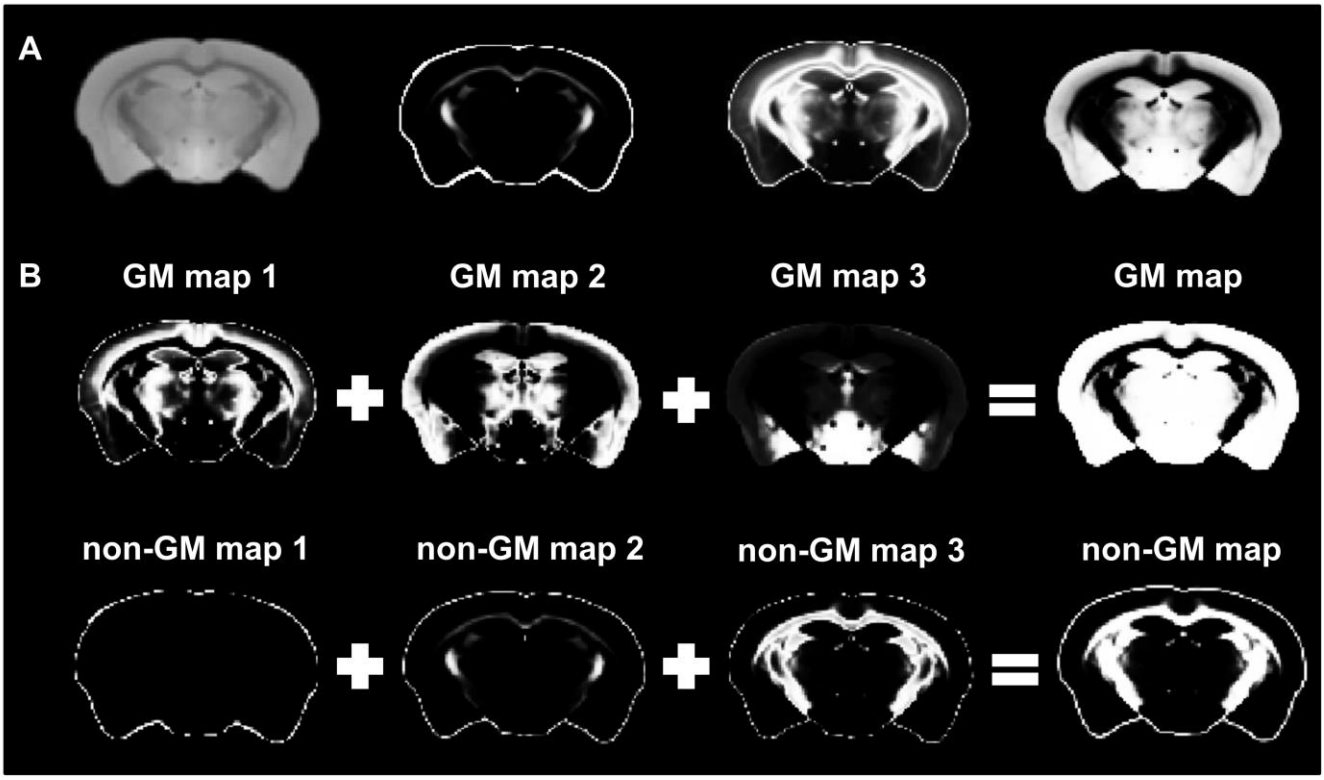

Figure 16. Segmentation of the study based template using six tissue classes provides accurate GM/WM separation. *A: Standard three-class segmentation of our ex vivo brains using Atropos did not produce an accurate GM/WM separation, with a great overestimation of white matter fraction. Anatomical template (left), plus the segmentation classes obtained with a three-cluster segmentation approach (WM, mixed WM/GM and GM matter maps, from left to right, respectively). B: The combined use of six independent segmentation classes leads to a more accurate separation of GM and WM. The final GM map is the combined result of three GM classes (middle row). Additional non-GM tissue can be obtained by merging the remaining three classes.*

The use of six independent classes results in three GM clusters that can be merged to provide a final accurate GM map (**Figure 15**). A similar approach has been employed by other investigators (e.g. (Li, Cheung et al. 2009)). Our segmentation procedure results in a two-voxel layer on the outmost edge of the cortex which is labelled as “non gray matter” and, as such, is not included in subsequent analysis. These voxels are characterized by low or very-low signal intensity and reflect a combination of partial volume effects between gray matter and non MRI visible skull signal, and possibly also small inaccuracies due to registrations. In our workflow,

these “low confidence” gray matter voxels are discarded to improve the robustness of subsequent voxelwise statistical mapping.

In our procedure, the quality of segmentation is assessed empirically by comparing individual and merged tissue classes with the anatomical distribution of known high-density WM structures such as the corpus callosum, anterior and posterior commissures, as seen in the study based template (**Figure 15**). These structures are easily identifiable and their extension can be compared with their segmented counterparts. Future developments of our initial workflow could employ quantitative approaches to estimate goodness of cluster separation (Chou, Su et al. 2004, Wu and Yang 2005), although operator dependent assessments of tissue class separations are ultimately warranted to ensure biologically meaningful results.

It should be noted that the segmentation procedure employed in our work does not always lead to a clear separation of WM and CSF, at least on brain volumes acquired *ex vivo*. Besides differences in the anatomical organization of the mouse brain and image contrast in the PFA perfused brain (Cahill, Laliberté et al. 2012), a contributing reason for this is the occurrence of CSF loss from the brain in a large proportion (ca. 70%) of the subjects as a consequence of the *ex vivo* fixation procedure, leading to the presence of signal voids in ventricular space. These low signal-intensity intra-ventricular foci are typically classified as WM, leading to mixed or incomplete separation between these two brain components. Such incomplete separation however does not limit the validity of our approach, because both CSF and WM (even if separate) would invariably end up being discarded from subsequent GM-based analyses (i.e. VBM and cortical thickness).

After tissue segmentation, the Jacobian determinants of the deformation are calculated with ANTSJacobian command of the ANTs toolkit and used to modulate the GM probability maps calculated during the segmentation step. This step permits the analysis of GM probability maps

in terms of local anatomical variation instead of tissue density (Ashburner and Friston 2000). Jacobian determinants can be also normalized by the total intracranial volume to further eliminate overall brain volume variations and calculate relative GM volumes. Fifth, the resulting modulated GM probability maps are smoothed using a Gaussian kernel with a sigma of three voxel width (FWHM=0.64mm) and employed for voxel-wise statistical comparison.

Cortical Thickness

The proposed registration-based cortical thickness DiReCT estimation approach (**Figure 12**) is a voxelwise computational approach based on the method presented by Das and colleagues (Das, Avants et al. 2009) and relies on the KellyKapowsky command within ANTs toolkit. The method provides cortical thickness measurements at the voxel level using cortical and non-cortical labelled volumes as inputs. From an anatomical standpoint, the cortical labelled volume employed (cortical ribbon) is limited between an external outline corresponding to the outer layer of the cortex and an internal outline identified by the inner layer of the cerebral cortex adjacent to callosal WM fibers. The method identifies a continuous one-to-one correspondence between inner and outer cortical surfaces and the cortical thickness is estimated via a distance measure on the basis of this diffeomorphic correspondence. The inner surface is used as a reference to initialize a thin layer of about 1 voxel width. This layer, which replicates the shape of the outer layer of the cortex, is then allowed to expand under the diffeomorphic deformation. The deformation is introduced through the cortical label until the layer reaches the outer cortical surface and the obtained deformation map can eventually be used to compute the cortical thickness. The final result of this process is a cortical voxelwise map with a nominal “thickness” value in each voxel, reflecting the deformation field that voxel has been subjected to (Das et al., 2009). **Figure 17** shows an illustrative example of the obtained voxelwise cortical thickness map where the presence of parallel columns of voxels exhibiting constant thickness is apparent.

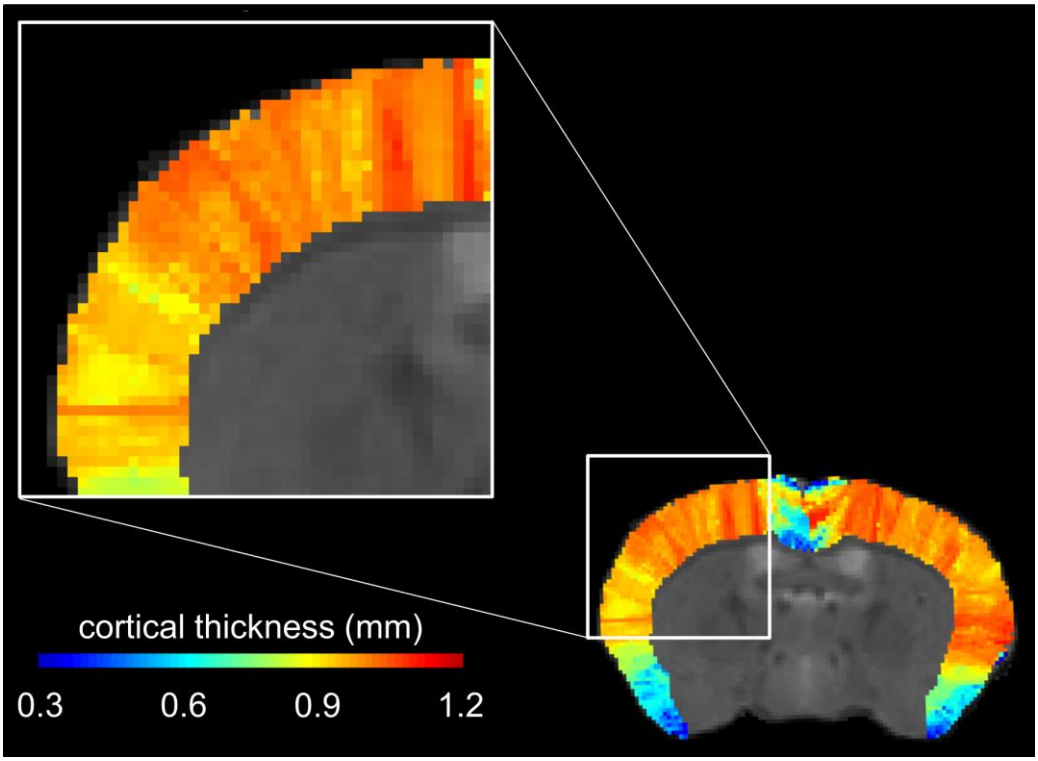

Figure 17. Cortical thickness estimation*. In lissencephalic brains, DiReCT measurement results in a string of voxels exhibiting constant thickness. This appears in the form of parallel cortical "columns" in coronal brain slices clearly visible in the magnified view, where colors represent the norm of the deformation field that is the estimated thickness.*

The obtained maps are then typically cross-compared using standard voxelwise statistics. The original method (Das, Avants et al. 2009) was optimized to identify deep sulci of the human brain by forcing the algorithm to recover lost sulci, but can also be applied to map lissencephalic cortices like those of the rodent brain. The estimation process is carried out separately for right and left hemisphere to preserve the Neumann boundary (Lee, Ehlers et al. 2011). The cortical thickness estimation includes four main steps. First, a right and the left cortical label need to be created, as well as the non-cortical label. In the present study this was achieved by combining all cortical labels mapped (enthorinal cortex, frontal, occipital and parieto-temporal lobe) of the Dorr MRI atlas of the mouse brain (Dorr, Lerch et al. 2008) into one single hemispheric label. A non-cortical label was generated by merging all the remaining non-cortical regions. Second,

cortical thickness is estimated using KellyKapowsky, with a prior anatomical constraint of cortical thickness of two millimeters and a gradient step size for optimization of 0.02. Number of iterations, threshold and window size for convergence were left unchanged (e.g. default parameters). Third, maps of cortical thickness are combined into a joint volume and transformed to template space using available registration maps obtained previously. Fourth, the transformed cortical maps are smoothed using a Gaussian kernel with a sigma of two voxel width (FWHM=0.42). This process yields images that can be used for univariate or multivariate analysis at the voxel level. Despite the use of non-callosal mice our automated anatomical labelling correctly labelled the cortical mantle of BTBR in virtually all cortical areas, with possible minor underestimations of cortical thickness in medial anterior cingulate regions. As a result, intergroup alterations in those regions may be interpreted cautiously when acallosal mice are used as reference strain. However, most mouse lines commonly used in neuroscience and preclinical research exhibit normal callosal integrity and are therefore to be considered immune to this potential artefact.

To further evaluate the accuracy of the cortical thickness estimation process, manual measurement was also performed by an experienced operator blinded to the results of the cortical thickness estimation (**Figure 18**). In a randomly chosen subject, three coronal slices were extracted and cortical thickness was measured for secondary motor cortex (M2), secondary somatosensory cortex (S2) and auditory cortex (Au) using the ruler tool available in the ITK Workbench.

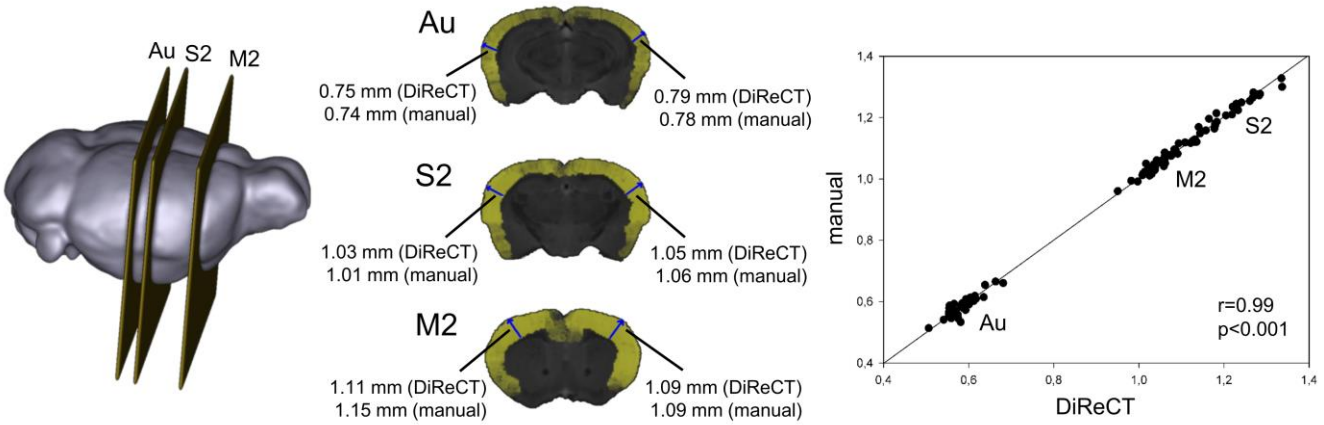

Figure 18. Correlation plot between *DiReCT* outputs and manual measurements of cortical thickness. Secondary motor (M2), secondary somatosensory (S2) and auditory cortex (Au) were chosen as representative cortical areas to validate our cortical thickness methodology. Representative measures from DiReCT and manual estimates are reported for selected cortical regions (middle panel). A correlation plot of manual and automatic measurements highlighted an excellent correspondence between the twee readouts in terms of Pearson's correlation (r=0.99; p<0.001).

Statistical Analysis

All statistical analysis of the smoothed and modulated GM probability maps and cortical thickness maps were conducted using FSL. Firstly, maps were concatenated in a 4D dataset, using fslmerge. Subsequently, standard non-parametric Monte Carlo test with 5000 random permutations was performed using randomise. Threshold-free cluster enhancement was employed to include voxels' neighbourhood information without defining a-priori cluster threshold. P-values were corrected for multiple comparisons using a cluster-based threshold of 0.01 (Salimi-Khorshidi, Smith et al. 2011). Two-tailed voxelwise statistics were used for inter-group VBM and cortical thickness mapping. Brain volumes, resulting from the segmentation process, were tested for statistical differences between the two strains using a two-tailed Student's t-test, followed by Hochberg's correction for multiple comparisons.

2.3. Results

As an illustrative example of the approach, we tested our set of methods to map and quantify morphological variations in inbred socially impaired BTBR mice with respect to normosocial B6 (Squillace, Dodero et al. 2014). A biological interpretation of the differences mapped has been recently reported by us (Dodero, Damiano et al. 2013) and others (Ellegood, Babineau et al. 2013), and will not be re-discussed here.

2.3.1. Study Based Template and Volumetric Analysis

A study based template created following the procedure herein explained is depicted in **Figure 15**. The template was created using the scans of nine normosocial B6 mice, which have been used as reference population for this illustrative study. The template reveals clear structural boundaries and high WM-GM contrast, depicting fine-grain anatomical features that can be used to describe the population more effectively and reliably than a single representative subject (Tucci, Kleefstra et al. 2014).

In pilot studies, we assessed the accuracy of registrations as a function of varying registration parameters (i.e. window radius and gradient step for symmetric normalization) as recently described (Badea, Gewalt et al. 2012). By varying registration parameters, the approach can be used to identify the best set of parameters matching the results of manual parcellation. We varied windows radius between 3 and 9 voxels, and gradient step for symmetric normalization between 0.10 and 2 voxels. The results of this analysis (**Figure 19**) show that the parameters choses (5 and 0.5 voxels, respectively) produce a good registration accuracy in all the brain regions tested. These parameters are in agreement with those previously selected by Badea and colleagues using *ex vivo* brain samples imaged at 9.4 Tesla.

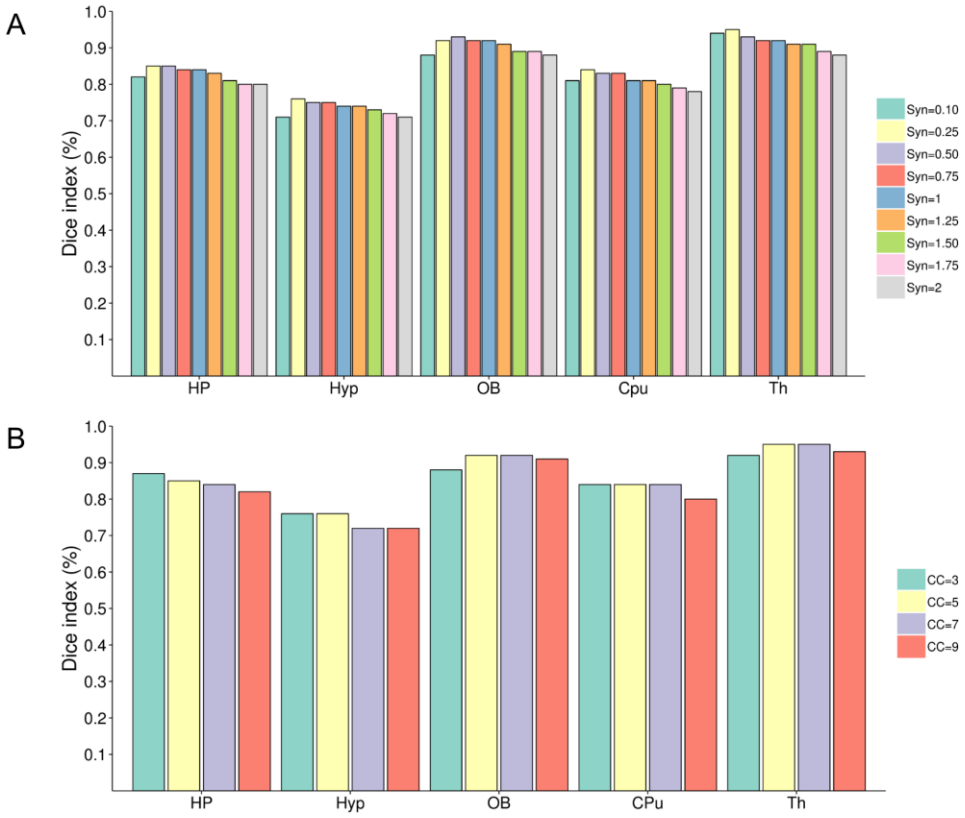

Figure 19. Optimization of registration parameters for anatomical labelling. *Accuracy of registration (Dice coefficient) for varying registration parameters (window radius for cross correlation and gradient steps). Top: as in Badea et al., (2012), we varied windows radius between 3 and 9 voxels. The chosen value (5 voxels) produces a good performance in all the brain regions tested. Bottom: the gradient step parameter for the symmetric normalization was varied between 0.10 and 2 voxels. The chosen parameter (0.5 voxels) produces a good performance in all the tested regions.*

Using these validated parameters, cross-strain volumetric analysis using anatomical labels from the two atlases highlighted the presence of a general reduction in cortical volume in BTBR mice with respect to B6 mice. Also major subcortical structures, including caudoputamen, hippocampus and hypothalamus reported a statistical significant reduction in volume (**Figure 20**). These results are in good agreement with recent comparative neuroanatomical mapping of these two strains performed by other labs (Ellegood, Babineau et al. 2013), where a similar significant decrease in the volume of cortex and corpus callosum was shown.

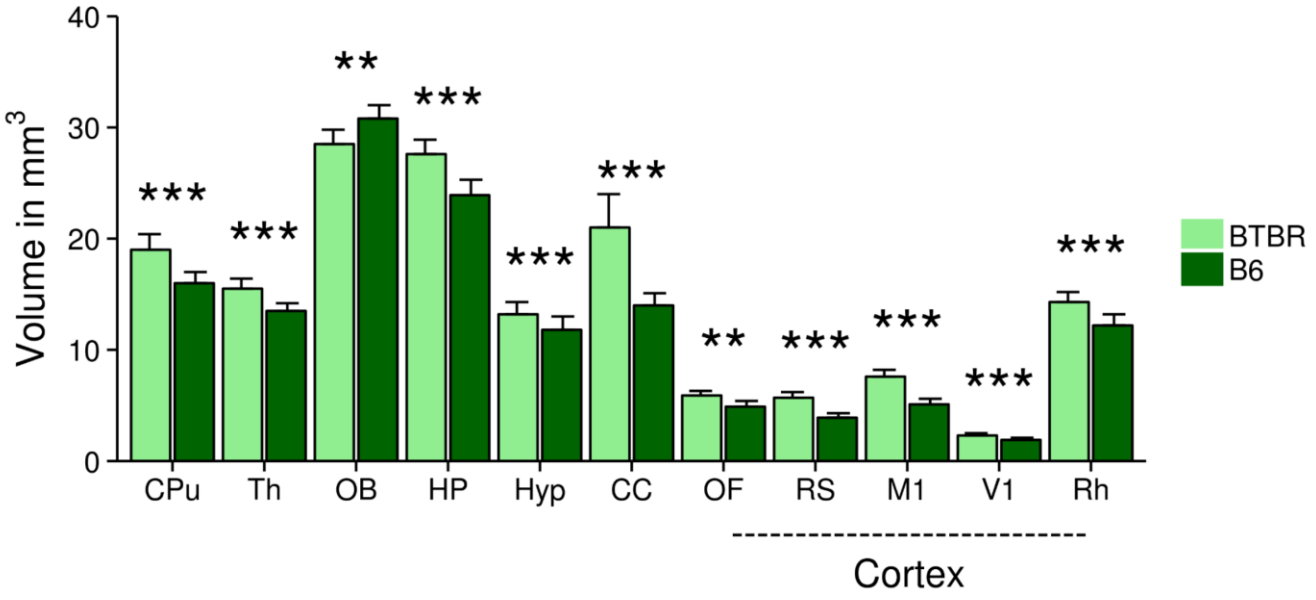

Figure 20. Anatomical labelling. *The labels of the reference atlas employed are warped into subjects' space via the study based template using the combination of affine and diffeomorphic mapping obtained after the registration process. The registered labels permit to calculate volumes of brain areas of interest and perform t-tests between the mouse samples. (Cpu: caudoputamen; Th: thalamus; OB: olfactory bulbs; HP: hippocampus; Hyp: hypothalamus, CC: corpus callosum; OF: orbitofrontal cortex; RS: retrosplenial cortex; M1: primary motor cortex; V1: primary visual cortex; Rh: rhinal cortex). **p<.01; ***p<.001).*

3.3.2. Voxel Based Morphometry

Whole-brain VBM revealed widespread and bilateral reductions in GM volume across dorsofrontal, cingulate, retrosplenial, occipital and parietal cortex (**Figure 21**, Z>3.1, p-corrected<.001), in BTBR compared to B6 controls. These findings are in agreement with the results of anatomical labelling. GM volume reductions were also evident in subcortical areas, including the lateral and posterior thalamus (longitudinal fasciculus), the posterior hypothalamus and the ventral hippocampus. Interestingly, VBM highlighted also small bilateral foci of increased GM volume in the olfactory bulbs, in the medial pre-frontal and insular cortex, in the amygdala and in the dorsal hippocampus. The detection of small focal effects that could not be revealed when integrated over large anatomical volumes is one of the main advantages

of the VBM approach over classic neuroanatomical volumetric mapping. These results are in good agreement with recent comparative neuroanatomical mapping of these two strains performed by other labs using tensor based morphometry (Ellegood, Babineau et al. 2013), which showed similar significant alterations (using Tensor Based Morphometry, see discussion below) in hippocampal and cortical areas.

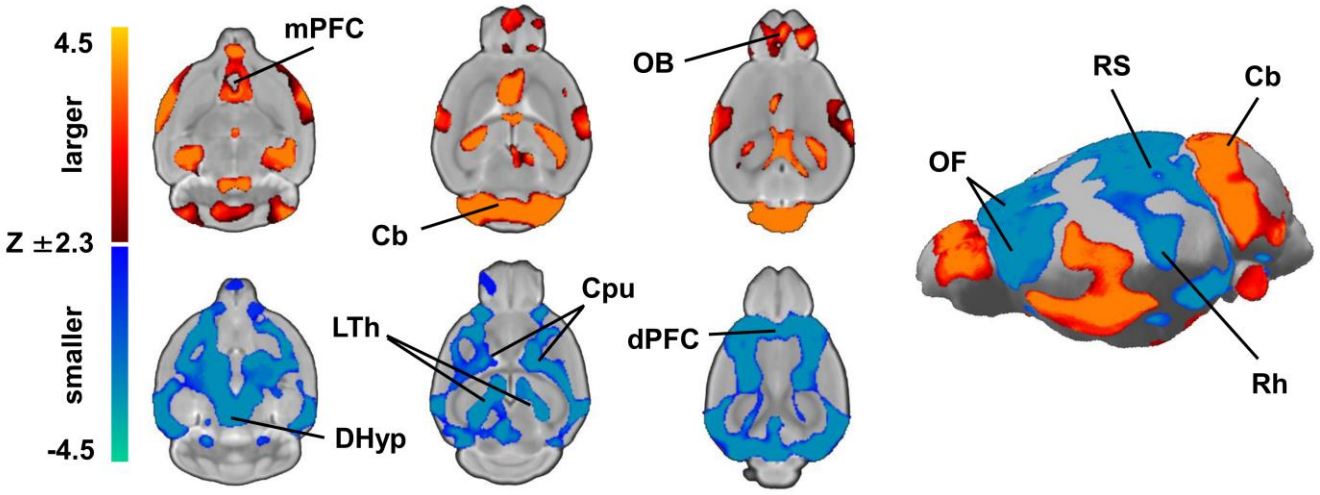

Figure 21. VBM. *Differences in local gray matter volumes are assessed combining gray matter probability maps and local Jacobian determinants. Statistical comparison (p<.01, threshold-free cluster enhancement followed by cluster-based thresholding) showed widespread and bilateral reductions in grey matter volumes across dorsofrontal, cingulate, retrosplenial, occipital and parietal cortex as well as in subcortical structures in BTBR compared to B6 controls. VBM highlighted also small bilateral foci of increased gray matter volume in the olfactory bulbs, in the medial pre-frontal and insular cortex, in the amygdala and in the dorsal hippocampus. (Cb: cerebellum; Cpu: caudoputamen; DHyp: dorsal hypothalamus; dPFC: dorsal prefrontal cortex; LTh: lateral thalamus; mPFC: medial prefrontal cortex; OB: olfactory bulbs; Rh: rhinal cortex; RS: retrosplenial cortex).*

3.3.3. Cortical Thickness Estimation

Further investigation of the presence of local alterations of GM in BTBR mice compared to B6 controls was performed in terms of cortical thickness estimation. Average spatially-normalized voxel-based thickness maps were calculated separately for each of the two strains and three-dimensionally rendered for visualization purposes (**Figure 22**). In good agreement

with the results of automated anatomical labelling and VBM mapping, a widespread reduction in mean cortical thickness (Z>2.3, p-corrected<0.01) was observed in BTBR mice compared to B6 controls. Importantly, inter-group voxel-wise statistics revealed significantly increased cortical thickness in medial prefrontal and insular regions in the BTBR cohort (Z>2.3, p-corrected<0.01).

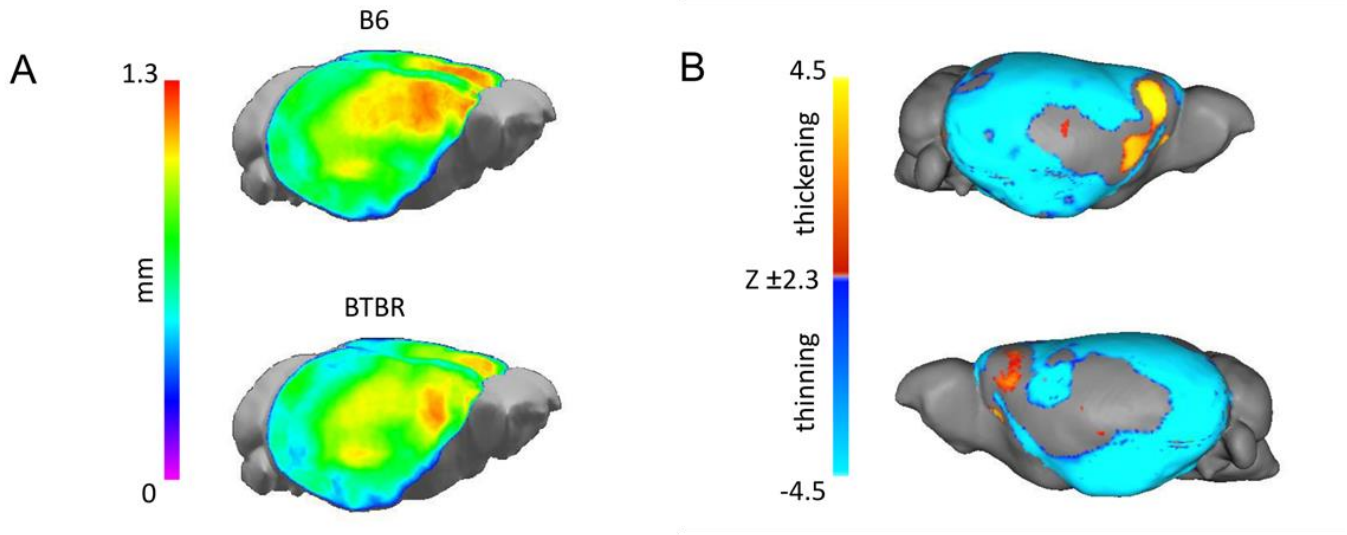

Figure 22. Cortical thickness estimation. *Three-dimensional rendering views of average cortical thickness in BTBR and B6 mice (a). Statistical comparison showed significant cortical thickness thinning (p<0.01, threshold-free cluster enhancement followed by cluster-based thresholding) in parietal, temporal and peri-hippocampal cortex of BTBR mice. Increased thickness was observed in medial prefrontal and anterior insular regions of this strain (b).*

2.4. Discussion

Here we described semi-automated procedures for automated anatomical labelling, VBM and cortical thickness estimation in the mouse brain. The approach has been recently applied to detect fine-grained morphoanatomical alterations in different mutant mouse lines, including alterations in β-catenin mouse mutants (Tucci, Kleefstra et al. 2014), acallosal and socially-impaired mice (Dodero, Damiano et al. 2013) and to identify sexually divergent effects on cortical anatomy in catechol-O-methyltransferase mutant lines (Sannino, Gozzi et al. 2014). In

the latter study, we showed remarkably consistent intergroup differences in regional GM volume as assessed with our VBM pipeline, or manual morphometric measurements of cortical thickness in post-mortem brain slices (Sannino et al., 2014), thus underscoring the accuracy and sensitivity of our workflow.

The image processing described here adopts the methodologies and toolkits originally developed for human brain imaging and can be straightforwardly extended to other areas of research and mouse models of disease. For example, we also used VBM to describe symmetric scMRI networks in the cortex of inbred mice complementary to those previously identified in humans, providing a new tool to study gray matter disrupted connectivity in brain disorders with transgenic mice (Pagani, Bifone et al. 2016). Although prominent examples of the use of morphoanatomical methods in the mouse have been recently described by other labs (Nieman, Bock et al. 2005, Delatour, Guegan et al. 2006, Johnson, Ali-Sharief et al. 2007, Borg and Chereul 2008, Sawiak, Wood et al. 2009, Lee, Ruffins et al. 2010, Lerch, Sled et al. 2011, Badea, Gewalt et al. 2012, Budin, Hoogstoel et al. 2013, Sawiak, Wood et al. 2013, Oguz and Sonka 2014), the vast majority of these contribution lack a detailed description of the complex workflow required to process and analyse different morphoanatomical readouts, thus complicating the replication of these methods by other groups. The methodological workflow presented in this work was designed to facilitate the implementation of fine-grained morphoanatomical mapping tools by non-expert users, and promote forward and back translation of MRI preclinical and clinical research evidence. We also point out that a preliminary account on the implementation of these procedures in parallel computing cloud environment has been recently reported (Minervini, Rusu et al. 2014), a strategy that can streamline and accelerate image processing time by exploiting large high-performance-computing infrastructures.

A dominant feature of our unified approach is the coupling of standard intensity based affine registration with a symmetric diffeomorphic normalization algorithm to obtain optimal MR image registration (Avants, Epstein et al. 2008). This approach, which has been successfully employed both in human (Kim, Avants et al. 2008, Klein, Andersson et al. 2009, Klein, Ghosh et al. 2010) and small animal imaging studies (Avants, Yushkevich et al. 2010, Lerch, Yiu et al. 2011), is based on the ANTs open source software library and is adopted to create a study based template, carry out skull stripping and perform anatomical labelling via label propagation. Our cortical thickness estimation approach is also registration-based, and employs DiReCT, an advanced diffeomorphic registration algorithm implemented in ANTs toolkit that has been recently validated on human imaging data (Das, Avants et al. 2009) and used for research studies with clinical population (Avants, Cook et al. 2010). To the best of our knowledge, this is the first example of the application of this approach to map cortical thickness in small rodent species.

The cortical thickness mapping and anatomical labelling approaches employed rely on the availability of three dimensional labelled MRI atlases with delineated cortical and subcortical morphology. While a universally accepted MRI atlas of the mouse brain is still not available, a number of mouse brain MRI atlases have been published based on high resolution acquisitions of a single subject (Maheswaran, Barjat et al. 2009, Xie, Yang et al. 2010, Zhang, Peng et al. 2010, Badea, Gewalt et al. 2012) or constructed from several animals, with data gathered either *in vivo* (Ma, Smith et al. 2008, Aggarwal, Zhang et al. 2009, Maheswaran, Barjat et al. 2009) or from *ex vivo* fixed specimens (Kovacevic, Henderson et al. 2005, Badea, Ali-Sharief et al. 2007, Dorr, Lerch et al. 2008, Aggarwal, Zhang et al. 2009, Johnson, Badea et al. 2010, Ullmann, Watson et al. 2013). In this study, a combination of two atlases was employed to obtain a fine-grained parcellation of both cortical (Ullmann et al., 2013) and subcortical (Dorr, Lerch et al.

2008, Ullmann, Watson et al. 2013) regions. However, our method is not atlas-dependent and can be flexibly adapted to a number of published or custom mouse brain MRI anatomical partitions.

An important benefit of our approach is the possibility to measure different and complementary morphoanatomical brain metrics - including volumetric analysis, VBM and cortical thickness - in a single reference space. This aspect is of crucial importance, as it broadens the scope of application of MRI-based brain morphometry and it augments its translational potential by permitting a multi parametric comparison with analogous clinical readouts. In the illustrative example reported here, an overall agreement between the three readouts was found. Apparent discrepancies between readouts (e.g., the lack of inter-strain differences in insular volume, due to the presence of VBM foci of increased and decreased regional volume in anterior and posterior portions of this region) are the result of different sampling scales (label vs. voxel level) of the readouts employed. We also note that the combination of complementary approaches can help disambiguate morphological alterations of pathological origin, as the relationship between thickness and local GM volume has not been thoroughly clarified, and may probably change across pathologies and populations (Hutton, De Vita et al. 2008). Within this scenario, the use of complementary metrics coupled to histological staining can help to pinpoint the pathological bases of brain morphometric changes of neuropathological origin.

In addition, our preprocessing workflow can be straightforwardly extended to perform tensor based morphometry (TBM). As in VBM, TBM entails the local computation of the Jacobian determinants of the deformation field used to map subjects' images to the study based template. The Jacobian determinant (i.e. the local scaling factor) encodes for local anatomical expansions and contractions of subjects' areas relative to the study based template, and therefore Jacobian maps can be used to localize inter-group differences in the local shape of

brain structures at the voxel level. TBM analysis can be simply performed by omitting the tissue segmentation step in the VBM procedure herein described. As TBM does not entail tissue classification, it can be used for the simultaneous investigation of WM and GM alterations, and may robustly detect alterations in areas of mixed WM-GM structures, such as the thalamus and brain stem, which are especially sensitive to the accuracy of intensity based tissue classification algorithms.

A few methodological limitations in our approach deserved to be mentioned. The procedure described here has been developed and optimized or fixed *ex vivo* brain samples imaged at 7 Tesla using T2-weighted images. While the application of our workflow to different field strengths and image contrast is conceivable, adjustments in single preprocessing parameters may be required to adapt our procedure to different contrast mechanisms or images acquired at different field strengths. One limitation of our cortical thickness mapping is its poor performance in resolving thickness at the level of inter-hemispheric fissure in medial regions of the mouse cortex such as cingulate or retrosplenial areas (**Figure 17**). As a result, inter-group differences in cortical thickness in these regions should be interpreted with caution. Researchers interested in mapping gray matter alterations in these regions with high confidence, should consider cross validating thickness mapping with voxelwise methods described in our workflow that are immune to this limitation, such as VBM and TBM. Similarly, the segmentation of the anterior cingulate in acallosal mice such as BTBR should be considered tentative, as the lack of clear white matter gray matter boundary prevents an empirical assessment of its accuracy. Once again, voxelwise-based morphoanatomical mapping together with histological measurements can help validate cortical thickness measurements in these areas when acallosal mice are employed. Caution should also be exercised in interpreting inter-group differences in mouse models characterized by profound demyelination and

neurodegeneration, two conditions that can reduce GM/WM contrast and affect segmentation accuracy for VBM. Notwithstanding these limitations, the possibility of using a unified workflow to map multiple complementary morphoanatomical parameters should be emphasized as a major point of strength of our approach, owing to the possibility of cross-comparing different readouts to dissect specific neuroanatomical features with increased confidence.

In conclusion, we described a registration-based approach for anatomical mapping, VBM and cortical thickness estimation in the mouse brain. The application of these procedures enabled the identification of subtle volumetric differences across subjects without prior knowledge of structures of interest. Our unified approach based on diffeomorphic registration permits to integrate complementary MR morphoanatomical techniques, and is based on popular open source software (ANTs), which has been extensively employed in priori MRI morphometric studies. The detailed operational workflow described in the present work is expected to help the implementation of rodent morphoanatomical methods by non-expert users, thus ultimately promoting the use of these tools across the preclinical neuroimaging community.

3. VBM Applied to Aged Mice Treated with Omega-3

All the material presented in this chapter has been recently published in the article “All the material presented in this chapter has been recently published in the article “Cutuli D, **Pagani M**, Caporali P, Galbusera A, Laricchiuta D, Foti F, Neri C, Spalletta G, Caltagirone C, Petrosini L, Gozzi A (2016). Effects of Omega-3 Fatty Acid Supplementation on Cognitive Functions and Neural Substrates: A Voxel-Based Morphometry Study in Aged Mice, Frontiers in Aging Neuroscience, 4:8-38”

Human and experimental studies have revealed putative neuroprotective and pro-cognitive effects of omega-3 polyunsaturated fatty acids (n-3 PUFA) in aging, evidencing positive correlations between peripheral n-3 PUFA levels and regional grey matter (GM) volume, as well as negative correlations between dietary n-3 PUFA levels and cognitive deficits. We recently showed that n-3 PUFA supplemented aged mice exhibit better hippocampal-dependent mnesic functions, along with enhanced cellular plasticity and reduced neurodegeneration, thus supporting a role of n-3 PUFA supplementation in preventing cognitive decline during aging. To corroborate these initial results and develop new evidence on the effects of n-3 PUFA supplementation on brain substrates at macro-scale level, here we expanded behavioral analyses to the emotional domain (anxiety and coping skills), and carried out a fine-grained regional GM volumetric mapping by using high-resolution MRI-based voxel-based morphometry. The behavioral effects of 8 week n-3 PUFA supplementation were measured on cognitive (discriminative, spatial and social) and emotional (anxiety and coping) abilities of aged (19 month-old at the onset of study) C57B6/J mice. n-3 PUFA supplemented mice showed better mnesic performances as well as increased active coping skills. Importantly, these effects were associated with enlarged regional hippocampal, retrosplenial and prefrontal GM volumes, and with increased post mortem n-3 PUFA brain levels. These findings indicate that increased dietary n-3 PUFA intake in normal aging can improve fronto-hippocampal GM structure and

function, an effect present also when the supplementation starts at late age. Our data are consistent with a protective role of n-3 PUFA supplementation in counteracting cognitive decline, emotional dysfunctions and brain atrophy. Importantly, the present findings also suggest the efficacy of our pipeline in detecting gray matter variations of neurobiological relevance.

3.1. Background

The constant worldwide growth of the elderly population has amplified the interest in the prevention and improvement of age-related cognitive decline. Such a process is characterised by a progressive and irreversible loss of grey matter (GM) in many brain regions, with a prominent atrophy of the hippocampus and prefrontal lobes (Jernigan, Archibald et al. 2001, Driscoll, Howard et al. 2006, Masliah, Crews et al. 2006). Research on environmental factors that affect age-related cognitive decline has aroused growing interest in cost-effective interventions, such as nutritional supplementation (Gómez-Pinilla 2008, Maruszak, Pilarski et al. 2014).

As major components of neuronal membranes and key modulators of neuroinflammation, oxidative stress, and neurogenesis (Luchtman and Song 2013, Denis, Potier et al. 2015), omega-3 polyunsaturated fatty acids (n-3 PUFA), particularly docosahexaenoic acid (DHA), eicosapentaenoic acid (EPA) and docosapentaenoic acid (DPA), may exert beneficial and neuroprotective effects on the aging brain. Consistently, rodent studies have shown that n-3 PUFA supplementation improves neurogenesis and synaptogenesis, executive functions and learning abilities, while n-3 PUFA deficiency is associated with memory deficits and impaired hippocampal plasticity (Fedorova and Salem 2006, Hooijmans, Pasker-de Jong et al. 2012, Denis, Potier et al. 2013, Luchtman and Song 2013, Maruszak, Pilarski et al. 2014). Human longitudinal studies based on direct or indirect indices of n-3 PUFA consumption have also

provided evidence of n-3 PUFA beneficial role in aging. Namely, increased n-3 PUFA consumption correlates with better cognitive functioning and reduced risk for dementia (Dullemeijer, Durga et al. 2007, Whalley, Deary et al. 2008, Cunnane, Plourde et al. 2009, Kröger, Verreault et al. 2009, Samieri, Maillard et al. 2012), higher total brain and regional GM volumes (Conklin, Gianaros et al. 2007, Samieri, Maillard et al. 2012, Tan, Harris et al. 2012, Titova, Sjögren et al. 2013, Pottala, Yaffe et al. 2014) and reduced white matter (WM) hyperintensity (Virtanen, Siscovick et al. 2013). However, interventional studies aimed at establishing a causative effect of n-3 PUFA supplementation on GM volumes and cognitive functions have produced inconclusive results. In fact, although some studies reported that n-3 PUFA supplementation improves cognition in healthy elderly subjects (Yurko-Mauro, McCarthy et al. 2010, Witte, Kerti et al. 2013) and in patients with mild cognitive impairment (Chiu, Su et al. 2008), other studies failed to reveal any significant effect in healthy subjects (van de Rest, Geleijnse et al. 2008, Dangour, Allen et al. 2010, Geleijnse, Giltay et al. 2012) and in patients with Alzheimer's disease (AD)(Quinn, Raman et al. 2010). Uncontrolled confounding factors, such as socio-economic status, genetic background as well as healthy habits and lifestyle (e.g., exercise, not smoking, sleep, social support, use of vitamin supplement, etc.) may contribute to these inconsistent results and make it difficult to isolate the specific neuroprotective impact of n-3 PUFA-enriched diet on cognitive functions of elderly people (Denis, Potier et al. 2013, Raji, Erickson et al. 2014). Furthermore, the enormous variation in n-3 PUFA supplement kind and dosage, and a general failure in controlling for n-6 PUFA dietary intake may also account for the huge variability in human clinical and interventional studies.

As a result, the impact of n-3 PUFA supplementation on cognitive functions in the aging human brain and the underlying neuronal substrates is still a matter of debate. Studies under controlled environmental and genetic conditions in animal models can help to disambiguate the complex

relationships among n-3 PUFA intake, cognitive performance and GM morphometry. We recently demonstrated that 8-week n-3 PUFA supplementation in aged mice robustly ameliorates hippocampal functions via increased neurogenesis and reduced neurodegenerative processes (Cutuli, De Bartolo et al. 2014). However, whether cellular-scale hippocampal changes can result in macro-scale structural alterations detectable through volumetric MRI, and whether n-3 PUFA effects are limited to hippocampal areas or affect other neocortical and/or subcortical regions remain to be determined.

In order to address these issues, in the present study MRI volumetric measures of the entire brain (and not just of hippocampal regions) as well as cognitive and emotional functions not previously evaluated were assessed. To this aim in aged inbred mice undergoing n-3 PUFA supplementation with respect to isocaloric control conditions we measured cognitive abilities in different spatial and discriminative tasks, and in tasks assessing sociability and social memory. Age-related disorders are in fact reported to affect social memory abilities (Riedel, Kang et al. 2009). Notably, since in older populations cognitive decline is frequently associated with depressive-like symptoms (Steffens, Otey et al. 2006) and n-3 PUFA are reported to exert antidepressant action (Freeman, Hibbeln et al. 2006, Sublette, Ellis et al. 2011), the behavioral assessment was extended to emotional competencies in facing coping skills. A control of anxiety levels was also performed. Then, regional GM volumes were mapped by using high resolution MRI-based whole-brain voxel-based morphometry (VBM). Finally, *ex vivo* brain levels of n-3 PUFA and individual behavioral scores were correlated with regional GM volumes to assess whether n-3 PUFA levels can be considered reliable predictors of volume changes and behavioral outcomes.

3.2. Materials and Methods

3.2.1. Ethical Statement

All experimental procedures were performed in accordance with the Italian law (D.L. 116, 1992 Italian Ministry of Health, Rome), and in agreement with the European Union Directive (2010/63/EU). All surgical procedures were performed under deep anesthesia and all efforts were made to minimize suffering and reduce the number of animals that were used. All experimental procedures were approved by the Italian Ministry of Health (Ministerial Decree number 232/2012-B, 10-2012).

3.2.2. Animals

Male aged C57B6/J mice (19 month-old at the onset of study; 35.57 ± 0.69 g) were used in the present research (Charles River Laboratories, Italy). The animals were group-housed (three-four mice/cage) with temperature (22-23°C) and humidity controlled (60 ± 5%), under a 12:12 h light/dark cycle with free access to food and water. Animals were randomly divided in two groups: 1) mice supplemented with an n-3 PUFA mixture by daily gavage for 8 weeks (5 day/week) (Group name: n-3 PUFA; n = 11); 2) mice supplemented with olive oil by daily gavage for the same period used as controls of an isocaloric intake, as reported in previous studies (Kotani, Sakaguchi et al. 2006, Oarada, Tsuzuki et al. 2008, Nakamoto, Nishinaka et al. 2010, Sinn, Milte et al. 2010, Danthiir, Burns et al. 2011, Vinot, Jouin et al. 2011, Cutuli, De Bartolo et al. 2014) (Group name: Control; n = 10) (Fig. 1). Animals' weight was recorded weekly throughout the study. No significant differences between groups were found in mice body weight during the entire experimental period (two-way ANOVA (group x week): group: $F_{1,19}$ = 0.32, p = 0.58; week: $F_{9,171}$ = 3.57, p = 0.0004; interaction: $F_{9,171}$ = 0.47, p = 0.89).

Food supplementation was performed by daily gavage to ensure that all cagemates received the same controlled amount of dietary supplements regardless of social hierarchy or appetitive drive. n-3 PUFA group was supplemented with a volume of 0.015 ml of fatty acids mixture (Pfizer, Italy) corresponding to a dose of 360 mg/kg/day of n-3 PUFA (Calviello, Palozza et al. 1997) mainly constituted by eicosapentaenoic acid (EPA, 20:5 n-3; 63%), docosahexaenoic acid (DHA, 22:6 n-3; 26%), docosapentaenoic acid (DPA, 22:5 n-3; 4%), and α-linolenic acid (ALA, 18:3 n-3; 1%) (Cutuli, De Bartolo et al. 2014). Control group was supplemented with the same volume of olive oil (Trasimeno, Italy) containing ≈ 4 mg/kg/day of n-3 PUFA constituted only by ALA (1%) (Cutuli, De Bartolo et al. 2014). The two groups of animals were fed ad libitum with standard food pellets (Mucedola 4RF21 standard diet GLP complete feed for mice and rats; Mucedola, Italy).

3.2.3. Behavioral Testing

Starting from the 5th supplementation week, mice were tested in a number of behavioral tasks tapping distinct cognitive and emotional functions: Dark/Light test, Y-maze test with objects, Morris Water Maze (MWM), Sociability and Social Memory test, Elevated Plus Maze (EPM), and lastly Porsolt test. After behavioral testing, the animals were sacrificed to perform VBM and biochemical analyses.

Dark/Light test

At the beginning of behavioral testing, anxiety levels and exploratory behaviors were tested by means of the Dark/Light test that is based on the innate rodent tendency to avoid brightly illuminated areas and to spontaneously explore novel environment (Crawley and Goodwin 1980). Dark/Light test was performed in an apparatus consisting of a parallelepiped box containing two compartments: a dark compartment (18x42x21 cm) with black walls, and a lighted compartment (36x42x21 cm) with white walls. The two compartments were separated

by a wall pierced with an open door (7x7 cm). The mouse was placed in the lighted compartment facing the wall and allowed to freely explore both compartments for 10 min. The following parameters were analyzed: time spent in each compartment; latency of first entrance into the dark compartment; number of transitions to the dark compartment; number of defecations.

Y-Maze test with objects

To assess novel object recognition memory we used a Y-Maze test with objects (Winters and Bussey 2005). The Y-Maze apparatus was made of grey Plexiglas and consisted of three identical arms (8x30x15 cm) with a 120° angle between adjacent arms. The three arms were designated as: start arm, from which the mouse started to explore the maze, and two choice arms, containing or not objects. Y-Maze test with objects was performed in a dimly lighted room and consisted of three trials. During the first trial (habituation phase) lasting 5 min the mice placed in the start arm were allowed to freely explore the Y-Maze arms containing no objects. After 3 min-inter-trial interval (ITI) the mice underwent the second trial (training phase) lasting 5 min during which moving from the start arm they were allowed to explore two identical objects put at the end of the choice arms. After 1 h-ITI the mice underwent the last 5 min-trial (retention phase) during which they were allowed to freely explore one copy of the familiar object and a novel object put at the end of the choice arms. During the ITI mice were put in their homecages. Maze floor and walls were cleaned after each trial to remove olfactory cues. Trials were recorded by a ceiling-mounted camera and analyzed by a video analyzer (Ethovision XT, Noldus, The Netherlands). To evaluate the preference for the novel object (novelty) total time spent in contact with the familiar vs. novel object during the retention phase was analyzed. The discrimination index was calculated: contact time with the novel object (Tno) minus contact time with the familiar one (Tfo)/total contact time with both objects.

Morris Water Maze (MWM)

MWM test is a well validated test to assess localizatory abilities in rodents during aging (Chen, Chen et al. 2000, Carrie, Smirnova et al. 2002). The mice were placed in a circular white pool (diameter 140 cm) filled with 24°C water made opaque by the addition of atoxic acrylic white color (Giotto, Italy). An escape platform (diameter 5 cm) with a rough surface was placed in the middle of the NW quadrant 20 cm from the side walls. It was submerged 0.5 cm under the water level. The pool located in a room uniformly lighted by four lamps (25 W each) was surrounded by several extra-maze cues. The water maze was surmounted by a video camera whose signal was relayed to a monitor and to the image analyser (Ethovision XT, Noldus, The Netherlands). The protocol consisted of a 16-trial Place phase and a 1-trial Probe phase. During the Place phase, mice were submitted to four consecutive sessions made by four 60 s-trials (with 30 s-ITI). During the 15 min-inter-session interval mice were put in their home cages. At the beginning of each trial, mice were gently released into the water from pseudo-randomly varied starting points and were allowed to swim around to find the hidden platform. Mice that did not locate the platform within 60 s were gently guided there by the experimenter. After mice climbed the platform, they were allowed to remain on it for 30 s. After 24 h, mice were submitted to the Probe phase, in which the platform was removed and the mice were allowed to search for it for 30 s. To evaluate localizatory memory the following MWM parameters were analyzed: time spent and distance swum to reach the platform during the Place phase; distance swum in the previously rewarded quadrant during the Probe phase. The navigational strategies were classified in three main categories, regardless of whether the platform was reached or not: Circling (C): circular swimming with inversion of direction and counter-clockwise and clockwise turnings; Searching (S): swimming around the pool in all or some quadrants, visiting the same area more than once; direct Finding (F): swimming towards the platform without any foraging around the pool. Two researchers unaware of the individual specimen's group categorized the

swimming trajectories drawn by the image analyzer. They attributed the dominant behavior in each trial to a specific category. Categorization was considered reliable only when their judgments were consistent.

Sociability and social memory test

Sociability and social memory test assesses social motivation and interest in social novelty, respectively (Nadler, Moy et al. 2004, Cutuli, De Bartolo et al. 2013). Rodents normally prefer to spend more time with another rodent (sociability) and investigate a novel intruder more than a familiar mouse (social novelty). Age-related disorders are reported to affect social memory abilities (Riedel, Kang et al. 2009). The apparatus consisted of a white rectangular wooden box (54x42x21 cm) divided in three 18 cm-wide chambers by two transparent Plexiglas walls with an open middle door (3.5x3.5 cm). Each lateral chamber contained a small metal cage (9x8 cm) with mesh-like holes in which stranger mice were confined for social interactions. The test comprised 3 trials: habituation, Sociability and Social Memory Test (SMT). During the habituation trial, the mice were allowed to freely move in the apparatus for 5 min. During Sociability trial, an unfamiliar juvenile (35-45 pnd) mouse conspecific (Stranger 1) was placed inside the small metal cage in one of the lateral chambers (randomly selected and counterbalanced for each group). The experimental mouse was placed in the apparatus and it was allowed to freely explore the three chambers and contact the small metal cages for 5 min. During SMT, another unfamiliar juvenile mouse (Stranger 2) was placed inside the metal cage in the opposite lateral chamber that was empty during the Sociability session. The experimental mouse was allowed to freely move and contact the metal cages for 5 min. ITI between habituation and Sociability trials lasted 3 min, while ITI between Sociability trial and SMT lasted 1 h. Mice behavior was recorded by a video camera mounted on the ceiling. The resulting video signal was relayed to a monitor and to an image analyzer (Ethovision XT, Noldus, The

Netherlands). Time spent in each lateral chamber during Sociability and SMT was recorded. Discrimination indexes were calculated: sociability index = contact time with the Stranger 1 (TS1) minus contact time with the empty cage (Te)/total contact time; social memory index = contact time with the Stranger 2 (TS2) minus contact time with the Stranger 1 (TS1)/total contact time.

Elevated Plus Maze (EPM)

EPM is a well validated test to assess anxiety levels in rodents based on their natural aversion to open spaces (Ruehle, Remmers et al. 2013, Cutuli, De Bartolo et al. 2014). The maze was formed by a wooden structure in the shape of a cross with a central platform and four 35x6 cm arms raised 100 cm above the ground. The north and south arms were open, the east and west arms were enclosed by walls 20 cm high. During a 5-min trial the mouse was placed in the central platform and allowed to freely explore the maze. Since mice avoid open areas by confining movements to enclosed spaces or to the edges of a bounded space, a typical mouse tends to spend the majority of trial time in the closed arms. The entire apparatus was cleaned after each trial to remove olfactory cues. Trials were recorded by a ceiling-mounted camera and analyzed by an image analyzer (Ethovision XT, Noldus, The Netherlands). The following EPM parameters were measured: total entries and total time spent in the open and closed arms; number of defecations.

Porsolt test

Mice were gently placed in individual glass cylinders (height 40 cm; diameter 18 cm) containing 20 cm water at 28±2°C. Mice were exposed to the apparatus for 10 min. At the end of the test mice were removed from the cylinder, allowed to dry in a small cage placed under a heat source and returned to their homecages. The behavior exhibited by each animal during the test was recorded by using a frontally-mounted camera. Later, an observer blind to the treatment

received by each animal manually scored the videos (Ethovison XT, Noldus, The Netherlands). Duration and frequency of the following behaviors were taken into account (Keers, Pedroso et al. 2012, Costa, Vieira et al. 2013): - passive behaviors: immobility = total absence of movement; paddling = small movements of one of the posterior paws not producing displacement; - active behaviors: swimming = large and horizontal movements of the paws leading to displacement of the body around the cylinder; climbing = vigorous vertical movements of the forepaws, directed against the wall of the tank, leading to displacement the body around the cylinder.

3.2.4. MR Acquisition and Image Analysis

High-resolution morpho-anatomical T2-weighted MR imaging of ex vivo mouse brains was performed in paraformaldehyde (4% PFA; 100 ml) fixed specimens. Standard sample preparation and MRI acquisition have been recently described (Dodero et al., 2013). Briefly, C57Bl/6 mice supplemented with n-3 PUFA (all 87-week-old) and age-matched controls supplemented with olive oil were deeply anaesthetized with an intraperitoneal avertin injection (375 mg/kg) and their brains were perfused in situ via cardiac perfusion. The perfusion was performed with phosphate buffered saline followed by paraformaldehyde (4% PFA; 100 ml). Both perfusion solutions were added with a Gadolinium chelate (Prohance, Bracco, Milan) at a concentration of 10 and 5 mM, respectively, to shorten longitudinal relaxation times. Brains were imaged inside intact skulls to avoid post-extraction deformations. A multi-channel 7.0 Tesla MRI scanner (Bruker Biospin, Milan) was used to acquire anatomical images of the brain, using a 72 mm birdcage transmit coil, a custom-built saddle-shaped solenoid coil for signal reception, and the following imaging parameters: FLASH 3D sequence with TR=17ms, TE=10ms, α=30°, matrix size of 260x160x180, field of view of 1.83x1.26x1.26cm and voxel size of 0.07 mm (isotropic).

Inter-group morpho-anatomical differences in local GM volumes were mapped with VBM (Ashburner and Friston, 2000) using ANTs (Avants et al., 2009). Registration-based VBM procedure on the mouse brain has been thoroughly described in the previous chapter and is briefly reported herein to provide a comprehensive description of all the experimental procedures involved.

First, all the high-resolution T2W images were corrected for intensity non-uniformity and skull stripped to remove extra-brain tissue. Second, a study-based template was created aligning pre-processed images to a common reference space using affine and diffeomorphic registrations. Third, individual images of the two groups were registered to the study-based template using affine and diffeomorphic registrations. Fourth, spatially normalized images were segmented to calculate tissue probability maps using Markov Random Field to enforce the spatial smoothing of the tissues. The separation of the different tissues is improved by initializing the process with the probability maps of the study based template previously segmented. Fifth, the Jacobian determinants of the deformation field were extracted and applied to modulate the grey matter probability maps calculated during the segmentation. This procedure allowed the analysis of grey matter probability maps in terms of local volumetric variation instead of tissue density. Jacobian determinants were also normalized by the total intracranial volume to further eliminate overall brain volume variations. Sixth, the resulting modulated grey matter probability maps were smoothed using a Gaussian kernel with a sigma of three voxel width and employed for voxel-wise statistics and thresholded with a cluster-based procedure as implemented in FSL.

Regional GM volume differences between n-3 PUFA and olive oil supplemented mice were mapped using a two-sample t-test ($p < 0.01$) followed by a cluster correction using a significant cluster threshold of $p=0.01$ (Worsley et al., 1992). To ensure inter-group differences were not

due to segmentation-artefacts reflecting indirect alterations in grey matter intensity, we performed tensor based morphometry (TBM) on the same subjects. TBM is a procedure that does not require tissue segmentation and can be used to map inter-group differences in local brain volume independent of the nature of the tissue quantified. The pre-processing steps employed for TBM are the same of VBM, with the exception of the segmentation, which is not performed.

To assess the correlations among the regional GM volumes, n-3 PUFA level and behavioral performances, we also performed voxel-wise Pearson's correlation mapping by using individual n-3 PUFA brain concentration levels and behavioral scores as regressors ($p < 0.05$, followed by cluster level significance correction with a threshold of $p = 0.01$). To explicit the correlative relationship between variables obtained in univariate maps, mean GM volumes were quantified in representative bilateral cubic (9x9x9voxels) regions of interest (ROIs) centered in hippocampal foci exhibiting inter-group differences or areas of significant correlation. The exact anatomical location of the hippocampal ROIs selected for correlations is shown in **Figure 23.**

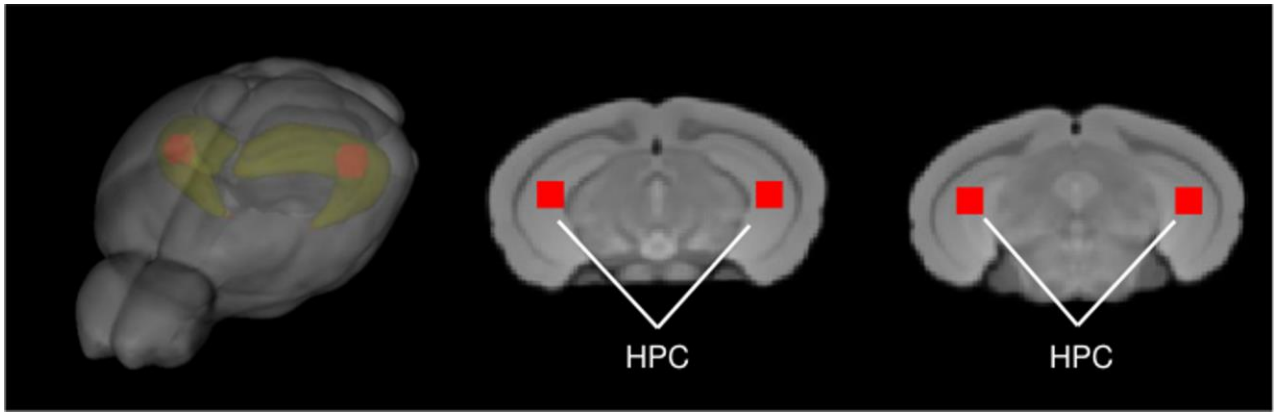

Figure 23. Anatomical location of the hippocampal bilateral cubic ROIs. *Three-dimensional rendering and slice representation of the anatomical location of the bilateral cubic (9x9x9 voxels) ROIs centred in hippocampal foci exhibiting significant correlations with behavioral scores and PUFA ($p < 0.01$, cluster-based correction at a significance level of 0.01). HPC = hippocampus.*

3.2.5. n-3 PUFA Quantification by GC/MS

After imaging, the brain content of n-3 PUFA was quantified. Fatty acids were extracted using the method reported by Folch (Folch, Lees et al. 1957) with slight modifications. Briefly, brains were homogenized in CHCl3/MeOH (2:1 v/v) to a final dilution of 20-fold of the original sample volume, assuming that the tissue has the same specific gravity of water. Heptadecanoic acid was used as internal standard. The resulting organic phase was evaporated to dryness in a speed-vac at room temperature and then derivatized with BSTFA-TMCS 99:1 v/v (Sigma-Aldrich, Italy) for 1 hour at 60°C. Derivatized samples were transferred in the injection vial and added with 20% v/v of Acetone. GC/MS analyses were performed using a Focus GC (Thermo Scientific, USA) equipped with 30 m×0.25 mm fused silica capillary column SLBTM-5MS (Supelco) and connected to a PolarisQ mass spectrometer (Thermo Scientific, USA). 2µL of samples were injected in split mode (1:10 ratio), the injector temperature was set at 200°C; the carrier gas was Helium and the flow rate was maintained constant at 1ml/minute. The initial oven temperature of 100°C was held for 1 minute and then raised to 250°C at 10°C/minute and maintained for 6 minutes. After then the oven temperature was increased up to 310°C at 20°C/minute and held for 5 minutes. Mass transfer line was maintained at 280°C and the ion source at 200°C. Analyses were performed in Selected Ion Monitoring (SIM) mode and fatty acids were identified by comparison with commercial standards.

All data were tested for normality (Shapiro-Wilk’s test) and homoscedasticity (Levene's test) and presented as mean ± SEM. Behavioral data and biochemical correlates were analyzed by using one- and two-way ANOVAs (with group as between-factor and compartment, session, strategy, arm and behavior as within-factors) followed by Tukey's HSD tests. Values of $p < 0.05$ were considered significant (Statistica 7, Statsoft).

3.3. Results

3.3.1. n-3 PUFA Supplemented Mice Exhibit Improved Cognitive Functions

To verify the ability of n-3 PUFA supplementation to improve mnesic function in the aged brain, both experimental aged mice groups were submitted to a battery of behavioral tests measuring hippocampal-dependent cognitive abilities **Figure 24**. n-3 PUFA supplemented mice demonstrated better novelty recognition abilities in the Y-Maze test with objects ($F_{1,19} = 6.13$, $p = 0.02$) as well as in the MWM. In the latter test, no inter-group differences were observed during Place in latency (group: $F_{1,19} = 0.52$, $p = 0.48$; session: $F_{3,57} = 4.85$, $p = 0.004$; interaction: $F_{3,57} = 0.74$, $p = 0.53$) and distance swum (group: $F_{1,19} = 0.17$, $p = 0.69$; session: $F_{3,57} = 17.23$, $p < 0.000001$; interaction: $F_{3,57} = 0.30$, $p = 0.82$) to reach the hidden platform. No differences were also observed in navigational strategies (group: $F_{1,19} = 1.55$, $p = 0.22$; strategy: $F_{2,38} = 310.94$, $p < 0.000001$; interaction: $F_{2,38} = 1.66$, $p = 0.20$), with Searching as the most used strategy (p=0.0001).

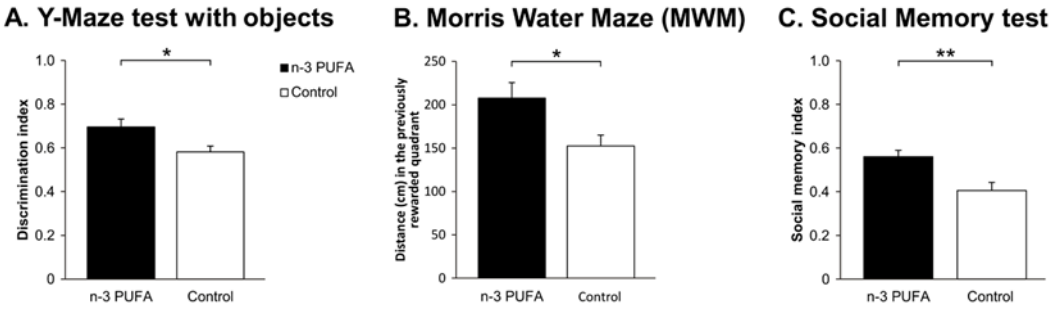

Figure 24. n-3 PUFA supplementation effects on mnesic performances. *A: Discrimination index in Y-Maze test with objects. B: Distance (cm) swum in the previously rewarded quadrant during Probe phase of MWM. C: Social memory index in SMT. Asterisks inside the graphs indicate the significance levels of comparisons between groups:* *p < *0.05,* **p ≤ *0.01.*

However, during Probe phase n-3 PUFA mice exhibited higher platform location retention as measured by distance swum in the previously rewarded (platform) quadrant ($F_{1,19} = 6.14$, $p =$

0.02), thus supporting a beneficial effect of n-3 PUFA supplementation on hippocampal mnesic functions. Accordingly, while all mice displayed an equal preference for social stimuli (sociability index: $F_{1,19}$ = 0.41, p = 0.53), n-3 PUFA supplementation significantly improved mnesic performances in SMT as indicated by the increased social memory index observed in n-3 PUFA supplemented mice ($F_{1,19}$ = 10.88, p = 0.004).

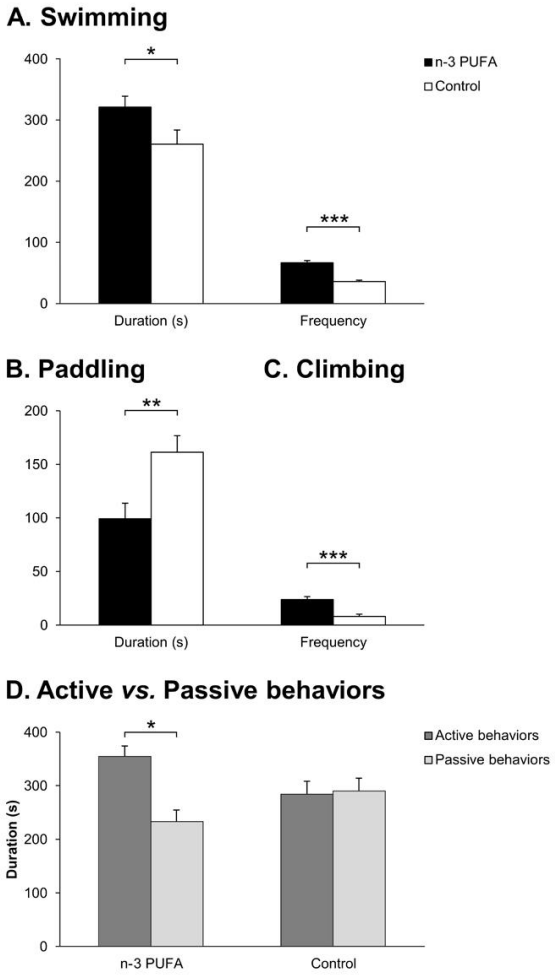

Figure 25. n-3 PUFA supplementation effects on coping skills. A: Swimming duration (s) and frequency in Porsolt test. B: Paddling duration (s). C: Climbing frequency. D: Active *vs.* passive behavior duration (s). Asterisks inside the graphs indicate the significance levels of comparisons between groups: *p < 0.05, **p ≤ 0.01, or ***p ≤ 0.001.

As reduced hippocampal volumes, depression and cognitive deterioration are frequently associated in older populations (Videbech and Ravnkilde 2004, Steffens, Otey et al. 2006),

Porsolt test was used to assess depressive-like behaviors and coping strategies in the two experimental groups (**Figure 25**). Depressive-like traits appeared to be less prominent in n-3 PUFA supplemented mice with respect to controls as evidenced by higher duration ($F_{1,19} = 4.69$, $p = 0.04$) and frequency of swimming ($F_{1,19} = 45.10$, $p < 0.000001$), as well as higher frequency of climbing ($F_{1,19} = 19.55$, $p = 0.0003$) and lower duration of paddling ($F_{1,19} = 8.61$, $p = 0.008$). No treatment differences were observed for the remaining parameters (immobility, duration: $F_{1,19} = 0.37$, $p = 0.55$; frequency: $F_{1,19} = 2.42$, $p = 0.14$; paddling, frequency: $F_{1,19} = 3.01$, $p = 0.09$; climbing, duration: $F_{1,19} = 1.47$, $p = 0.24$). Interestingly, ANOVA performed on active *vs.* passive behaviors (group: $F_{1,19} = 1.33$, $p = 0.26$; behavior: $F_{1,19} = 3.53$, $p = 0.08$; interaction: $F_{1,19} = 4.68$, $p = 0.04$) revealed that the total duration of active behaviors (swimming + climbing) was significantly higher than the total duration of passive behaviors (immobility + paddling) in n-3 PUFA supplemented mice than in controls ($p = 0.04$), indicating increased use of active coping strategies in n-3 PUFA supplemented mice.

Importantly, no inter-group differences in terms of anxiety levels and explorative behaviors were observed. In the Dark/Light test all mice spent more time in the dark compartment than in the lighted one (group: $F_{1,19} = 0.09$, $p = 0.76$; compartment: $F_{1,19} = 9.26$, $p = 0.007$; interaction: $F_{1,19} = 0.98$, $p = 0.33$), without differences in the latency of first entrance ($F_{1,19} = 1.87$, $p = 0.19$), number of transitions into the dark compartment ($F_{1,19} = 0.53$, $p = 0.48$), and total defecations ($F_{1,19} = 0.07$, $p = 0.79$). These findings were confirmed also in the EPM test during which all mice spent significantly more time in the closed than open arms (group: $F_{1,19} = 0.05$, $p = 0.82$; arm: $F_{1,19} = 1450.51$, $p < 0.000001$; interaction: $F_{1,19} = 0.12$, $p = 0.73$), showing similar total entries ($F_{1,19} = 0.03$, $p = 0.87$) and no differences in defecation number ($F_{1,19} = 2.59$, $p = 0.12$).

3.3.2. Treated Mice Exhibit Foci of Increased Hippocampal and Cortical GM Volume

High-resolution voxel-wise VBM mapping revealed prominent bilateral areas of increased GM

volume in the posterior hippocampus, plus additional foci of GM increase in the retrosplenial and medial prefrontal cortices in n-3 PUFA supplemented mice compared to controls ($p < 0.01$, cluster-based correction, **Figure 26**).

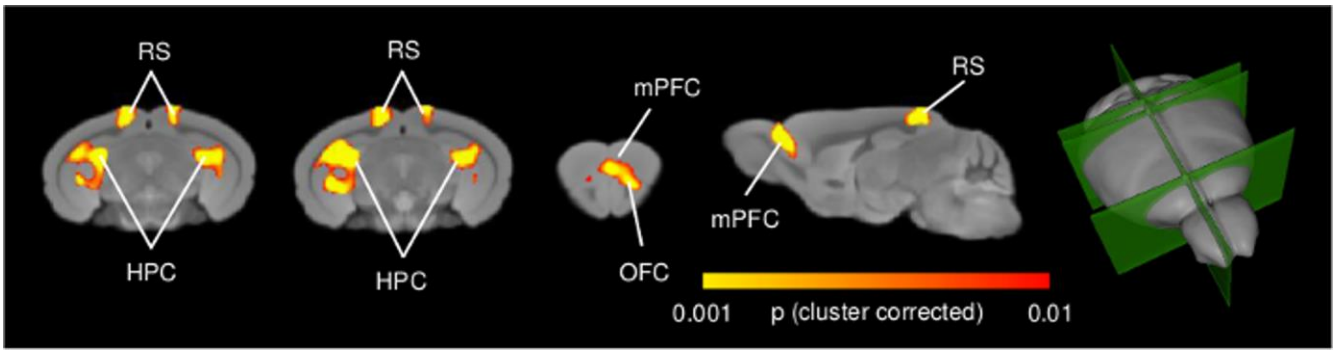

Figure 26. n-3 PUFA supplementation increases hippocampal and prefrontal GM volume. *VBM morphometric analysis revealed significantly increased ($p < 0.01$, cluster corrected at a significance level of 0.01) regional GM volume in hippocampal formation, prefrontal and retrosplenial cortex in n-3 PUFA supplemented compared to control mice. 3D rendering of the sagittal and coronal slices is also visualised. HPC = hippocampus; mPFC = medial prefrontal cortex; RS = retrosplenial cortex.*

No foci of significant GM volume reduction were observed throughout the brain in n-3 PUFA supplemented mice ($p < 0.01$, cluster-based correction).

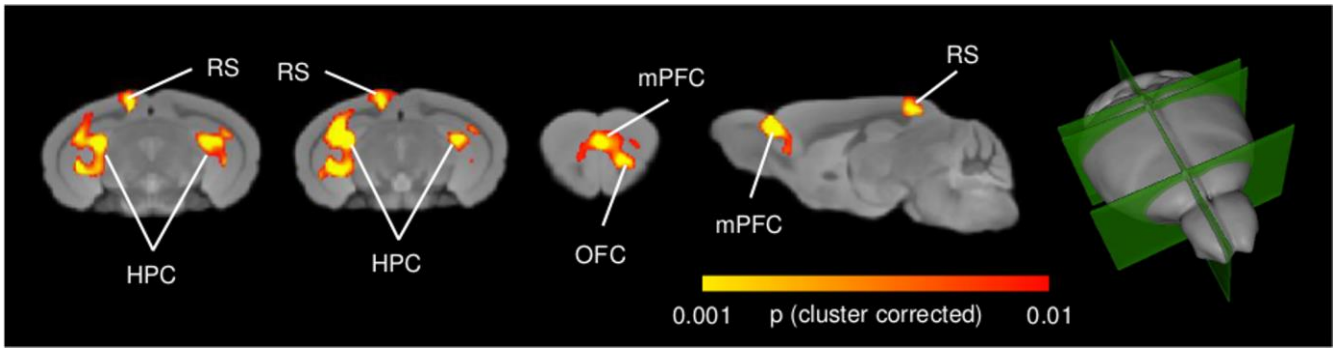

Figure 27. Tensor Based Morphometry (TBM) corroborates supplementation-specificity of increased GM volume mapped with VBM. *n-3 PUFA supplementation increases hippocampal and prefrontal GM volume as seen with TBM ($p < 0.01$, cluster-based correction at a significance level of 0.01). Note the overlap with VBM analysis. HPC = hippocampus; mPFC = medial prefrontal cortex; RS = retrosplenial cortex; OFC = orbitofrontal cortex.*

TBM of n-3 PUFA and control groups produced similar inter-group difference maps with clear involvement of foci of hippocampal, retrosplenial and prefrontal areas ($p < 0.01$, cluster-based correction **Figure 27**). The presence of analogous findings in VBM and TBM maps corroborates a supplementation-specific impact on the GM volumes mapped with VBM.

3.3.3. Behavioral Performances Correlate with Fronto-Hippocampal GM Volume

In an attempt to probe the relationship between cognitive and behavioral performance and regional GM volumes, and locate the brain substrates underlying the different performance levels of the two groups, voxel-wise regression of individual behavioral parameters was performed on GM maps at the subject level.

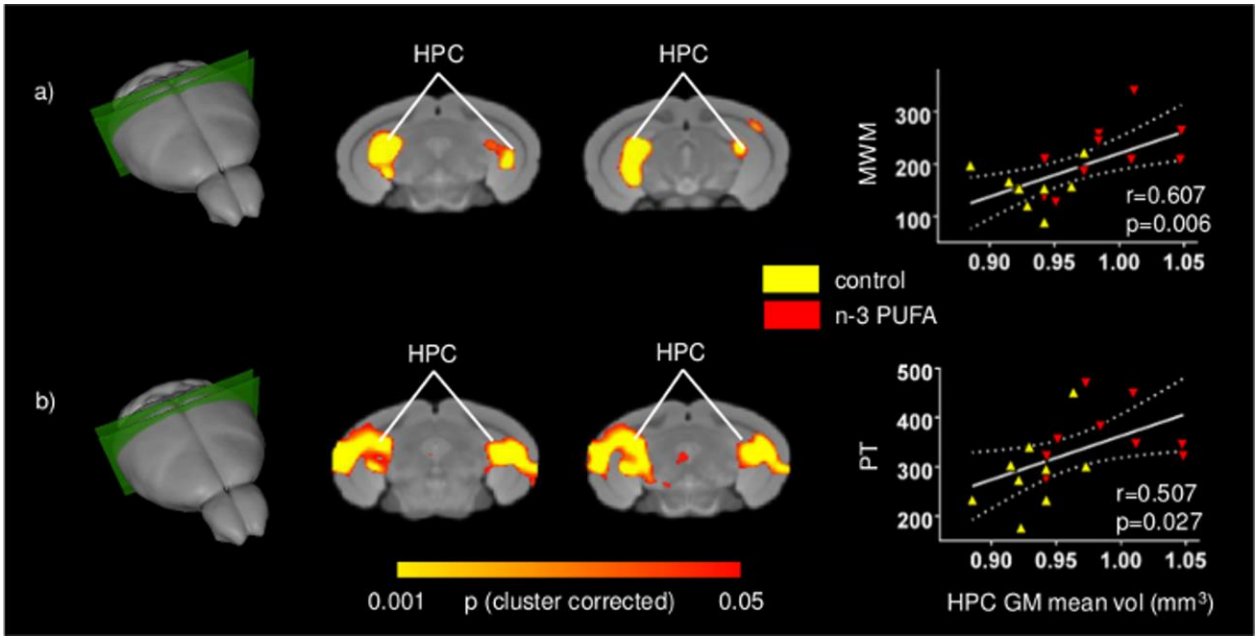

Figure 28. Behavioral performances are positively correlated with hippocampal GM increase. *Voxel-wise correlation mapping of behavioral scores and GM volume. Foci of correlation between GM volume and enhanced MWM spatial mnesic performances (a) and increased coping skills in the Porsolt test (b) were found in the same regions exhibiting univariate increased GM volume. Scatter plots indicate significant Pearson's correlations between n-3 PUFA concentrations and hippocampal mean GM volume (continuous lines), and the 95% CI (dotted lines). Red triangles indicate n-3 PUFA supplemented subjects, yellow triangles indicate the control group subjects. HPC = hippocampus; MWM = Morris Water Maze; PT = Porsolt test.*

Figure 28 depicts significant voxel-wise correlation mapping obtained by using individual behavioral scores as regressors. Consistent with univariate mapping of supplementation effects, foci of significant voxel-wise correlations were observed in hippocampal formation when behavioral scores from MWM and Porsolt test were used ($p < 0.05$, cluster-based correction).

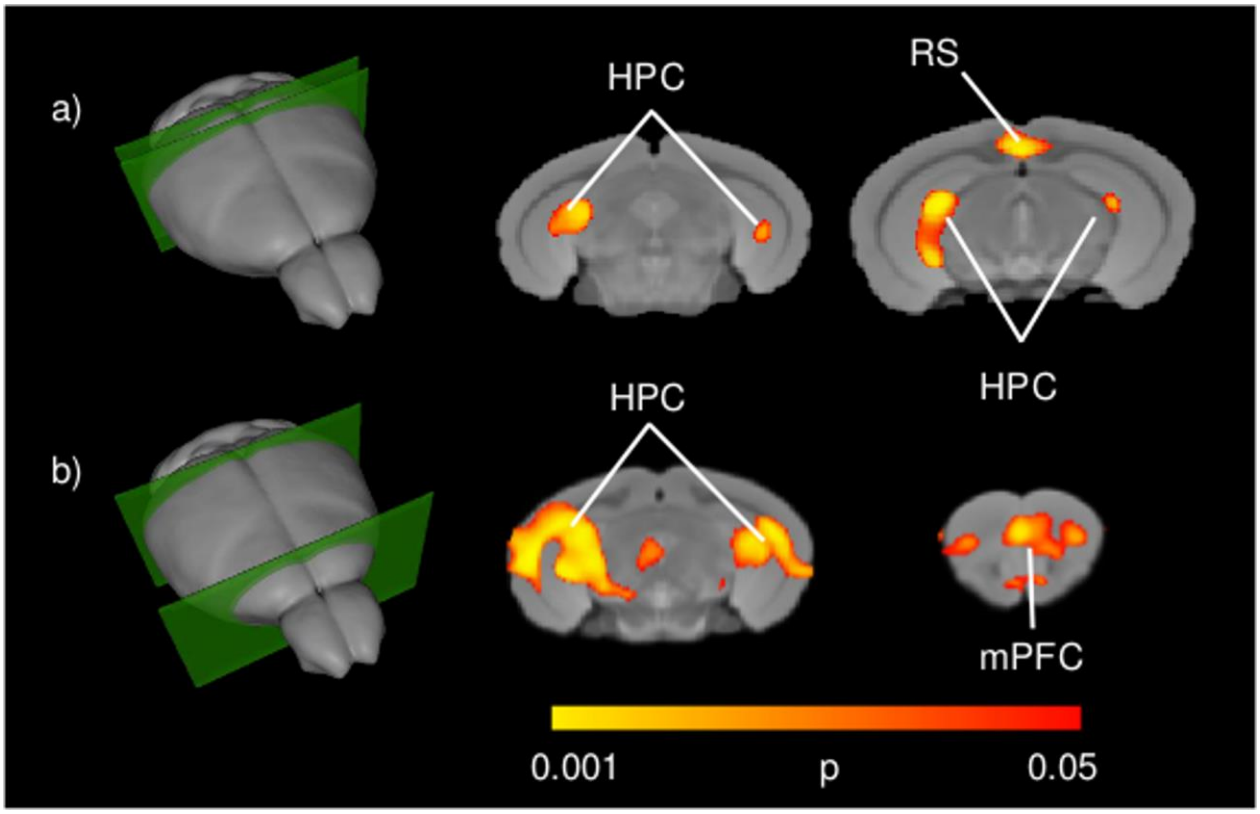

Figure 29. Behavioural performances are positively correlated with fronto-hippocampal GM volume. *Consistent with univariate inter-group mapping, voxel-wise correlation of behavioral scores and GM volume prior to cluster-based correction revealed foci of significant correlation in hippocampal and prefrontal regions. GM-behavioral performance correlation map for MWM spatial mnesic performances (a) and coping skills in the Porsolt test (b). The prefrontal effects did not survive cluster-based correction (p = 0.01, Fig. 5). HPC = hippocampus; mPFC = medial prefrontal cortex; RS = retrosplenial cortex.*

In good agreement with univariate inter-group maps, additional foci of significant correlation were found in retrosplenial and medial prefrontal cortices, an effect that however did not survive cluster-based correction (**Figure 29**). Overall, these findings support the involvement of the

mapped GM substrates in the improved cognitive and increased coping skills exhibited by n-3 PUFA supplemented mice. No significant correlations were found for any of the remaining behavioral variables mapped.

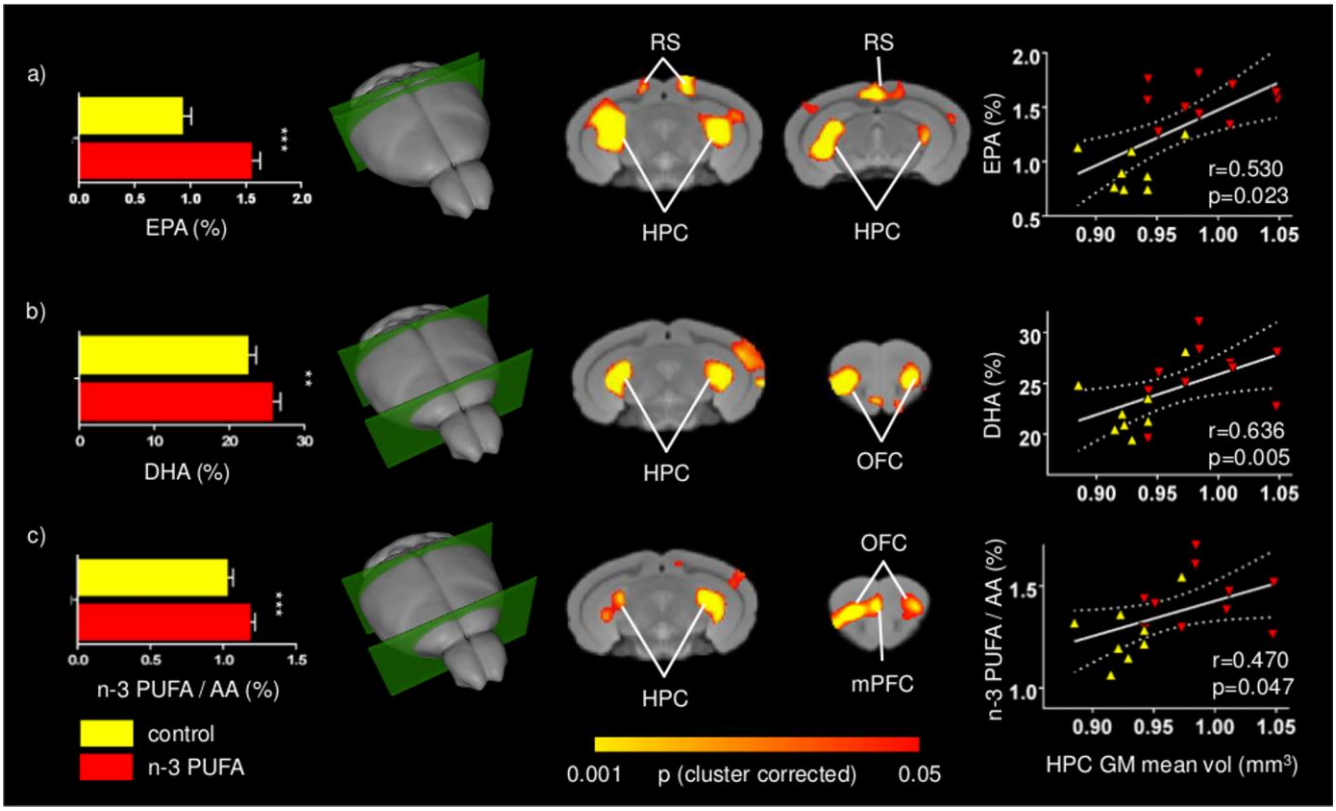

Figure 30. Positive correlations between n-3 PUFA levels and fronto-hippocampal GM volume. *Voxel-wise correlation mapping of total brain EPA (a), DHA (b) and n-3 PUFA/AA concentrations (c) and GM volume revealed foci of significant correlation in the same regions exhibiting univariate increased GM (hippocampal, prefrontal, retrosplenial, and orbitofrontal areas). Histograms report mean concentrations with error bars indicating SEM. Scatter plots indicate significant Pearson's correlations between n-3 PUFA concentrations and hippocampal mean GM volume (continuous lines), and the 95% CI (dotted lines). Red triangles indicate n-3 PUFA supplemented subjects, yellow triangles indicate the control group subjects. HPC = hippocampus; mPFC = medial prefrontal cortex; RS = retrosplenial cortex; OFC = orbitofrontal cortex; EPA = eicosapentaenoic acid; DHA = docosahexaenoic acid; AA = arachidonic acid. Asterisks inside the graphs indicate the significance levels of comparisons between groups: **p ≤ 0.01 , or ***p ≤ 0.001.*

3.3.4. n-3 PUFA Supplemented Mice Exhibit Increased EPA and DHA Brain Levels

To assess effectiveness of the supplementation regime, the concentrations of EPA, DHA, and DPA, the three major n-3 PUFA components of cell membranes, were measured. EPA+DHA+DPA/Arachidonic Acid (AA) ratio was also measured given its postulated role in cognitive dysfunction and neuroinflammation (Rao, Ertley et al. 2007, Labrousse, Nadjar et al. 2012).

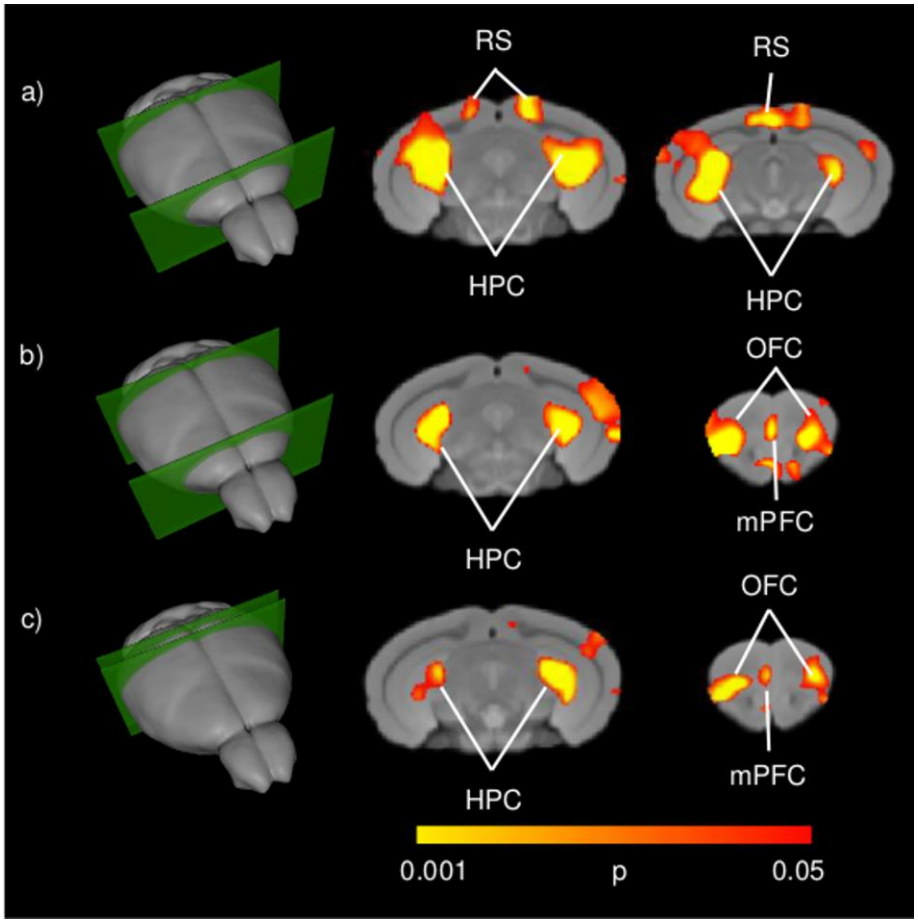

Figura 31. Positive correlations between n-3 PUFA levels and fronto-hippocampal GM volume. *Consistent with univariate inter-group mapping, voxel-wise correlation between total brain EPA (a), DHA (b) and n-3 PUFA/AA concentrations (c) and GM volume prior to cluster-based correction revealed foci of significant correlation in hippocampal and prefrontal regions. For EPA, prefrontal effects did not survive cluster-based correction (p = 0.01, Fig. 6). HPC = hippocampus; OFC = orbitofrontal cortex; mPFC = medial prefrontal cortex; RS = retrosplenial cortex; EPA = eicosapentaenoic acid; DHA = docosahexaenoic acid; AA = arachidonic acid.*

EPA and DHA, but not DPA, levels were found to be increased in the n-3 PUFA group in comparison to controls, as revealed by one-way ANOVAs (EPA: $F_{1,19} = 68.36$, $p < 0.000001$; DHA: $F_{1,19} = 7.11$, $p = 0.01$; DPA: $F_{1,19} = 0.10$, $p = 0.75$). Moreover, one-way ANOVA on the EPA+DHA+DPA /AA ratio revealed a significant increase of EPA+DHA+DPA/AA ratio in n-3 PUFA group in comparison to controls ($F_{1,19} = 7.55$, $p = 0.01$) (**Figure 30**).

3.3.5. Brain Levels of n-3 PUFA Positively Correlate with Fronto-Hippocampal GM Volume

To further probe the relationship between n-3 PUFA supplementation and GM morphometric alterations mapped, voxel-wise correlations of n-3 PUFA levels of individual subjects were generated. Voxel-wise correlation of total EPA, DHA and n-3 PUFA/AA concentrations revealed foci of significant correlations in the hippocampal, retrosplenial and prefrontal regions, as well as orbitofrontal areas ($p < 0.05$, cluster-based correction; **Figure 30**). Additional foci of significant voxel-wise correlations between GM volumes and DHA levels were found in the medial prefrontal cortex in uncorrected statistics maps (**Figura 31**). The anatomical location of these correlations is consistent with the effects of n-3 PUFA supplementation on GM volume and behavioral performance changes.

3.4. Discussion

As main components of synaptic membranes, n-3 PUFA have an important role in keeping structure and function of aged brain, a feature that has promoted research on their dietary supplementation as a strategy to counteract aging-related cognitive decline. However, despite encouraging epidemiological evidence linking enhanced peripheral n-3 PUFA levels to improved cognitive performance and brain structure (Denis, Potier et al. 2015), interventional studies on n-3 PUFA supplementation have so far produced inconsistent results. This issue

could reflect methodological inconsistencies such as the contribution of genetic and environmental factors that cannot be effectively controlled in human studies. In the present work we sought to overcome these limitations by investigating the relationships between GM volumes, cognitive and emotional performances, and n-3 PUFA cerebral levels in genetically homogeneous inbred aged mice reared in controlled laboratory conditions. In particular, we investigated whether long-term n-3 PUFA supplementation starting at old age may produce behavioral improvements and how the eventual improvements can be related to underlying neuroanatomical substrates. The present results strongly corroborate the emerging view of a pro-cognitive and neuroprotective function of n-3 PUFA supplementation on the aged brain (Varteresian and Lavretsky 2014). Specifically, n-3 PUFA supplemented mice exhibited improved mnesic functions and coping skills, and presented foci of greater GM volumes in fronto-hippocampal areas. The increased GM volumes correlated with better mnesic performances, increased active coping skills, and enhanced total brain n-3 PUFA concentrations. Collectively, these findings indicate that the n-3 PUFA-induced neuroprotective effects are able to take place even when the supplementation starts at late age. Importantly, the present results were obtained through commonly available supplements (i.e., commercially available n-3 PUFA mixture and olive oil) and employing a well-established brain structural VBM readout to maximize ecological validity and translational value.

The effects here reported develop our recent evidence of a beneficial cognitive effects of n-3 PUFA supplementation in aged mice (Cutuli, De Bartolo et al. 2014) and indicate that the n-3 PUFA-induced hippocampal changes observed at the cellular scale are associated to the macro-scale structural alterations detectable with MRI mapping. Furthermore, the here observed improvements in many facets of mnesic (localizatory, discriminative and social) function, convincingly support an overall n-3 PUFA pro-cognitive action in aging. n-3 PUFA

interventional studies in humans also sustain this view evidencing delayed cognitive decline in elderly people with (Yurko-Mauro, McCarthy et al. 2010) or without (Danthiir, Burns et al. 2011) subjective memory complaints, and in patients with mild cognitive impairment (Chiu, Su et al. 2008) or very mild AD (Freund-Levi, Eriksdotter-Jönhagen et al. 2006).

Importantly, in the present research n-3 PUFA supplementation exerted beneficial effects not only on cognitive, but also on emotional behaviors. Specifically, n-3 PUFA supplemented mice showed more active coping responses, without inter-group differences in anxiety levels. It is well-known that depression is a multifaceted disorder frequently associated with aging, metabolic disorders and neurodegenerative diseases (Lang and Borgwardt 2013), and that it is linked to prefrontal and hippocampal atrophy (Erickson, Miller et al. 2012, Vu and Aizenstein 2013). In agreement with the few previous experimental and clinical findings (Puri, Counsell et al. 2001, Schipper, Kiliaan et al. 2011, Samieri, Maillard et al. 2012, Lang and Borgwardt 2013), our results indicate that n-3 PUFA supplementation is able to improve coping abilities by preserving fronto-hippocampal functionality. As a further note, it is important to remember that the n-3 PUFA deficiency has been associated with the dysfunction of neuronal membrane stability and catecolaminergic neurotransmission linked to the aetiology of depressive symptoms (Su 2009). Recently, it has been proposed that EPA and DHA increase serotoninergic transmission by reducing prostaglandin levels and increasing neuronal membrane fluidity (Patrick and Ames 2015). Given that in the Porsolt test selective serotonin and norepinephrine reuptake inhibitors are reported to increase swimming and climbing behaviors respectively (Renault and Aubert 2006), we cannot exclude that the n-3 PUFA beneficial effects may be ascribed also to an influence of these nutrients on serotoninergic and noradrenergic neurotransmission.

The use of a three-dimensional hypothesis-independent GM mapping approach allowed us to

identify following n-3 PUFA supplementation extra-hippocampal foci of increased GM volume, such as retrosplenial and prefrontal areas. Analogous findings have been recently reported in an interventional study in aged humans receiving prolonged n-3 PUFA supplementation describing improved cognitive functions and increased GM volumes in the hippocampus, precuneus (area reciprocally connected with the adjacent retrosplenial cortex) and frontal areas (Witte et al., 2014). Although the exact mechanisms underlying the involvement of cortical regions remain to be determined, it can be advanced that in n-3 PUFA supplemented mice the preservation of prefrontal structural integrity is functionally driven by the direct afferents stemming from CA1 and subicular hippocampal regions (Hoover and Vertes 2007). This hypothesis is consistent with enhanced neuroplasticity phenomena (such as increased neurite outgrowth, synaptogenesis, angiogenesis), and decreased neurodegenerative processes (such as apoptosis, astrocytosis) observed in the hippocampus of n-3 PUFA supplemented animals (Gómez-Pinilla 2008, Thomas and Baker 2013, Cutuli, De Bartolo et al. 2014, Dyall 2015). Speculatively, it can be hypothesized that the same neuroplastic processes may act at prefrontal and retrosplenial level promoting structural preservation.

Finally, the contribution of WM changes should also be taken into account. Indeed, recent correlational studies reported positive associations between n-3 PUFA levels and GM or WM volumes (Samieri, Maillard et al. 2012, Tan, Harris et al. 2012, Titova, Sjögren et al. 2013, Virtanen, Siscovick et al. 2013, Pottala, Yaffe et al. 2014, Raji, Erickson et al. 2014). Recently, Witte et al. (2014) suggested that the superior WM microstructural architecture of n-3 PUFA supplemented older adults could be linked to higher myelination, increased fiber packing density and reduced axonal damage that sustain better cognitive performances by improving axonal transmission.

The presence of positive regional association between n-3 PUFA brain levels and GM volumes

might be linked to increased regional volume resulting from n-3 PUFA induced increased membrane fluidity and reduced neuroinflammation processes. Specifically, research on the aging brain has shown that major biochemical changes affect the neuronal membrane that is the site of action for many essential functions, such as neurotransmission, regulation of membrane-bound enzymes, control of the ionic channels structure and activity, and receptors maintenance (Yehuda 2012). During aging, the level of cholesterol and its toxic metabolites greatly increases in neuronal membranes, thus reducing the membrane fluidity. On the other hand, n-3 PUFA concentration in aged neuronal membranes decreases(Yehuda, Rabinovitz et al. 2002). Interestingly, in the present study EPA and DHA levels, and n-3 PUFA/AA ratio increased following n-3 PUFA supplementation. Thus, it can be argued that by increasing membrane fluidity, n-3 PUFA supplementation may prevent and/or counteract brain aging.

In addition, EPA and DHA have an anti-inflammatory role by giving rise to mediators, such as resolvins and neuroprotectin D1 (Bazan, Musto et al. 2011, Calder 2011), and decreasing age-related microglial activation, oxidative stress, and increased pro-inflammatory cytokines (Martin, Lonergan et al. 2002, Maher, Martin et al. 2004, Lynch, Loane et al. 2007, Kelly, Grehan et al. 2011, Trépanier, Hopperton et al. 2015). Accordingly, the present increased n-3 PUFA brain concentrations may result in anti-inflammatory effects, thus contributing to neuroprotective actions against brain atrophy and cognitive decline. Among the multifactorial processes underlying n-3 PUFA beneficial effects on brain structural parameters, cognition, and affective regulation, also the increased monoaminergic and cholinergic neurotransmission should be taken into account (Willis, Shukitt-Hale et al. 2009, Jiang, Liang et al. 2012). In any case, future research on this topic is warranted to pinpoint the cellular and sub-cellular determinants of n-3 PUFA induced volumetric enhancement at cortical level.

Collectively, the present findings suggest that n-3 PUFA supplementation in old age helps

maintaining brain functionality by counteracting reductions in GM volume in prefrontal and retrosplenial cortices, as well as in hippocampus. In this respect, n-3 PUFA appear ideal candidates for cognition-enhancing and antidepressant nutritional interventions aimed to promote active and healthy aging. This issue is of growing relevance, given the pressing need to maintain cognitive functions in the elderly Western population, whose life expectancy increasingly rises. Moreover, our study supports the use of VBM measurements in human population as a surrogate mechanistic marker for n-3 PUFA pro-cognitive action in controlled supplementation trials assessing their therapeutic use in the healthy and diseased aged brain.

4. Gray Matter scMRI Networks in the Mouse Brain

All the material presented in this chapter has been recently published in the article “All the material presented in this chapter has been recently published in the article “**Pagani M**, Bifone A, Gozzi A (2016). Structural covariance networks in the mouse brain, *NeuroImage*, 129:55-63.”

The presence of networks of correlation between regional gray matter volume as measured across-subjects in a group of individuals has been consistently described in several human studies, an approach termed structural covariance MRI (scMRI). Complementary to prevalent brain mapping modalities like functional and diffusion-weighted imaging, the approach can provide precious insights into the mutual influence of trophic and plastic processes in health and pathological states. To investigate whether analogous scMRI networks are present in lower mammal species amenable to genetic and experimental manipulation such as the laboratory mouse, we employed high resolution morphoanatomical MRI in a large cohort of genetically-homogeneous wild-type mice (C57Bl6/J) and mapped scMRI networks using a seed-based approach. We show that the mouse brain exhibits robust homotopic scMRI networks in both primary and associative cortices, a finding corroborated by independent component analyses of cortical volumes. Subcortical structures also showed highly symmetric inter-hemispheric correlations, with evidence of distributed antero-posterior networks in diencephalic regions of the thalamus and hypothalamus. Hierarchical cluster analysis revealed six identifiable clusters of cortical and sub-cortical regions corresponding to previously described neuroanatomical systems. Our work documents the presence of homotopic cortical and subcortical scMRI networks in the mouse brain, thus supporting the use of this species to investigate the elusive biological and neuroanatomical underpinnings of scMRI network development and its derangement in neuropathological states. The identification of scMRI networks in genetically

homogeneous inbred mice is consistent with the emerging view of a key role of environmental factors in shaping these correlational networks.

4.1. Background

Correlation analyses of magnetic resonance imaging (MRI) data have produced evidence of integrated structural and functional networks of brain regions, thus providing information on brain organization beyond the segregated local properties classically revealed by univariate methods (Bullmore and Sporns 2009). Complementary to networks mapped with resting state functional MRI and white matter pathways reconstructed with diffusion weighted imaging, large scale scMRI networks represent an additional valuable source of information about inter-regional connectivity (Alexander-Bloch, Raznahan et al. 2013). Specifically, this approach permits to study the extent to which inter-individual differences in regional structures are coherently organized within networks of gray matter volumes or cortical thickness that emerge across a population of individuals (Alexander-Bloch, Giedd et al. 2013, Evans 2013).

Sc-MRI has provided valuable insight into the structural organization of the brain. Recent scMRI studies have substantially expanded and corroborated early post-mortem evidence of anatomical covariance between regions of the visual and motor systems (Andrews, Halpern et al. 1997, White, Andrews et al. 1997) by highlighting robust correlations between inter-hemispheric homotopic regional gray matter volume in motor, somatosensory and associative cortical regions of the human brain (Mechelli, Friston et al. 2005, Zielinski, Gennatas et al. 2010). Similarly, limbic cortical and non-cortical regions have been shown be part of more distributed covariance network that encompass wide portion of prefrontal and temporal regions (Bernhardt, Klimecki et al. 2013).

Anatomical covariance mapping has also offered initial insights into the abnormal structural organization of networks in brain disorders. For example, reduced extension of the right anterior insular network has been reported in patient diagnosed with autism spectrum disorder (Zielinski, Anderson et al. 2012). Analogously, basal ganglia, parietal and fronto-temporal scMRI networks exhibit reduced gray mater content in schizophrenic patients compared to healthy controls (Xu, Groth et al. 2009), and decreased inter-hemispheric correlations between postcentral gyrus and parietal lobule have been observed in patients diagnosed with Alzheimer's disease (He, Chen et al. 2008).

Despite the increasing interest in scMRI and its emerging use to investigate the trophic development of gray matter, fundamental questions regarding the origin and significance of these correlative networks remain unanswered. For example, recent evidence has linked genetic polymorphisms with the development of specific functional and anatomical networks (Pezawas, Meyer-Lindenberg et al. 2005), however, the genetic determinants underlying the emergence of these networks remain poorly understood. Moreover, although correlations between cortical gray matter thickness and structural connectivity have been described (Lerch, Worsley et al. 2006), with recent estimates suggesting that white matter MRI connectivity explains approximately 35‑40% of the thickness correlations across the cerebral cortex (Gong, He et al. 2012), whether anatomical covariance requires intact axonal connectivity, or can develop in the face of altered connectional substrates like in the case of congenital callosal alterations or white matter abnormalities (Tyszka, Kennedy et al. 2011, Sforazzini, Bertero et al. 2014), remains to be determined. Finally, although both genetic and environmental factors have been identified to play a role in shaping these networks (Schmitt, Lenroot et al. 2008, Schmitt, Lenroot et al. 2009, Rimol, Panizzon et al. 2010), the relative contribution of these

components is poorly understood and it is not clear to what extent covariance is a causal result of genetic influence, development and aging, or experience-related plasticity (Evans 2013).

The investigation of networks of anatomical covariance in laboratory mice - where a wide repertoire of genetic, molecular and cellular manipulations can be readily implemented - could complement human research on the emergence of gray matter covariance networks, and generate novel hypothesis about the etiopathological origin of aberrant scMRI findings in human brain diseases (Alexander-Bloch, Giedd et al. 2013). In the present work, we used high resolution structural imaging and voxel-based morphometry (Dodero, Damiano et al. 2013, Sannino, Gozzi et al. 2014) to probe the presence of cortical and subcortical networks of anatomical covariance in the mouse brain. To this end, scMRI mapping was carried out in a large cohort (N=53) of genetically-homogeneous inbred C57Bl6/J mice, thus permitting to assess the emergence of these networks under controlled genetic and environmental conditions, an essential prerequisite for the implementation of scMRI approaches in transgenic models. Our result demonstrate the presence of robust homotopic scMRI gray matter networks in cortical and sub-cortical regions of the mouse brain, paving the way to the application of interventional approaches to study the physiological and pathological effectors of this phenomenon.

4.2. Materials and Methods

4.2.1. Ethical Statement

All research involving animals were carried out in accordance with the European directive 86/609/EEC governing animal welfare and protection, which is acknowledged by the Italian Legislative Decree 116 - 27 January 1992, and following the recommendations in the Guide for the Care and Use of Laboratory Animals of the National Institutes of Health. Animal research

protocols were also reviewed and consented by the Animal Care Committee of the Istituto Italiano di Tecnologia (Permit date 07-2012).

4.2.2. Sample Preparation and Image Data Acquisition

High-resolution morphoanatomical T2-weighted MR imaging of C57Bl6/J male mouse brains (n=53) was performed in paraformaldehyde (4% PFA; 100 ml) fixed specimens, a procedure employed to obtain high-resolution images with negligible confounding contributions from physiological or motion artefacts (Cahill, Laliberte et al. 2012). Standard sample preparation and MRI acquisition has been recently described (Dodero, Damiano et al. 2013, Sforazzini, Bertero et al. 2014) and is reported below to provide a comprehensive description of all the experimental procedures involved. Briefly, male B6 mice were deeply anaesthetized with an intraperitoneal Avertin injection (375 mg/Kg) and their brains were perfused in situ via cardiac perfusion. The perfusion was performed with phosphate buffered saline followed by paraformaldehyde (4% PFA; 100 ml). Both perfusion solutions were added with a Gadolinium chelate (Prohance, Bracco, Milan) at a concentration of 10 and 5 mM, respectively, to shorten longitudinal relaxation times. A four-channel 7.0 Tesla MRI scanner (Bruker Biospin, Milan) was used to acquire anatomical images of the brain, using a 72 mm birdcage transmit coil, a custom-built saddle-shaped solenoid coil for signal reception, and the following imaging parameters: FLASH 3D sequence with TR=17ms, TE=10ms, α=30°, matrix size of 260x160x180, field of view of 1.83x1.26x1.26 cm, voxel size of of 90 µm3 (isotropic).

4.2.3. Image Data Preprocessing and VBM

VBM of gray matter was performed using ANTs (Avants, Yushkevich et al. 2010), a flexible open source toolkit widely adopted for mice and human studies. Nonlinear registration-based VBM procedure on the mouse brain has been thoroughly described in a previous

methodological study and it is only briefly reported herein (Pagani et al. under review). Each high-resolution T2W image was corrected for intensity non-uniformity and skull stripped to remove extra brain tissue. A study based template was created by aligning pre-processed images to a common reference space using affine and diffeomorphic registrations. After registering individual images to the study based template, spatially normalized images were segmented to calculate tissue probability maps. The separation of the different tissues is improved by initializing the process with the probability maps of the study based template previously segmented. The Jacobian determinants of the deformation field were extracted and applied to modulate the grey matter probability maps calculated during the segmentation. This procedure permits the analysis of grey matter probability maps in terms of local volumetric variation instead of tissue density. Jacobian determinants were also normalized by the total intracranial volume (range 390 - 531 mm3) to account for inter-subject variability in total brain volume (Bassett, Bullmore et al. 2008, Zielinski, Anderson et al. 2012). The resulting modulated grey matter probability maps were then smoothed using a Gaussian kernel with a sigma of three voxel width.

4.2.4. Grey Matter Variance Map

Ninety-nine neuroanatomical (68 cortical and 31 extracortical) volumes from previously published parcellated reference neuroanatomical atlases of the mouse brain (Dorr, Lerch et al. 2008, Ullmann, Watson et al. 2013) were registered to each image. This procedure standardizes the location and size of each brain region, thus avoiding operator-dependent bias related to manual anatomical recognition and improves replicability of findings. We used this method also to identify VOIs for agglomerative hierarchical clustering and for seed-based correlation mapping (described below). The variance of grey matter volumes in each

neuroanatomical volume was then calculated across subjects, yielding a region-by-region map of the gray matter variability of our inbred mice.

4.2.5. Agglomerative Hierarchical Clustering

Agglomerative hierarchical clustering is a bottom-up data driven approach that aims to find clusters based on a similarity measure and has the advantage of requiring no a priory information on the number of cluster to be computed. We used the R package ‘gplots’ (http://cran.r-project.org/web/packages/gplots/index.html) to calculate the correlation matrix of the mean grey matter volumes of major neuroanatomical volumes of interest (VOIs) and to perform the agglomerative hierarchical cluster analysis adopting Euclidean distance as similarity measure (Schmitt, Lenroot et al. 2008). Color coding to highlight the diverging nature of the correlation matrix was obtained using the R package ‘RColorBrewer’ (http://cran.r-project.org/web/packages/RColorBrewer/index.html). A dendrogram was also displayed both to visualize the degree of similarity between the VOIs - where similar vectors of correlation are visualized more proximal - and to identify the most informative higher level clusters of the correlation matrix. Hierarchical clustering provides an overview of the connectivity patterns of gray matter over the whole brain. The approach however suffers from a limited spatial resolution, determined by the size of the VOIs employed. To overcome this limitation, a subsequent seed based analysis was performed to calculate whole brain voxelwise correlations on the gray matter volumetric maps between 14 seeds and the rest of the brain voxelwise.

4.2.6. Seed Region Analysis

Preprocessed images were employed for a seed-based correlation analysis to examine voxelwise gray-matter covariance patterns with respect to neuroanatomical VOIs of interest. To this purpose, unilateral right or left cortical and subcortical anatomical VOI were used as

correlation seeds. All the VOIs were selected from cortical and sub-cortical VOIs from parcellated reference atlases previously registered to each image (Dorr, Lerch et al. 2008, Ullmann, Watson et al. 2013). The anatomical volumes probed are: primary auditory, motor, somatosensory, visual, cingulate, retrosplenial, insular and medial prefrontal cortex, amygdala, striatum, dorsal and ventral hippocampus, hypothalamus and thalamus. To map anatomical networks at a high spatial resolution, the mean grey matter volume of each seed was used as a regressor for each voxel in the brain to generate a voxel-wise correlation map. This permits to identify positive networks when an increase of gray matter in the seed is associated to an increase of gray matter in the voxels, and, similarly, negative networks when an increase in gray matter of the seed is associated to a decrease of gray matter in the voxels. Correlations were performed using FSL randomise non parametric permutation testing and statistical results where threshold at $p<0.05$ upon familywise error (FWE) correction for multiple comparisons (Mechelli, Friston et al. 2005).

4.2.7. Source Based Morphometry with Independent Component Analysis

After preprocessing, individual cortical images were concatenated in a single 4D gray matter image that was analyzed by means of source based morphometry (SBM), using the MATLAB GIFT toolbox (http://icatb.sourceforge.net). SBM exploits Independent Component Analysis (ICA) to map cortical scMRI networks at the voxel level by identifying maximally independent sources (Xu, Groth et al. 2009). We converted each gray matter image into a one-dimensional vector and we arrayed those vectors into a 53 row (subjects) by 163.401 column (voxels) matrix. This matrix was then decomposed into a mixing and a source matrix - where the mixing matrix expresses the relationship between subjects and components, and the source matrix expresses the relationship between the components and the voxels - using the Infomax approach (Bell and Sejnowski 1995). The number of independent components used for the

analysis (N = 15) was estimated after pilot studies performed with varying component numbers (3, 5, 10, 15, 20).

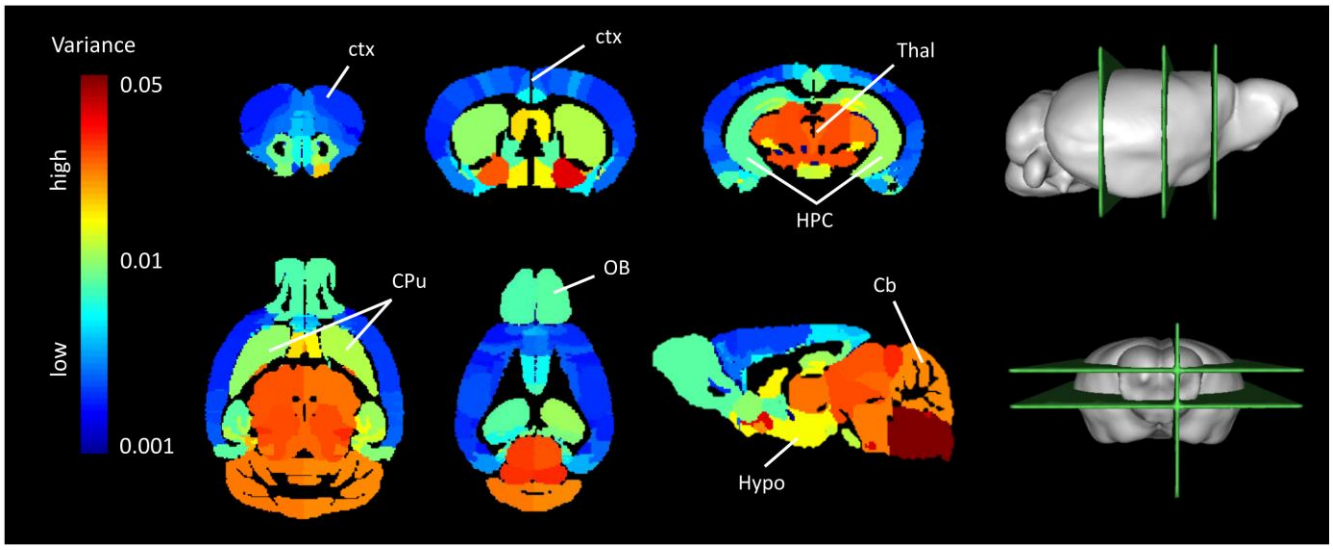

Figure 32 Inter-subjects gray matter volume variance. *The diencephalon, cerebellum and midbrain showed higher grey matter variance whereas the cerebral cortex displayed the lowest volumetric variability across subjects. Intermediate variance was found in the hippocampal formation, in the striatum, in the basal ganglia and in the olfactory bulbs. Coronal (top), horizontal (bottom, left) and sagittal (bottom, right) slices are displayed with relative 3D renderings to show the exact location of the cuts. Cb: cerebellum; CPu: caudate putamen; ctx: cortex; Hypo: hypothalamus; HPC: hippocampus; OB: olfactory bulbs; Thal: thalamus.*

We used ICASSO to test the statistical reliability of the independent component decomposition, by running Infomax 100 times with different initial conditions and bootstrapped data sets. All the other default parameters of GIFT (included PCA data reduction) were left unaltered. These source maps were then scaled to unit standard deviation (Z map) and thresholded at a value of |Z|> 2.0. Visual inspection of the estimated independent components allowed to separate meaningful components to those clearly related to noise.

4.3. Results

4.3.1 Regional Distribution of GM Variance

We first mapped the variance in regional gray matter volumes to identify regions characterized by higher inter subject variability, and, as such, more prone to be the substrates of trophic remodeling. The results of this univariate analysis revealed the presence of region specific differences in mean gray matter volumetric variability throughout the brain that could be empirically grouped into three variability profiles (**Figure 32**). The diencephalons, cerebellum and midbrain regions exhibited the highest gray matter variance. Regions with intermediate gray matter volume variability included the hippocampal formation, retrosplenial cortex, the basal ganglia and the olfactory bulbs. The cortical mantle showed overall low gray matter volume variance. Within the cerebral cortex, somatosensory and motor areas exhibited the lowest variance, while associative and limbic regions such as the prelimbic, infralimbic and cingulate cortices, showed relatively higher variability. Importantly, variance mapping highlighted exquisite symmetrical correspondence in virtually all the volumes probed, suggesting the presence of inter-hemispheric homotopic concordance in the inter-subject variability of regional gray matter volume. We also report voxelwise average gray matter volume map for all the subjects imaged (**Figure 33**).

As expected, all mouse gray matter regions (e.g. cortex) exhibit maximal voxelwise gray matter volume density. We also computed voxelwise covariance strength, i.e. the average correlation coefficient when the gray matter volume of every voxel is correlated with the gray matter volume of every other voxel. In this map, virtually all rostral brain regions plus the whole cortex display positive covariance strength, while negative covariance strength is apparent in subcortical gray matter regions, cerebellum and brain stem, as well as the amygdala, suggesting a

competitive/inhibiting effect on the growth of GM between rostral and caudal macroscale brain districts.

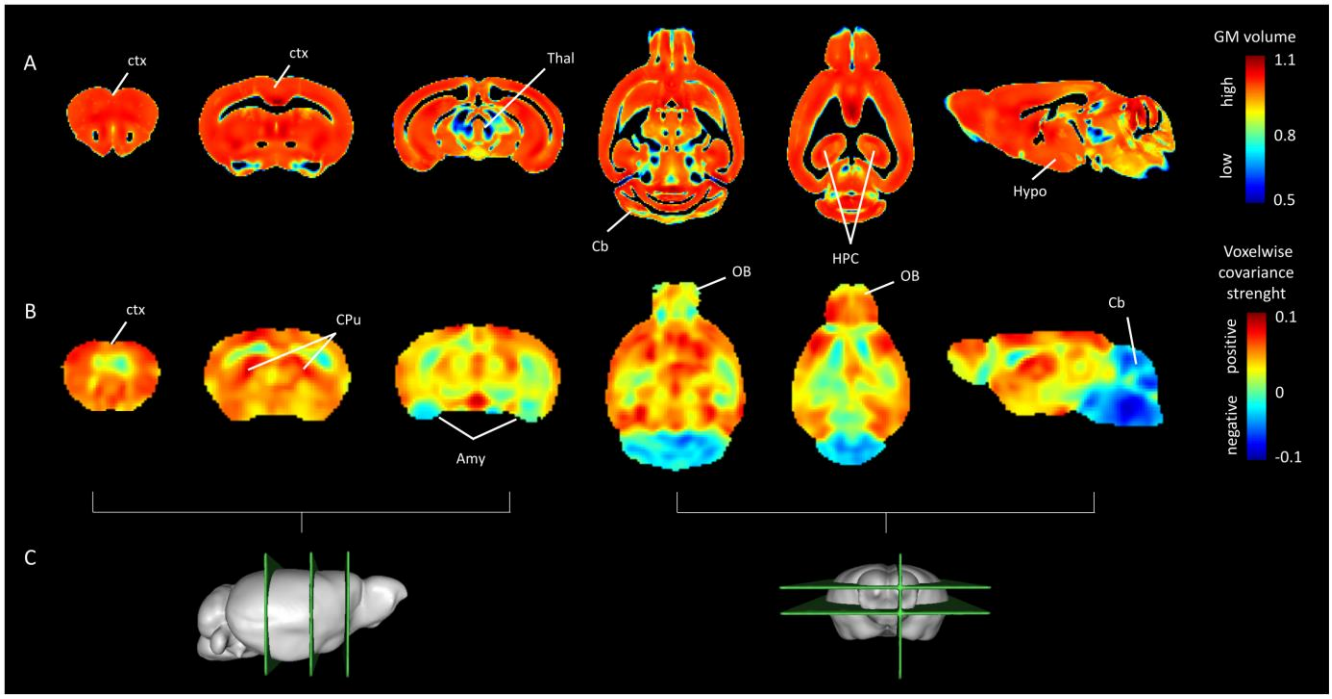

Figure 33. Inter-subjects gray matter volume and voxelwise covariance strength. *A) Maps of across subjects mean gray matter volume. All gray matter areas, including cerebral cortex and major subcortical nuclei showed consistently high gray matter volume. B) Maps of voxelwise covariance strength of gray matter volumes. Anterior areas of the brain and the cerebral cortex displayed a consistent pattern of positive covariance strength, whereas negative covariance strength was found in the posterior regions of the brain, including cerebellum, brain stem and amygdala. C) 3D renderings. Coronal, horizontal and sagittal slices are displayed with relative 3D renderings to show the exact location of the cuts. Amy: amygdala; Cb: cerebellum; CPu: caudate putamen; ctx: cortex; Hypo: hypothalamus; HPC: hippocampus; OB: olfactory bulbs; Thal: thalamus.*

4.3.2 Hierarchical Clustering and Source Based Morphometry

We next carried out an unbiased hierarchical clustering of inter-subject unilateral regional gray matter volumes to assess whether co-varying unilateral anatomical volumes would exhibit homotopic interhemispheric variance and would identify neuro-anatomically plausible systems. A color map of the correlation matrix obtained with a set of all the 198 VOIs covering the whole

brain gray matter volume is shown in **Figure 34** (for the detailed list of the VOIs to appendix A), highlighting two important features.

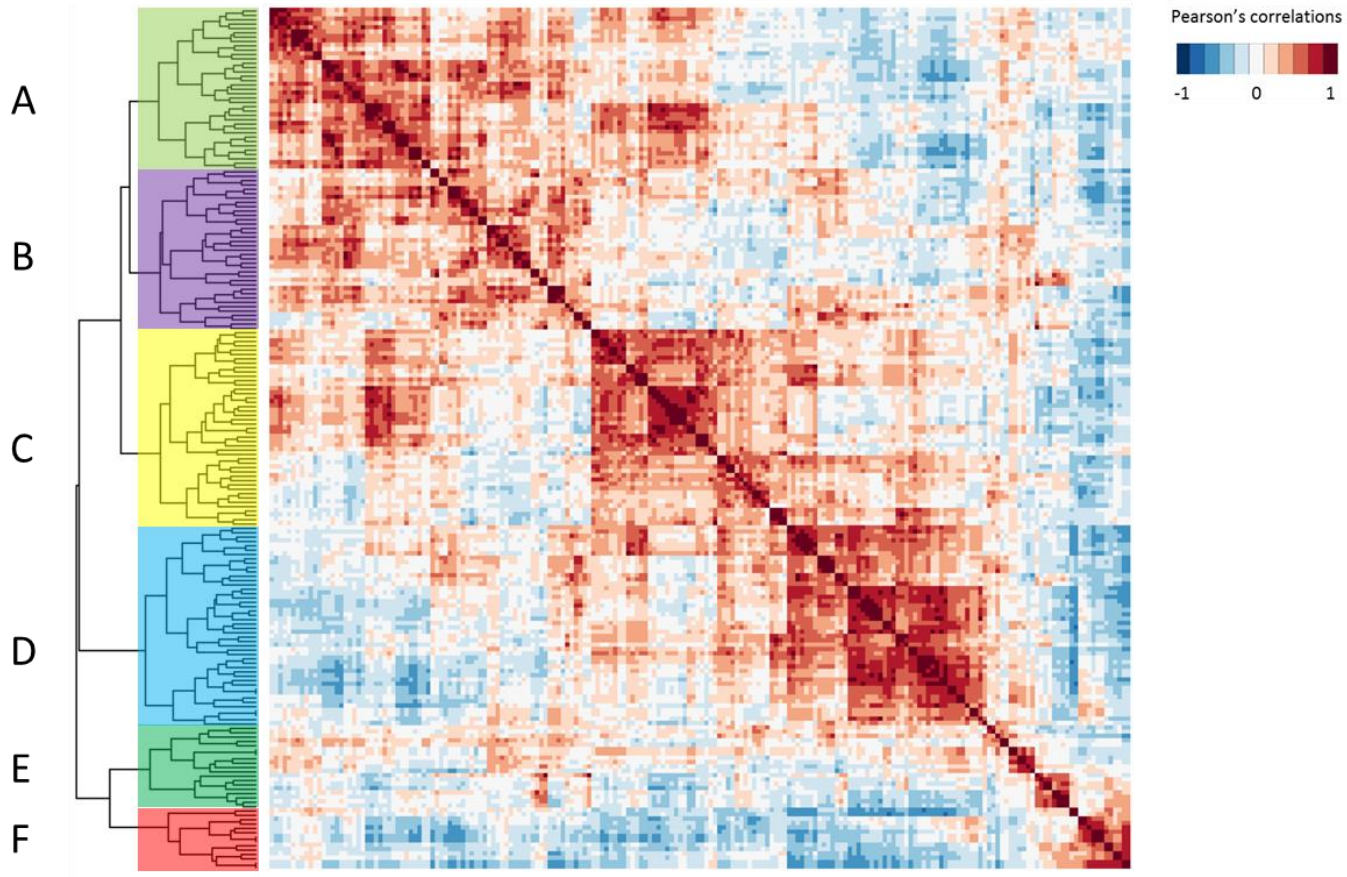

Figure 34 Whole brain agglomerative hierarchal clustering of regional gray matter volume. *Heatmap of the correlation between inter-subject gray matter volumes in all the 198 VOIs extracted from the two labelled neuroanatomical atlases. Regions have been arranged based on the results of agglomerative hierarchal cluster analysis. Six major clusters of structures were identified: A) a posterior cortical cluster, B) a hippocampal cluster, C) an anterior cortical cluster, D) a subcortical cluster, E) colliculi plus olfactory regions; and F) a brain stem and cerebellar cluster. The vast majority of homotopic areas clustered within the first steps of the agglomeration procedure. The ordered list of regions composing each cluster is reported in Appendix A.*

First, the vast majority of all left and right homotopic gray matter volumes displayed similar patterns of correlations and were found to be clustered together after the first steps of the agglomeration procedure. This finding demonstrates the presence of covarying gray matter

volumes in homotopic mouse brain regions, a finding recapitulating the structural organization of the human brain cortex (Mechelli, Friston et al. 2005). Additional agglomeration steps revealed six major clusters of anatomical structures reflecting different combinations of known mouse brain neuroanatomical systems. Specifically, the clusters identified were: A) a posterior cortical cluster, including auditory, visual and retrosplenial cortices; B) a hippocampal cluster, including hippocampal formation, rhinal and temporal association cortices, C) an anterior cortical cluster including both limbic (cingulate, orbitofrontal, insular cortex and prelimbic cortex) and somatomotor cortices; D) a subcortical cluster, including the striatum, amygdala, thalamus and hypothalamus, as well as the infralimbic cortex; E) colliculi and olfactory regions; and F) brain stem and cerebellar areas. All the clusters identified were characterized by the presence of positive correlations between their constituting regions. Interestingly, brain stem and cerebellar regions appeared to be anti-correlated to most of the neocortical and subcortical regions, suggesting a competing interaction in regional volumetric variability between these areas, which is consistent with voxelwise correlation strength mapping in **Figure 33**. A similar anti-correlation was also apparent between hippocampal and posterior neocortical cortex.

4.3.3 Seed Based Mapping: Sc-MRI Networks

To corroborate our results and overcome the issues related to the coarse spatial sampling achievable with volumetric cluster analysis, we carried out whole-brain voxelwise correlation analyses using mean gray matter volume from unilateral anatomical VOIs as seeds. Consistent with human studies (Mechelli, Friston et al. 2005, Zielinski, Gennatas et al. 2010), our results revealed strong positive associations between each of the seeds and their contralateral homotopic regions for all primary cortical areas probed (i.e. primary motor, somatosensory and auditory cortices **Figure 35**). Additionally, both right and left auditory networks were found to

encompass also the visual cortex bilaterally, and somatosensory and motor networks included foci of correlation in the cingulate cortex.

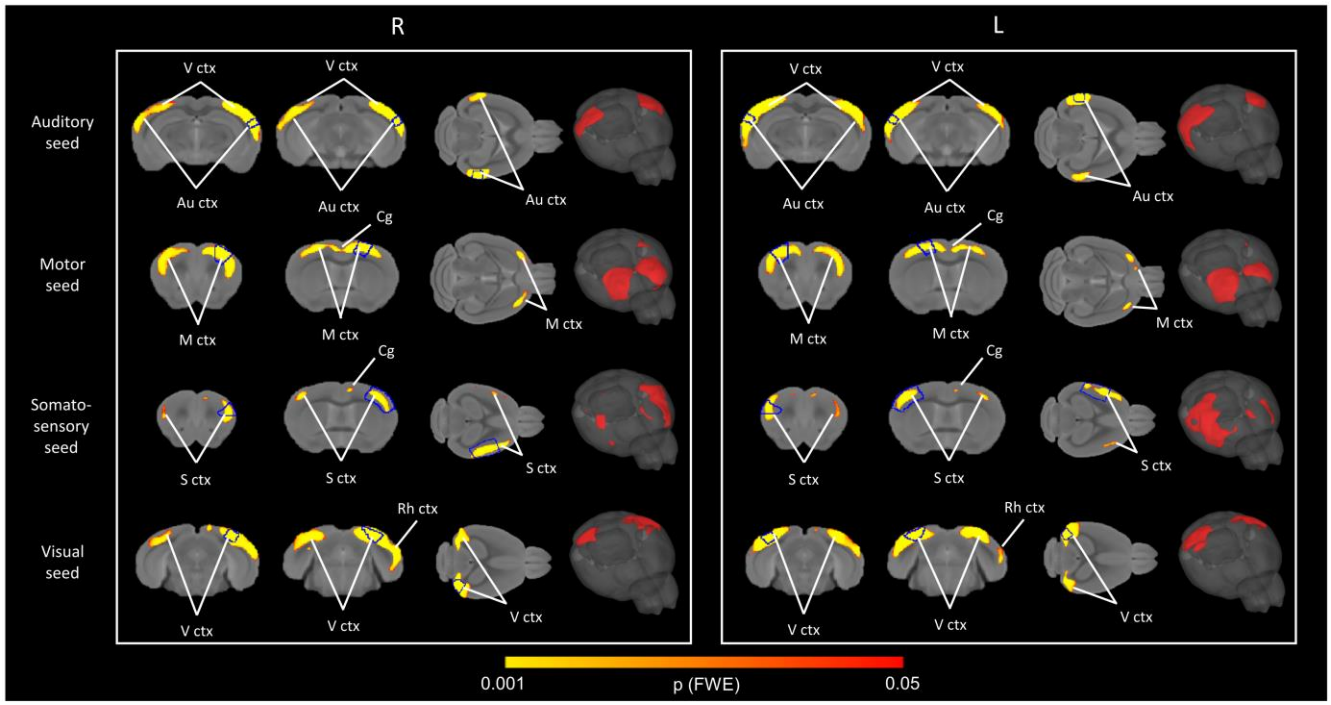

Figure 35. Networks of anatomical covariance: primary cortices. *Correlation maps for unilateral primary motor, somatosensory and auditory gray matter volume seeds. All the seeds exhibited the involvement of homotopic regions in the contralateral hemisphere. Additionally, both right and left auditory networks were found to encompass also the visual cortex bilaterally, and somatosensory and motor networks included foci of correlation in the cingulate cortex. Threshold of statistical significance was set at p<0.05, FWE corrected for multiple comparisons. Au ctx: auditory cortex; Cg ctx: cingulate ctx; M ctx: motor ctx; Rh ctx: rhinal cortex; S ctx: somatosensory cortex; V ctx: visual cortex.*

The use of unilateral seeds in associative cortical regions (i.e. cingulate, prefrontal, insular and retrosplenial cortices, **Figure 36**) highlighted analogous bilateral homotopic covariance patterns, together with the involvement of neighboring somatosensory regions. Consistent with the results of cluster analysis, the cingulate network also included large portions of the motor and somatosensory cortices corroborating the existence of a strong mutual trophic influence between these regions. We also found ipsilateral correlation between the insula and neighboring somatosensory and piriform cortices, and between the retrosplenium and the visual

cortex. Interestingly, covariance mapping using medial prefrontal seeds (left and right prelimbic cortex, **Figure 36**) revealed local network encompassing the orbitofrontal cortex bilaterally together with foci in the insular cortex, reminiscent of a pattern of correlation observed in human scMRI mapping (Zielinski, Anderson et al. 2012).

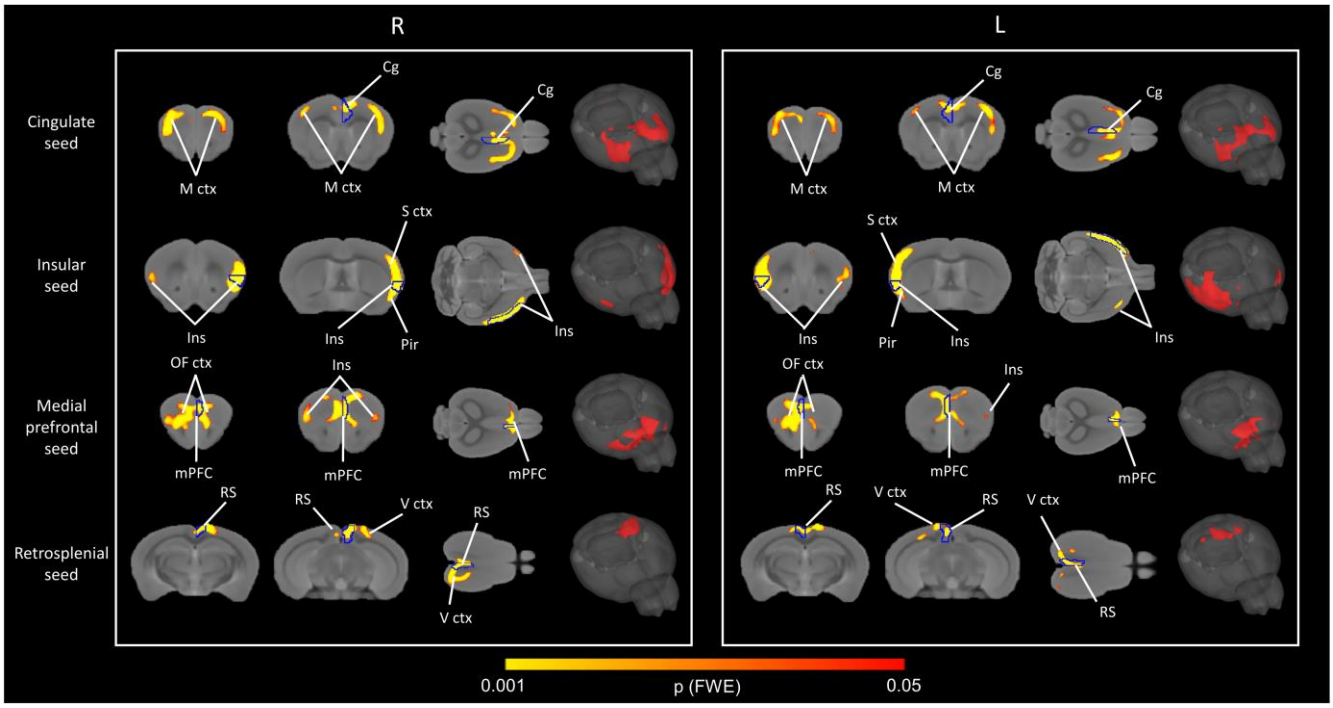

Figure 36. ScMRI networks: associative cortices. *Correlation maps for associative cortex gray matter volume seeds. We found positive symmetric associations between cingulate, prefrontal, insular and retrosplenial areas, and their homotopic contralateral regions. Threshold of statistical significance was set at p<0.05, FEW corrected for multiple comparisons. Cg ctx: cingulate ctx; Ins: Insula; mPFC: medial prefrontal cortex; M ctx: motor ctx; OF ctx: orbitofrontal cortex; Pir: Piriform cortex; RS: retrosplenial cortex; S ctx: somatosensory cortex; V ctx: visual cortex.*

Importantly, analogous network configurations were also identified using SBM (**Figure 37**). Specifically, six components recapitulated anatomical features of the cortical networks identified with seed-based mapping. These included a medial prefrontal, auditory-visual, insular, retrosplenial, motor-cingulate and somatosensory component (**Figure 37**). In keeping with seed-based correlation mapping, all the networks identified exhibited symmetric homotopic

distribution, although the degree of symmetry produced by SBM was lower than observed with seed mapping.

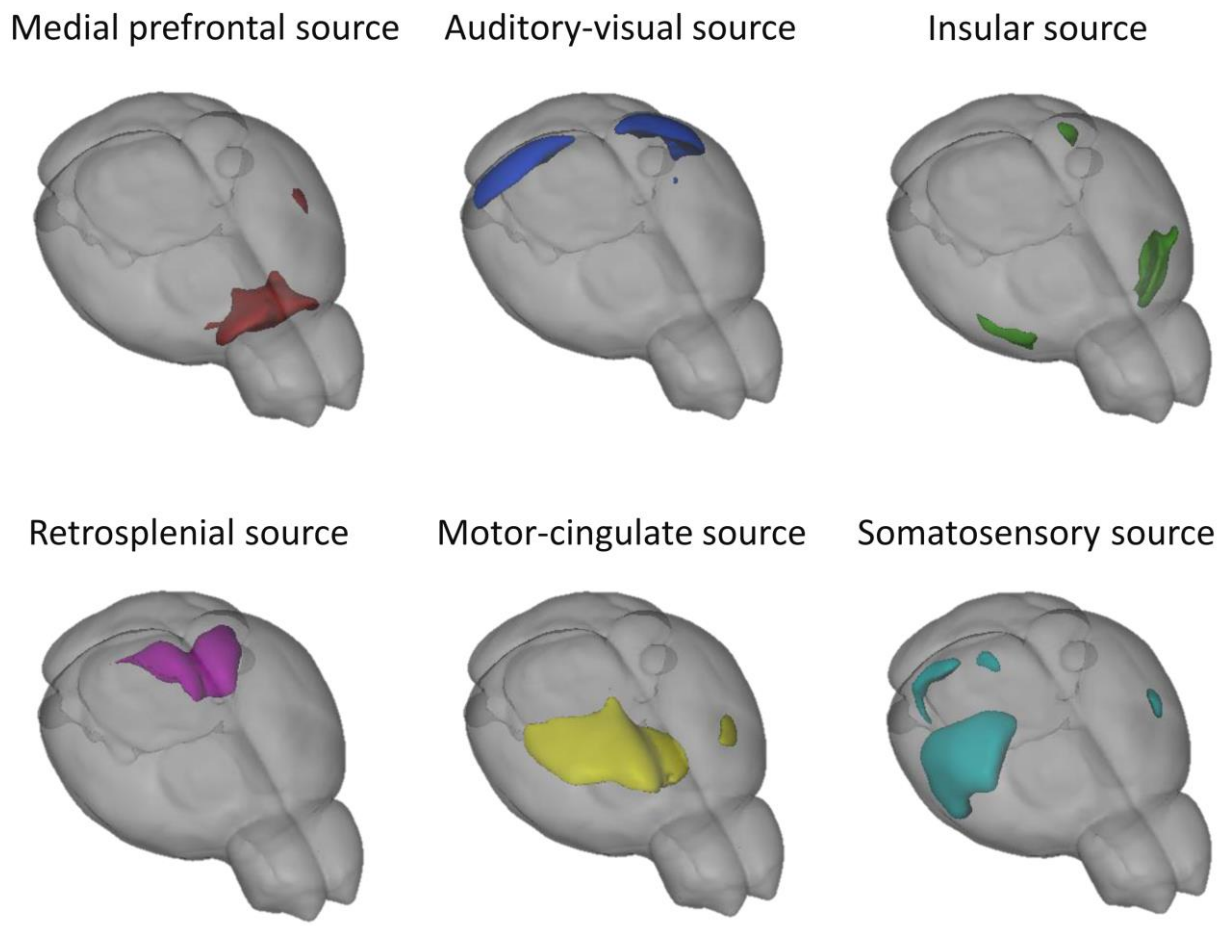

Figure 37. Source based morphometry of the cerebral cortex. *Six bilateral homotopic independent components were identified with SBM, including a medial prefrontal, an auditory-visual, an insular, a retrosplenial, a motor-cingulate and a somatosensory source. The anatomical distribution of these components exhibits overlap with correlative networks found using seed-based analysis.*

Seed-based correlation mapping of subcortical structures such as the amygdala, the caudate putamen, the thalamus and hypothalamus also showed positive, highly bilateral inter-hemispheric correlations encompassing homotopic brain regions. Interestingly, the diencephalic structures probed (thalamus, and hypothalamus) revealed reciprocal extensive antero-posterior network distribution to involve additional subcortical systems (i.e. the striatum),

in keeping with the results of our cluster analysis. The amygdala network also revealed significant ipsilateral involvement of rhinal cortex **Figure 38**.

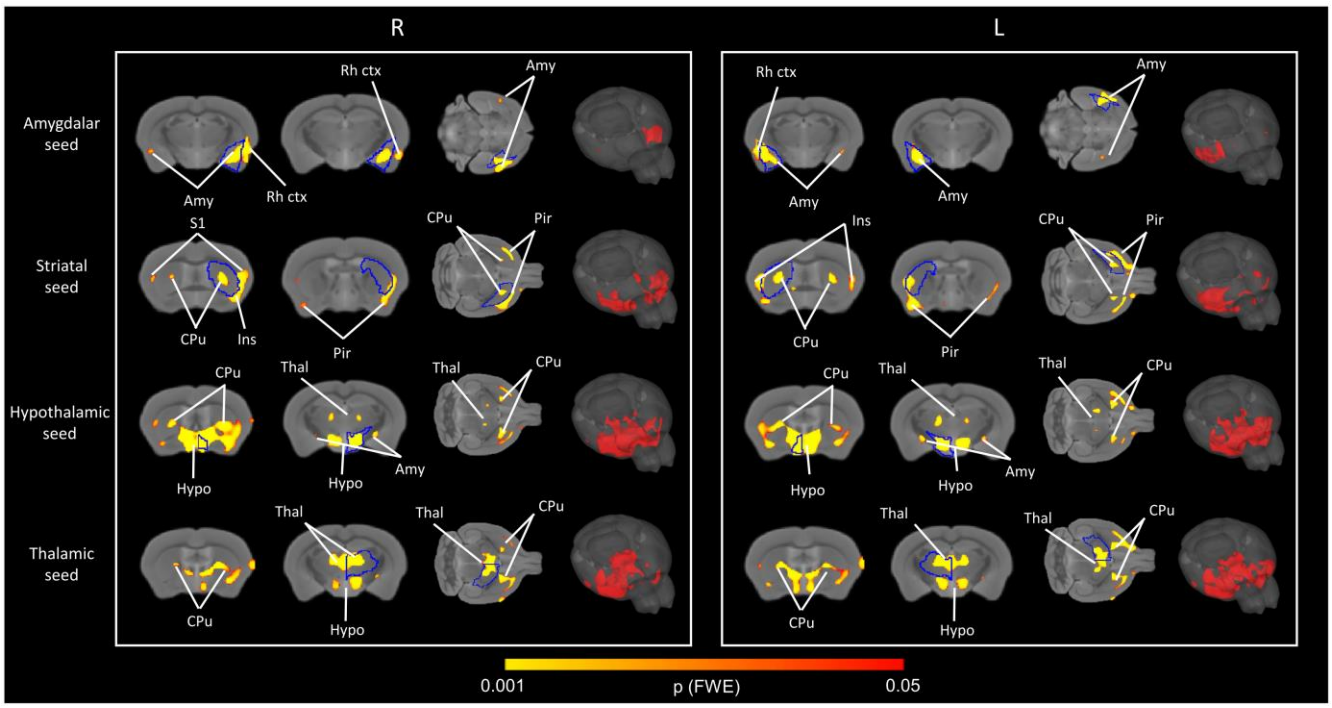

Figure 38. ScMRI networks: subcortical regions. *Correlation maps for subcortical gray matter volume seeds. Subcortical structures showed highly symmetric patterns of inter-hemispheric correlations, with evidence of distributed bilateral correlations in the thalamus and hypothalamus. Threshold of statistical significance was set at p<0.05, FEW corrected for multiple comparisons. Amy: amygdala; CPu: striatum; Hypo: hypothalamus; Ins: insula; Rh ctx: rhinal cortex; S1: primary somatosensory cortex; Thal: thalamus.*

Seed-based probing of ventral and dorsal hippocampus did not shown any significant inter-hemispheric correlation with other brain areas. Interestingly, a large involvement of hippocampal areas was observed when septal nuclei were used as seeds (**Figure 39**), to delineate a highly symmetric antero-distributed septo-hippocampal network reminiscent of in vivo functional networks previously identified in rodents (Gozzi, Crestan et al. 2010, Teles-Grilo Ruivo and Mellor 2013). The network however did not survive the family-wise correction threshold employed in this study. These results demonstrate the presence of bilateral

homotopic grey matter covariance networks in the mouse brain recapitulating anatomical covariance features recently observed in human brain studies.

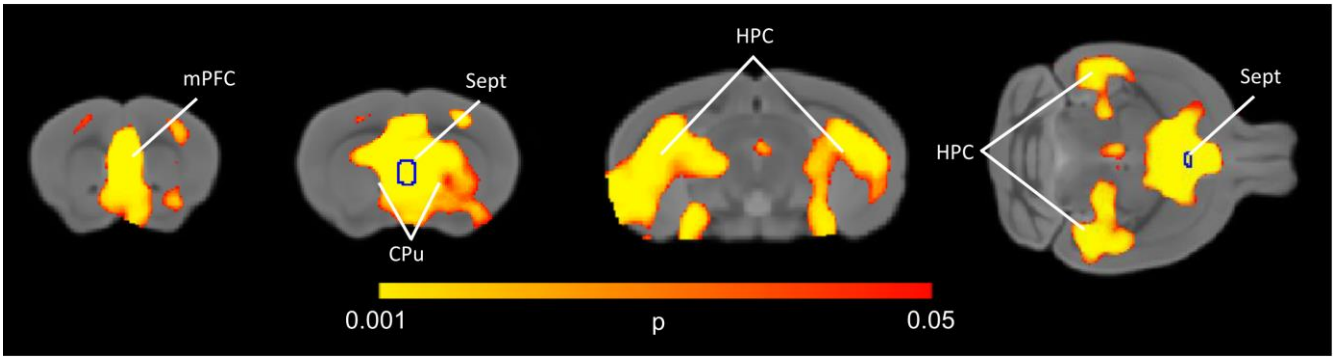

Figure 39. Septo-hippocampal network. *Seed-correlation map obtained using septal gray matter volume. The approach highlighted a bilateral antero-distributed septo-hippocampal network. Threshold of statistical significance was set at p<0.05 (uncorrected). CPu=caudate putamen; HPC=hippocampus; mPFC=medial prefrontal cortex; Sept=septal nucleus.*

To obtain an initial estimate of power necessary to reliably map covariance networks in the mouse, we performed a simple seed-based analysis of a representative cortical and subcortical network (auditory and hypothalamus, respectively) employing increasing numbers (i.e. 10, 20, 30, 40, 53) of randomly selected subjects from our subjects cohort. The results of this analysis () revealed emergence of robust covariance networks with a sample size of approximately 30-40 subjects. We note that such sample size is in line with those typically employed in human studies (Montembeault, Joubert et al. 2012, Zielinski, Anderson et al. 2012, Khundrakpam, Reid et al. 2013). We also empirically assessed the effect of smoothing on the distribution of covariance network (***Figure 41***). To this purpose, we generated scMRI maps for our two representative seed volumes (auditory cortex and hypothalamus) at varying smoothing sizes. For both seeds, significant homotopic brain covariance was evident also in unsmoothed data thus arguing against a major confounding contribution of this procedure to our findings. As expected, increased smoothing was associated with a larger extension of contralateral regions,

although the overall anatomical distribution of the affected areas appears to be overall conserved.

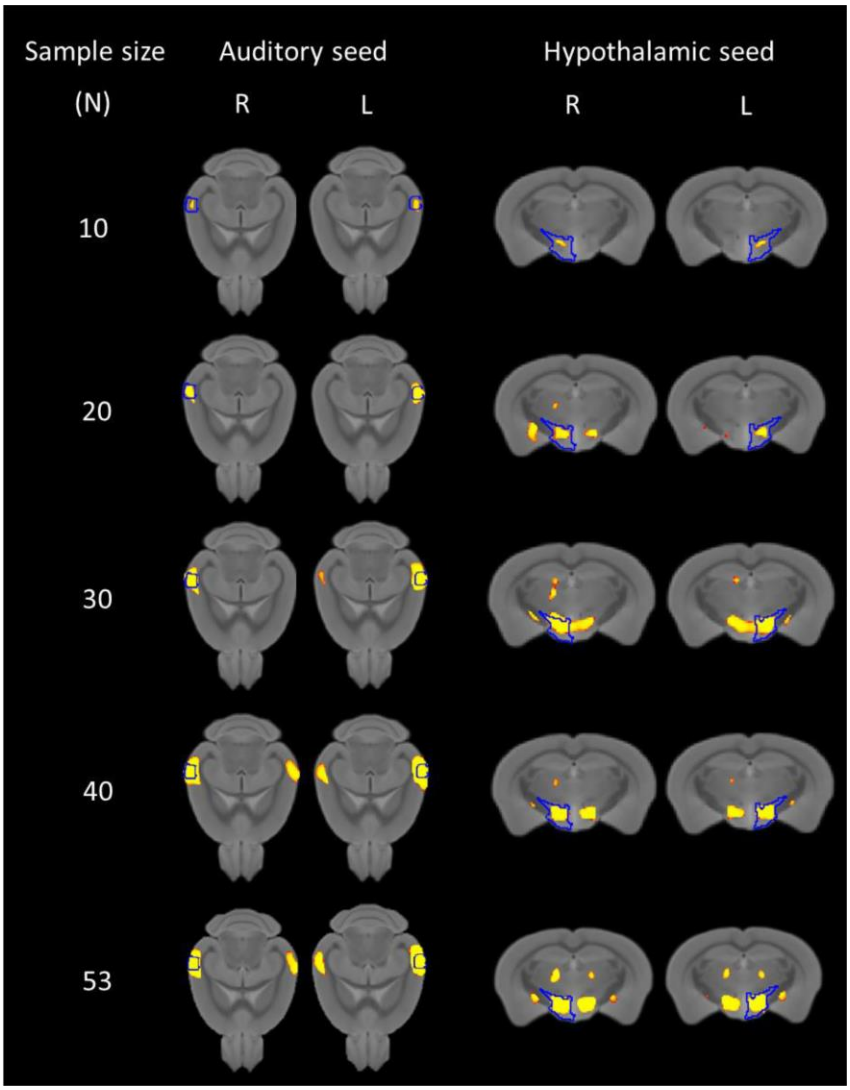

Figure 40. Impact of sample size on scMRI. *Seed-based analysis of a representative cortical and subcortical network (auditory and hypothalamus, respectively) employing increasing sample sizes. Emergence of statistically significant bilateral covariance networks is apparent with a minimum sample size of 30 subjects.*

To investigate whether gray matter scMRI is affected by neuroanatomical proximity, we correlated Euclidian distance (in mm) between each pair of VOI and their covariance strength (Pearson's correlation). This resulted in a correlation plot containing 19503 observations (198

* 197 / 2), illustrated in **Figure 42**. A significant correlation between anatomical distance and covariance strength was found (r=0.21; p<0.0001), although the gentle regression slope indicated a relatively small contribution of this phenomenon to the covariance strength observed.

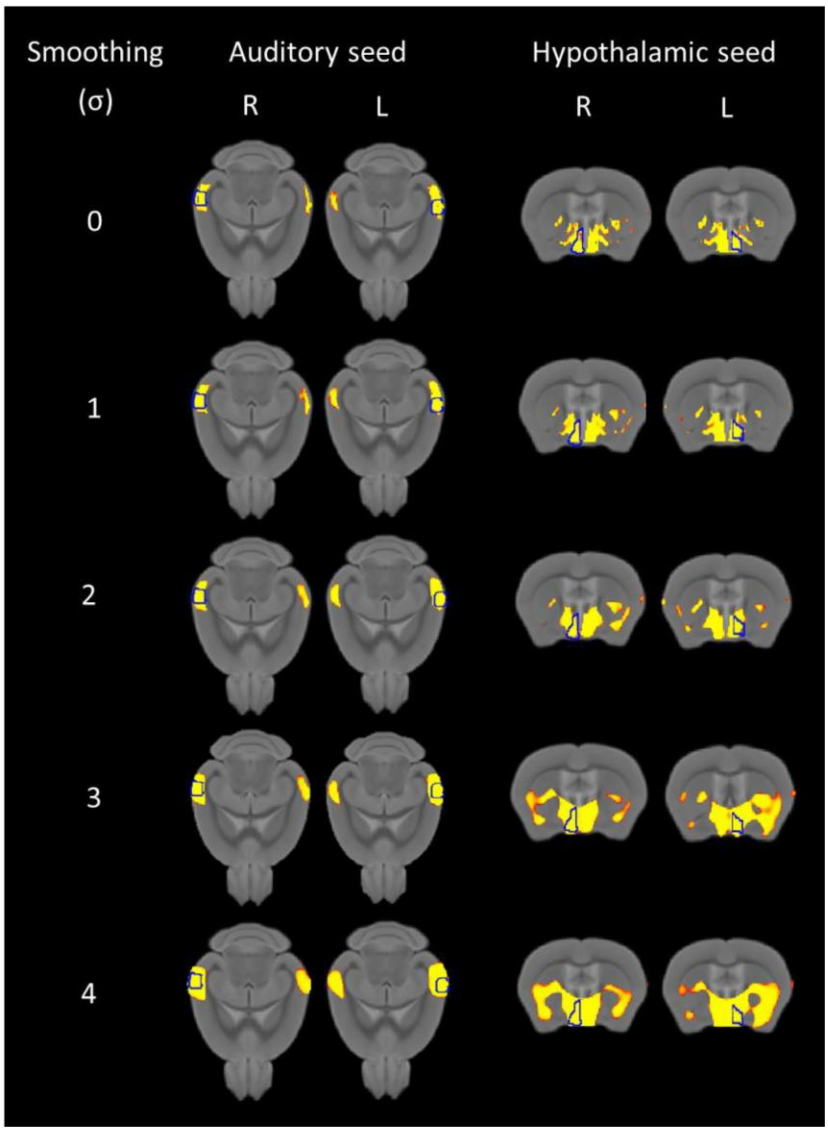

Figure 41. Impact of smoothing on scMRI. *To investigate the impact of smoothing, we use our representative cortical and subcortical seeds (auditory and hypothalamus) to study the behavior of scMRI at different size of smoothing, by varying sigma from 0 (no smoothing) to 4 voxels.*

In keeping with this, the scatterplot shows high density of VOI pairs exhibiting high covariance despite being substantially far apart (e.g. > 5 mm).

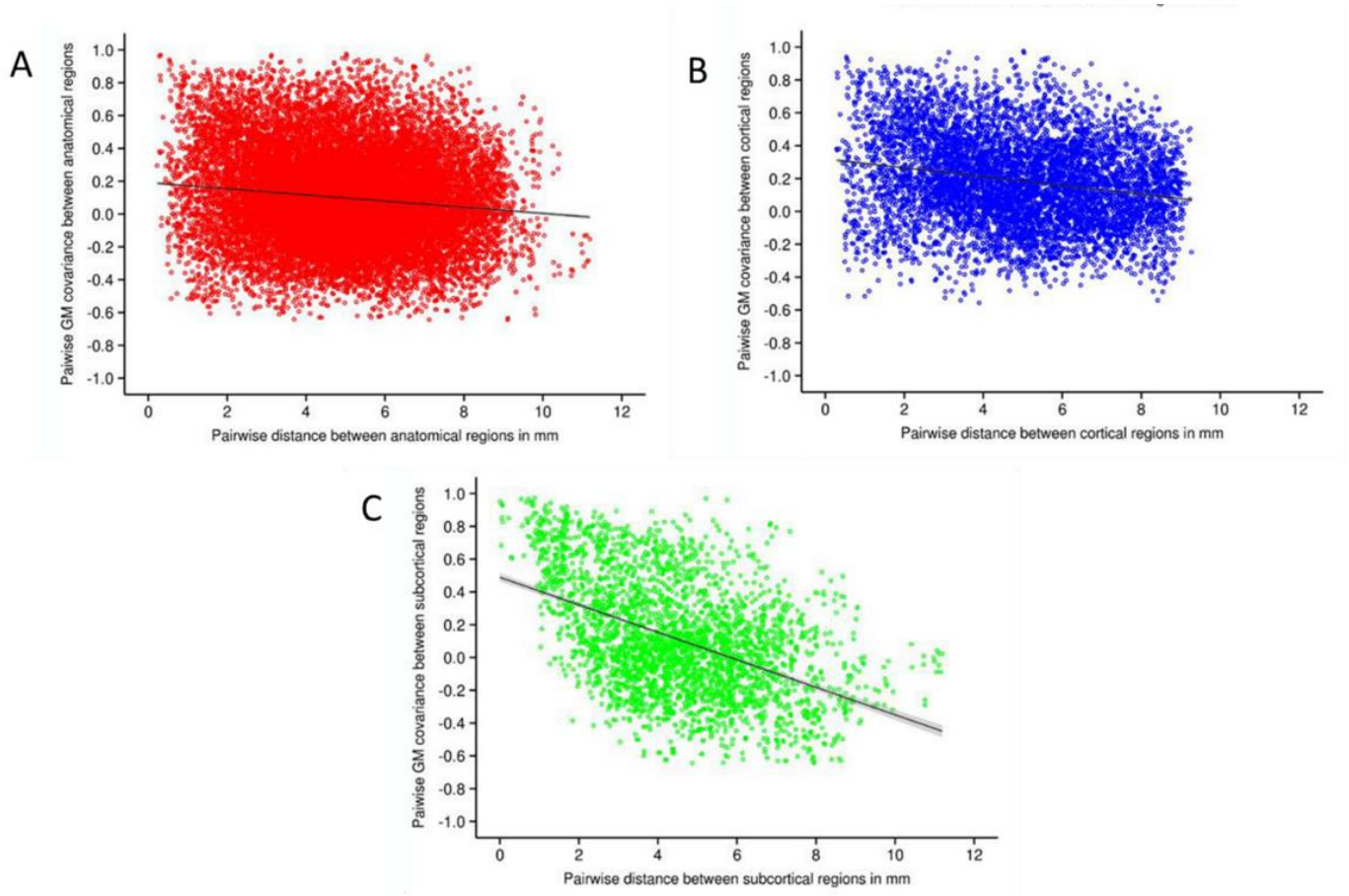

Figure 42. Correlation plot between physical distance and covariance strength. *To investigate the effect of physical distance of scMRI, we correlate the distance between each pair of regions with the covariance between those regions. We found a moderately low correlation coefficient, indicating that mutual trophic influence occurs at different brain scales and is only marginally associated with anatomical proximity (A). Similar results were found when the correlation between physical distance and covariance strength was investigated only in cortical regions (B). The profile of extra-cortical pairs of anatomical regions exhibited instead a shift from positive to negative correlations as the anatomical distance between regions increases (C). 95% CI are reported in grey.*

Some of these long distance covariance relationships are also depicted in our seed based mapping (e.g. insular, visual, amygdala, or thalamo-striatal covariance, **Figure 36** and **Figure**

38). Collectively, this observation suggests that mutual trophic influence occurs at different brain scales and is only marginally associated with (or driven by) anatomical proximity. Further cross comparisons with a mouse axonal density may help probe a putative connectional origin for this relationship. We also generated distinct plots for cortical and subcortical areas (**Figure 42**). The cortical plot recapitulates features observed with the whole set of regions. The profile of extracortical VOI pairs exhibited instead a shift from positive to negative correlations as the anatomical distance between regions increases.

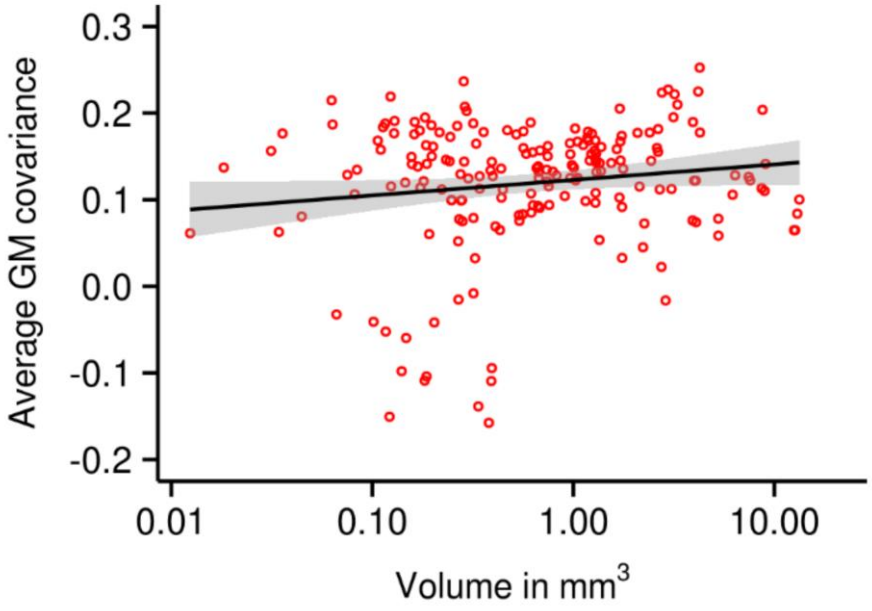

Figure 43. Correlation plot between region size and covariance strength. *To investigate a role of volumetric VOI heterogeneity in determining correlation strength, we correlated the size of each of the 198 VOIs with the average covariance of that VOI with all the other brain regions. Pearson's correlation coefficient of this correlation was not significant (r=0.04; p=0.58), 95% CI are reported in grey.*

This finding is consistent with voxelwise covariance mapping at the voxel level (**Figure 33**, discussed below) showing anti-correlation between subcortical brainstem regions and cortical areas, thus revealing a competing interaction in regional volumetric variability affecting mostly

long-range subcortical regions (e.g. brainstem and striatum). We also probed the correlation between region size (volume in mm3) and covariance strength (mean covariance between each pair of volumes). As reported in **Figure 43**, no significant correlation between these two metrics was found (Pearson's r = 0.04; p=0.58).

4.4. Discussion

Our work documents the presence of covarying regional gray matter volumes in a cohort of inbred laboratory mice, defining macroscale correlational networks characterized by high neuroanatomical specificity, which could be clustered into antero-cortical, cortico-hippocampal and subcortical limbic components. Consistent with previous findings in humans (Mechelli, Friston et al. 2005, Chen, He et al. 2008, Zielinski, Gennatas et al. 2010), the covariance patterns identified showed strong symmetric correlations among gray matter volumes of homologous brain regions. Robust scMRI correlations were observed both in cortical and sub-cortical structures, with the latter including the mutual involvement of diencephalic and striatal areas to define an extended antero-posterior network, as well as a septo-hippocampal network. Complementary computational and mapping approaches (e.g. hierarchical clustering, seed-based mapping and SBM) produced consistent results, thus supporting the robustness of our findings. Moreover, the use of brain size corrected volumes permits to rule out a purely allometric origin for the mapped networks in favor of a trophic connectional origin (Szulc, Lerch et al. 2015).

Despite the increasing use of scMRI mapping in human studies, the application of this approach to animal models has been so far very limited, with the exception of a few notable examples in the field of nonhuman primate research (Alexander, Chen et al. 2008, Spocter, Hopkins et al. 2010, Shamy, Habeck et al. 2011). An exploratory covariance analysis of mouse brain regional volumes has been previously reported (Badea, Johnson et al. 2009), leading to the identification

of a large putative limbic network, but failing to highlight fine-grained homotopic cortical and subcortical scMRI networks analogous to those observed in humans. Our results demonstrate the existence of neuro-anatomically specific cortical and subcortical networks of covariance also in the laboratory mouse, thus extending the use of scMRI approaches to lower mammal species. In this respect our work may serve as a reference for future studies aimed at exploiting the increasing availability of mouse models and genetic tools to address open questions about the neurobiological, genetic and connectional determinants of these correlative networks, and generate hypothesis about their derangement in pathological states. Importantly, several of the identified networks have direct human homologues, thus enabling tentative cross species comparisons. For example, segregated somatosensory, visual, motor and auditory scMRI networks have been reliably identified in humans using seed-based approaches (Mechelli, Friston et al. 2005, Zielinski, Gennatas et al. 2010). ScMRI between midline cingulate and lateral cortical areas reminiscent of our findings has also been described (Zielinski, Gennatas et al. 2010), together with homotopic involvement of amygdala and peri-hippocampal cortical areas (Bohbot, Lerch et al. 2007). Importantly, the presence of symmetric short and long distance patterns of scMRI connecting interhemispheric regions recapitulate previous functional network mapping using resting-state functional MRI in humans (Salvador, Suckling et al. 2005) and mice (Sforazzini, Schwarz et al. 2014), thus highlighting common neuroanatomical substrates driving the emergence of these phenomena.

A cross-species comparison of cortical covariance patterns involving higher order cognitive areas is complicated by the lack of direct cytoarchitectural correlates of human cortical areas in the mouse as a result of the large evolutionary distance between human and rodents. The correlation between anterior cingulate, medial prefrontal and insular foci is nevertheless of interest as it recapitulates neuroanatomical features reminiscent of a human scMRI network

termed “salience network” (Zielinski, Anderson et al. 2012). This network was originally identified with resting-state fMRI and is involved in attribution of salience to behavioral stimuli (Seeley, Menon et al. 2007). Interestingly, empirical evidence of an analogous insular-cingulate “salience-like” functional connectivity network has been recently provided in the mouse using resting-state fMRI (Sforazzini, Bertero et al. 2014, Sforazzini, Schwarz et al. 2014), although an involvement of this functional network in mouse salience attribution remains to be demonstrated. While at present only speculative, the putative structural-functional correspondence observed in the mouse is noteworthy as it may parallel analogous human findings, supporting the translational significance of the approach also for associative areas involved in high level cognitive integration. Such a parallel was however not identified for the default mode network (DMN), a large functional connectivity network that in humans exhibits partial neuroanatomical overlap with scMRI patterns (Spreng and Turner 2013). Despite the recent identification of a plausible mouse brain DMN-homologue (Sforazzini, Schwarz et al. 2014, Liska, Galbusera et al. 2015) reflecting homologous antero-posterior brain axonal connectivity patterns (Oh, Harris et al. 2014), no midline gray matter covariance relatable to the DMN was observed in the present study, a finding at odds with some human scMRI reports (Zielinski, Gennatas et al. 2010, Spreng and Turner 2013). The lack of scMRI in antero-posterior midline regions exhibiting robust white matter connectivity such as the DMN supports the emerging view that the trophic processes driving the emergence of scMRI reflect macroscale integrative network activity that is only partially constrained by underlying axonal connectivity. Consistent with this, human white matter connectivity has been shown to describe less than 40% of scMRI (Gong, He et al. 2012). Direct comparisons with high-resolution mouse brain axonal tracing may help disentangle the elusive relationship between white matter and covariance gray matter connectivity.

Relative differences in the genetic variability of human population imaged and the inbred mouse cohort employed in the present study also need to be taken when attempting to extrapolate our results to clinical scMRI research. Human studies employing genetically heterogeneous subjects and homozygotic twins have demonstrated that both genes and the environment play a determinant contribution in shaping scMRI networks. For example, a relevant contribution of the environment in explaining cross-subjects cortical thickness variability of the occipital and temporal lobe has been demonstrated (Schmitt, Lenroot et al. 2009), although association between cortical and subcortical (Eyler, Prom-Wormley et al. 2011) homotopic was mainly attributable to genetic mechanisms. Similarly, genetic polymorphisms have been shown to affect the development and topology of specific scMRI networks (Pezawas, Meyer-Lindenberg et al. 2005, Alexander-Bloch, Giedd et al. 2013). The identification of scMRI networks also in genetically homogeneous inbred mice bred under standardized environmental conditions achievable in laboratory settings is a non-trivial finding that corroborates a significant amplifying influence of early life (e.g. maternal care, number of littermates), and minor environmental and experience-related factors in the emergence of these networks. This finding also suggests that heterogenic experience-related factors can induce gray matter neuroanatomical remodeling of neuronal processes not only at a the local (Lerch, Yiu et al. 2011) but also at the macroscale.

The use of outbred mouse strains or inbred crosses characterized by different genetic variability may be useful in assessing the relative contribution of genetic and environmental factors in controlling the emergence of distributed networks and their neuroanatomical extension. In this respect, it is interesting to note that during human development, scMRI networks are initially characterized by strict homotopic extension (e.g. similar to what we observed in the mouse), and assume broader cross-modal distribution in late adolescence and young adulthood, a trajectory that presumably reflects an interaction between neurodevelopmental and

environmental contributions. Future mouse studies may assess whether similar distributed network correlations could similarly emerge upon robust environmental enrichment in inbred and outbred strains. The controlled genetic variability related to the use of inbred mice has also practical implications for the design of future mouse scMRI research. The correlational nature of scMRI mapping and low variance observed in cortical regions imply that large sample size (e.g. at least 30-40, **Figure 40**) may be needed to adequately power studies aimed at detecting inter-group differences in scMRI networks, with values theoretically exceeding group size typically used in behavioral or molecular neuroscience research. Whether this is an intrinsic feature of the inbred mouse strain employed in this study, or a fundamental characteristic of the mammal brain remains to be determined, although the wide use of similarly powered samples in human covariance studies (Montembeault, Joubert et al. 2012, Zielinski, Anderson et al. 2012, Khundrakpam, Reid et al. 2013) favors the second hypothesis.

In conclusion, here we describe robust inter-hemispheric scMRI networks in the laboratory mouse, characterized by high neuroanatomical specificity and involving cortical and subcortical regions. Our work may guide future investigations on the emergence of these correlative networks, and pave the way to the investigation of the underpinnings of scMRI alterations of pathological relevance.

5. Conclusion

Structural MRI methods based on volumetric quantification have been extensively applied over the last decades to study the human brain in healthy and pathological states. ScMRI represents a step forward compared to standard volumetric techniques since it permits to elucidate the trophic dynamics between brain regions and has the potential to unravel the trophic organization of the brain at the network level. However, the specific neurobiological determinants of scMRI network coupling remain debated.

To probe the presence of scMRI networks in the mouse brain, I used seed-based analysis based on permutation as implemented in FSL randomize (Winkler, Ridgway et al. 2014). Permutation testing is a non-parametric statistical framework that can be used regardless the distribution profile of the data (Holmes, Blair et al. 1996). Seed based mapping generates multiple gray matter correlation coefficients (equal to the number of voxels in the brain) that need to be controlled for type-I errors (Nichols and Holmes 2002). To this aim, I used a strict family-wise error rate correction (FWER, $p<0.05$) and I calculated the permutation distribution of the maximal correlation coefficient over the entire mouse brain considering significant only the correlation coefficients that were in the top 5% of the distribution of the maximal correlation (Nichols and Holmes 2002). Importantly, this rigorous correction strategy has been successfully used to map scMRI networks in a number of previous human studies (Mechelli, Friston et al. 2005, Coppen, van der Grond et al. 2016, Bassett, Bullmore et al. e2008).

Because human studies are typically based on large cohort of individuals, I applied covariance network mapping methods to a similarly big cohort of mice (n=53). However, the typical sample size of a neuroscientific experiment involving different experimental arms is usually much smaller than this (e.g. n=8-12). This was the case for two of the studies I performed as part of

my PhD research (Cutuli, Pagani et al. 2016, Lassi, Priano et al. 2016) in which smaller experimental groups were used (n=9-12 per group). In the above two studies, the FWER approach appeared to be too conservative, leading to the rejection of inter-group differences that were otherwise bilateral, region-specific and remarkably consistent with the experimental hypotheses underlying these two studies. To circumvent this problem, I used ordinary least squares (OLS) followed by cluster-based correction, a more liberal, yet rigorous, multiple comparison correction approach widely employed in structural imaging studies (Good, Johnsrude et al. 2003, Modinos, Costafreda et al. 2013, Jednorog, Marchewka et al. 2015, Khan, Wang et al. 2015). In order to meet normality assumption, I introduced spatial smoothing to brain volumes prior to statistics, as previously described (Salmond, Ashburner et al. 2002). As expected, by using this procedure we obtained undistinguishable results when using permutation statistics or OLS mapping (**Figure 44**).

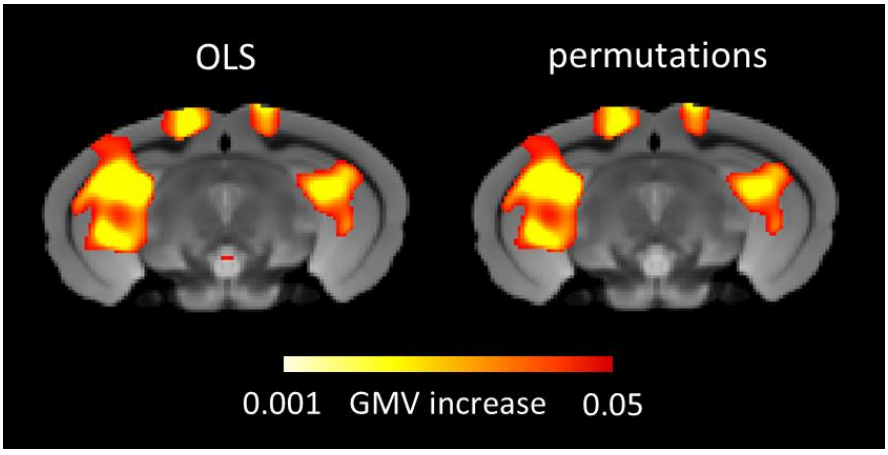

Figure 44. Exemplificative comparison between OLS and permutation statistical testing. *OLS and permutation-based statistics yield virtually undistinguishable results in term of significant foci of increased GM volumes. Red-yellow coloring show increased hippocampal and retrosplenial GM volume in mice treated with omega-3 compared to control mice treated with olive oil.*

OLS maps were subsequently thresholded using a cluster based correction for multiple comparisons (Worsley, Evans et al. 1992). This method defines clusters as sets of contiguous

voxels whose intensity exceeds a statistically significant threshold ($p<0.01$), and tests the null hypothesis by using random fields to examine whether the spatial extent of these clusters is unusually large than by chance alone (Hayasaka and Nichols 2003). This strategy revealed to be sensitive enough to reveal hippocampal increase in GM volume in the group of mice treated with omega-3, an effect consistent with previous mouse studies (Gómez-Pinilla 2008, Cutuli, De Bartolo et al. 2014) and human literature (Pottala, Yaffe et al. 2014) as well as with behavioral improvement in hippocampal based cognitive functioning exhibited by nPUFA treated mice (Figure 31). Importantly, a key confirmation of the validity of this approach is its excellent correspondence with the results of inter-group volumetric anatomical labelling in the same datasets. For example, all the studies I performed using VBM revealed excellent neuroanatomical agreement between regions exhibiting statistically significant volumetric labelling and corresponding foci of significant GMV in VBM maps. This observation provides crucial empirical support to the cluster-based thresholding strategy employed (Cutuli, Pagani et al. 2016, Lassi, Priano et al. 2016), that can be also used to correct permutation based statistics (Salimi-Khorshidi, Smith et al. 2011), as shown in VBM morphoanatomical measurements in BTBR mice (Pagani, Damiano et al. 2016).

The VBM pipeline heavily relies upon image registration, a step employed in the creation of the study based template, normalization of images and calculation of Jacobian determinants. As shown in Figure 19, I took great care in making sure that this crucial step is performed accurately by running a high number of pilot studies to find the better parameters for the antsRegistration tool via measurements of Dice coefficients. The results of this optimization show an excellent agreement between automated and manual registrations in all brain regions tested (Figure 19) and are in line with those of other lab (Badea, Gewalt et al. 2012). Regarding cortical thickness, the pipeline based on DiReCT is capable to produce results in excellent

correspondence (Figure 17; r=0.99; p<0.001) with manual thickness measurements in secondary motor (M2), secondary somatosensory (S2) and auditory cortex (Au). Importantly, the sensitivity of all these readouts was also previously validated in previous studies (Das, Avants et al. 2009, Avants, Tustison et al. 2011, Tustison, Cook et al. 2014), from which we replicated the computational parameters

Also, the quality of segmentation was assessed empirically by comparing individual and merged tissue classes with the anatomical distribution of known high-density white matter structures such as the corpus callosum, anterior and posterior commissures, as seen in the study-based template. These structures are easily identifiable when compared with their segmented counterparts (**Figure 45**).

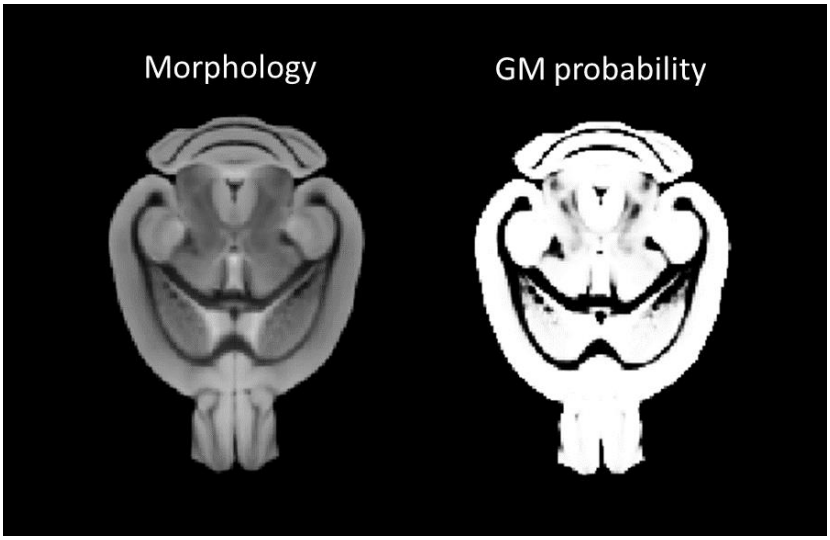

Figure 45. Segmented probability maps trace anatomical images. *Segmented GM probability maps (colored in white in the right image) showed a great overlapping with the anatomy of morphological images. Cerebral and cerebellar cortex, hippocampus, striatum and other major gray matter regions are clearly labelled as GM, whereas corpus callosum and the other major fiber bundles are labelled as non-GM and then correctly excluded from following analysis.*

Overall the segmentation procedure appears to efficiently and clearly separate high density gray and white matter regions. However, the lack of a “ground truth” spatial tissue distribution,

and the presence of tissues with variable proportion of white and gray matter have so far prevented an unbiased validation of the employed segmentation strategies, with the accuracy of this step being in most case still entirely operator dependent. The use of tensor based morphometry (a straightforward extension of our procedure) can help increase confidence of inter-group differences observed in regions at the interface of white/gray matter. Future extension of this initial workflow could employ quantitative approaches to estimate goodness of cluster separation (Chou, Su et al. 2004, Wu and Yang 2005), although operator dependent assessments of the tissue class separations are ultimately warranted to ensure biologically meaningful results.

To conclude, my research has focused on the development and application of MRI-based methods to map structural covariance in the laboratory mouse, hence enabling the possibility of causally probing the contribution of genetic, cellular and environmental challenges in morphing the establishment of these networks. This research led to the first description of neuroanatomically meaningful covariance patterns that recapitulate key topological features of the human brain, thus defining scMRI as a novel translational tool to bridge clinical and preclinical research. My results open the way to the investigation of brain structural architecture in the laboratory mouse. For example, the application of scMRI networks in genetically modified mouse lines recapitulating human pathological mutations in experimentally controlled studies can produce valuable insights about causal links between specific genetic mutations and clinically relevant scMRI endophenotypes. The application of this approach to mouse lines harboring autism-related mutation is currently in progress.

Collectively, my work supports the use of scMRI in the mouse to generate hypotheses about derangement of structural covariance in pathological states of clinical relevance and provides

a novel mechanistic and translational perspective on the elusive pathological mechanisms of neuro-psychiatric disorders such as autism and schizophrenia.

6. References

Aggarwal, M., J. Zhang, M. I. Miller, R. L. Sidman and S. Mori (2009). "Magnetic resonance imaging and micro-computed tomography combined atlas of developing and adult mouse brains for stereotaxic surgery." Neuroscience **162**(4): 1339-1350.

Albaugh, M. D., S. Ducharme, D. L. Collins, K. N. Botteron, R. R. Althoff, A. C. Evans, S. Karama, J. J. Hudziak and B. D. C. Group (2013). "Evidence for a cerebral cortical thickness network anti-correlated with amygdalar volume in healthy youths: implications for the neural substrates of emotion regulation." Neuroimage **71**: 42-49.

Alexander-Bloch, A., J. N. Giedd and E. Bullmore (2013). "Imaging structural co-variance between human brain regions." Nature Reviews Neuroscience **14**(5): 322-336.

Alexander-Bloch, A., A. Raznahan, E. Bullmore and J. Giedd (2013). "The convergence of maturational change and structural covariance in human cortical networks." The Journal of Neuroscience **33**(7): 2889-2899.

Alexander, G. E., K. Chen, M. Aschenbrenner, T. L. Merkley, L. E. Santerre-Lemmon, J. L. Shamy, W. E. Skaggs, M. H. Buonocore, P. R. Rapp and C. A. Barnes (2008). "Age-related regional network of magnetic resonance imaging gray matter in the rhesus macaque." The Journal of Neuroscience **28**(11): 2710-2718.

Andrews, T. J., S. D. Halpern and D. Purves (1997). "Correlated size variations in human visual cortex, lateral geniculate nucleus, and optic tract." The Journal of Neuroscience **17**(8): 2859-2868.

Ashburner, J. and K. J. Friston (2000). "Voxel-based morphometry--the methods." NeuroImage **11**(6 Pt 1): 805-821.

Avants, B. B., P. A. Cook, L. Ungar, J. C. Gee and M. Grossman (2010). "Dementia induces correlated reductions in white matter integrity and cortical thickness: a multivariate neuroimaging study with sparse canonical correlation analysis." NeuroImage **50**(3): 1004-1016.

Avants, B. B., C. L. Epstein, M. Grossman and J. C. Gee (2008). "Symmetric diffeomorphic image registration with cross-correlation: Evaluating automated labeling of elderly and neurodegenerative brain." Medical Image Analysis **12**(1): 26-41.

Avants, B. B., N. Tustison and G. Song (2009). "Advanced normalization tools (ANTS)." Insight J.

Avants, B. B., N. J. Tustison, G. Song, P. A. Cook, A. Klein and J. C. Gee (2011). "A reproducible evaluation of ANTs similarity metric performance in brain image registration." Neuroimage **54**(3): 2033-2044.

Avants, B. B., N. J. Tustison, M. Stauffer, G. Song, B. Wu and J. C. Gee (2014). "The Insight ToolKit image registration framework." Frontiers in neuroinformatics **8**.

Avants, B. B., N. J. Tustison, J. Wu, P. A. Cook and J. C. Gee (2011). "An open source multivariate framework for n-tissue segmentation with evaluation on public data." Neuroinformatics **9**(4): 381-400.

Avants, B. B., P. Yushkevich, J. Pluta, D. Minkoff, M. Korczykowski, J. Detre and J. C. Gee

(2010). "The optimal template effect in hippocampus studies of diseased populations." NeuroImage **49**(3): 2457-2466.

Badea, A., A. A. Ali-Sharief and G. A. Johnson (2007). "Morphometric analysis of the C57BL/6J mouse brain." NeuroImage **37**(3): 683-693.

Badea, A., S. Gewalt, B. B. Avants, J. J. Cook and G. A. Johnson (2012). "Quantitative mouse brain phenotyping based on single and multispectral MR protocols." Neuroimage **63**(3): 1633-1645.

Badea, A., G. Johnson and R. Williams (2009). "Genetic dissection of the mouse brain using high-field magnetic resonance microscopy." Neuroimage **45**(4): 1067-1079.

Bassett, D. S., E. Bullmore, B. A. Verchinski, V. S. Mattay, D. R. Weinberger and A. Meyer-Lindenberg (2008). "Hierarchical organization of human cortical networks in health and schizophrenia." The Journal of neuroscience **28**(37): 9239-9248.

Bazan, N. G., A. E. Musto and E. J. Knott (2011). "Endogenous signaling by omega-3 docosahexaenoic acid-derived mediators sustains homeostatic synaptic and circuitry integrity." Molecular neurobiology **44**(2): 216-222.

Bell, A. J. and T. J. Sejnowski (1995). "An information-maximization approach to blind separation and blind deconvolution." Neural computation **7**(6): 1129-1159.

Bernhardt, B. C., O. M. Klimecki, S. Leiberg and T. Singer (2013). "Structural covariance networks of the dorsal anterior insula predict females' individual differences in empathic responding." Cerebral Cortex: bht072.

Bohbot, V. D., J. Lerch, B. Thorndycraft, G. Iaria and A. P. Zijdenbos (2007). "Gray matter differences correlate with spontaneous strategies in a human virtual navigation task." The Journal of Neuroscience **27**(38): 10078-10083.

Borg, J. and E. Chereul (2008). "Differential MRI patterns of brain atrophy in double or single transgenic mice for APP and/or SOD." J Neurosci Res **86**(15): 3275-3284.

Brodmann, K. (1909). Vergleichende Lokalisationslehre der Grosshirnrinde in ihren Prinzipien dargestellt auf Grund des Zellenbaues, Barth.

Budin, F., M. Hoogstoel, P. Reynolds, M. Grauer, S. K. O'Leary-Moore and I. Oguz (2013). "Fully automated rodent brain MR image processing pipeline on a Midas server: from acquired images to region-based statistics." Front Neuroinform **7**: 15.

Bullmore, E. and O. Sporns (2009). "Complex brain networks: graph theoretical analysis of structural and functional systems." Nature Reviews Neuroscience **10**(3): 186-198.

Cahill, L. S., C. L. Laliberte, J. Ellegood, S. Spring, J. A. Gleave, M. C. Eede, J. P. Lerch and R. M. Henkelman (2012). "Preparation of fixed mouse brains for MRI." Neuroimage **60**(2): 933-939.

Calder, P. C. (2011). "Fatty acids and inflammation: the cutting edge between food and pharma." European journal of pharmacology **668**: S50-S58.

Calviello, G., P. Palozza, P. Franceschelli and G. M. Bartoli (1997). "Low-dose eicosapentaenoic or docosahexaenoic acid administration modifies fatty acid composition and does not affect susceptibility to oxidative stress in rat erythrocytes and tissues." Lipids **32**(10): 1075-1083.

Carrie, I., M. Smirnova, M. Clement, J. De, H. Frances and J. Bourre (2002). "Docosahexaenoic

acid-rich phospholipid supplementation: effect on behavior, learning ability, and retinal function in control and n-3 polyunsaturated fatty acid deficient old mice." Nutritional Neuroscience **5**(1): 43-52.

Chen, G., K. S. Chen, J. Knox, J. Inglis, A. Bernard, S. J. Martin, A. Justice, L. McConlogue, D. Games and S. B. Freedman (2000). "A learning deficit related to age and β-amyloid plaques in a mouse model of Alzheimer's disease." Nature **408**(6815): 975-979.

Chen, Z. J., Y. He, P. Rosa-Neto, J. Germann and A. C. Evans (2008). "Revealing modular architecture of human brain structural networks by using cortical thickness from MRI." Cerebral cortex **18**(10): 2374-2381.

Chiu, C.-C., K.-P. Su, T.-C. Cheng, H.-C. Liu, C.-J. Chang, M. E. Dewey, R. Stewart and S.-Y. Huang (2008). "The effects of omega-3 fatty acids monotherapy in Alzheimer's disease and mild cognitive impairment: a preliminary randomized double-blind placebo-controlled study." Progress in Neuro-Psychopharmacology and Biological Psychiatry **32**(6): 1538-1544.

Chou, C.-H., M.-C. Su and E. Lai (2004). "A new cluster validity measure and its application to image compression." Pattern Analysis and Applications **7**(2): 205-220.

Conklin, S. M., P. J. Gianaros, S. M. Brown, J. K. Yao, A. R. Hariri, S. B. Manuck and M. F. Muldoon (2007). "Long-chain omega-3 fatty acid intake is associated positively with corticolimbic gray matter volume in healthy adults." Neuroscience letters **421**(3): 209-212.

Coppen, E. M., J. van der Grond, A. Hafkemeijer, S. A. Rombouts and R. A. Roos (2016). "Early grey matter changes in structural covariance networks in Huntington's disease." NeuroImage: Clinical **12**: 806-814.

Costa, A. P. R., C. Vieira, L. O. Bohner, C. F. Silva, E. C. da Silva Santos, T. C. M. De Lima and C. Lino-de-Oliveira (2013). "A proposal for refining the forced swim test in Swiss mice." Progress in Neuro-Psychopharmacology and Biological Psychiatry **45**: 150-155.

Crawley, J. and F. K. Goodwin (1980). "Preliminary report of a simple animal behavior model for the anxiolytic effects of benzodiazepines." Pharmacology Biochemistry and Behavior **13**(2): 167-170.

Cunnane, S., M. Plourde, F. Pifferi, M. Bégin, C. Féart and P. Barberger-Gateau (2009). "Fish, docosahexaenoic acid and Alzheimer's disease." Progress in lipid research **48**(5): 239-256.

Cutuli, D., P. De Bartolo, P. Caporali, D. Laricchiuta, F. Foti, M. Ronci, C. Rossi, C. Neri, G. Spalletta and C. Caltagirone (2014). "n-3 polyunsaturated fatty acids supplementation enhances hippocampal functionality in aged mice." Frontiers in aging neuroscience **6**: 220.

Cutuli, D., M. Pagani, P. Caporali, A. Galbusera, D. Laricchiuta, F. Foti, C. Neri, G. Spalletta, C. Caltagirone and L. Petrosini (2016). "Effects of omega-3 fatty acid supplementation on cognitive functions and neural substrates: a voxel-based morphometry study in aged mice." Frontiers in aging neuroscience **8**.

Dangour, A. D., E. Allen, D. Elbourne, N. Fasey, A. E. Fletcher, P. Hardy, G. E. Holder, R. Knight, L. Letley and M. Richards (2010). "Effect of 2-yn− 3 long-chain polyunsaturated fatty acid supplementation on cognitive function in older people: a randomized, double-blind, controlled trial." The American journal of clinical nutrition **91**(6): 1725-1732.

Danthiir, V., N. R. Burns, T. Nettelbeck, C. Wilson and G. Wittert (2011). "The older people, omega-3, and cognitive health (EPOCH) trial design and methodology: a randomised, double-blind, controlled trial investigating the effect of long-chain omega-3 fatty acids on

cognitive ageing and wellbeing in cognitively healthy older adults." Nutrition journal **10**(1): 1.

Das, S. R., B. B. Avants, M. Grossman and J. C. Gee (2009). "Registration based cortical thickness measurement." Neuroimage **45**(3): 867-879.

Delatour, B., M. Guegan, A. Volk and M. Dhenain (2006). "In vivo MRI and histological evaluation of brain atrophy in APP/PS1 transgenic mice." Neurobiol Aging **27**(6): 835-847.

Denis, I., B. Potier, C. Heberden and S. Vancassel (2015). "Omega-3 polyunsaturated fatty acids and brain aging." Current Opinion in Clinical Nutrition & Metabolic Care **18**(2): 139-146.

Denis, I., B. Potier, S. Vancassel, C. Heberden and M. Lavialle (2013). "Omega-3 fatty acids and brain resistance to ageing and stress: body of evidence and possible mechanisms." Ageing research reviews **12**(2): 579-594.

Dice, L. R. (1945). "Measures of the amount of ecologic association between species." Ecology **26**(3): 297-302.

Dodero, L., M. Damiano, A. Galbusera, A. Bifone, S. A. Tsaftsaris, M. L. Scattoni and A. Gozzi (2013). "Neuroimaging evidence of major morpho-anatomical and functional abnormalities in the BTBR T+ TF/J mouse model of autism." PLoS One **8**(10): e76655.

Dorr, A. E., J. P. Lerch, S. Spring, N. Kabani and R. M. Henkelman (2008). "High resolution three-dimensional brain atlas using an average magnetic resonance image of 40 adult C57Bl/6J mice." Neuroimage **42**(1): 60-69.

Driscoll, I., S. Howard, J. Stone, M. Monfils, B. Tomanek, W. Brooks and R. Sutherland (2006). "The aging hippocampus: a multi-level analysis in the rat." Neuroscience **139**(4): 1173-1185.

Dullemeijer, C., J. Durga, I. A. Brouwer, O. van de Rest, F. J. Kok, R.-J. M. Brummer, M. P. van Boxtel and P. Verhoef (2007). "n− 3 Fatty acid proportions in plasma and cognitive performance in older adults." The American journal of clinical nutrition **86**(5): 1479-1485.

Dyall, S. C. (2015). "Long-chain omega-3 fatty acids and the brain: a review of the independent and shared effects of EPA, DPA and DHA." Frontiers in aging neuroscience **7**: 52.

Ellegood, J., B. A. Babineau, R. M. Henkelman, J. P. Lerch and J. N. Crawley (2013). "Neuroanatomical analysis of the BTBR mouse model of autism using magnetic resonance imaging and diffusion tensor imaging." NeuroImage **70**: 288-300.

Erickson, K. I., D. L. Miller and K. A. Roecklein (2012). "The aging hippocampus interactions between exercise, depression, and BDNF." The Neuroscientist **18**(1): 82-97.

Evans, A. C. (2013). "Networks of anatomical covariance." Neuroimage **80**: 489-504.

Eyler, L. T., E. Prom-Wormley, C. Fennema-Notestine, M. S. Panizzon, M. C. Neale, T. L. Jernigan, B. Fischl, C. E. Franz, M. J. Lyons and A. Stevens (2011). "Genetic patterns of correlation among subcortical volumes in humans: results from a magnetic resonance imaging twin study." Human brain mapping **32**(4): 641-653.

Fedorova, I. and N. Salem (2006). "Omega-3 fatty acids and rodent behavior." Prostaglandins, leukotrienes and essential fatty acids **75**(4): 271-289.

Folch, J., M. Lees and G. Sloane-Stanley (1957). "A simple method for the isolation and purification of total lipids from animal tissues." J biol Chem **226**(1): 497-509.

Freeman, M. P., J. R. Hibbeln, K. L. Wisner, J. M. Davis, D. Mischoulon, M. Peet, P. E. Keck

Jr, L. B. Marangell, A. J. Richardson and J. Lake (2006). "Omega-3 fatty acids: evidence basis for treatment and future research in psychiatry." Journal of Clinical Psychiatry **67**(12): 1954-1967.

Freund-Levi, Y., M. Eriksdotter-Jönhagen, T. Cederholm, H. Basun, G. Faxen-Irving, A. Garlind, I. Vedin, B. Vessby, L.-O. Wahlund and J. Palmblad (2006). "ω-3 fatty acid treatment in 174 patients with mild to moderate Alzheimer disease: OmegAD Study: a randomized double-blind trial." Archives of neurology **63**(10): 1402-1408.

Friston, K. J., A. P. Holmes, K. J. Worsley, J. P. Poline, C. D. Frith and R. S. Frackowiak (1994). "Statistical parametric maps in functional imaging: a general linear approach." Human brain mapping **2**(4): 189-210.

Geleijnse, J. M., E. J. Giltay and D. Kromhout (2012). "Effects of n-3 fatty acids on cognitive decline: a randomized, double-blind, placebo-controlled trial in stable myocardial infarction patients." Alzheimer's & Dementia **8**(4): 278-287.

Gómez-Pinilla, F. (2008). "Brain foods: the effects of nutrients on brain function." Nature Reviews Neuroscience **9**(7): 568-578.

Gong, G., Y. He, Z. J. Chen and A. C. Evans (2012). "Convergence and divergence of thickness correlations with diffusion connections across the human cerebral cortex." Neuroimage **59**(2): 1239-1248.

Good, C. D., I. S. Johnsrude, J. Ashburner, R. N. Henson, K. Fristen and R. S. Frackowiak (2003). A voxel-based morphometric study of ageing in 465 normal adult human brains. Biomedical Imaging, 2002. 5th IEEE EMBS International Summer School on, IEEE.

Gozzi, A., V. Crestan, G. Turrini, M. Clemens and A. Bifone (2010). "Antagonism at serotonin 5-HT2A receptors modulates functional activity of frontohippocampal circuit." Psychopharmacology **209**(1): 37-50.

Hayasaka, S. and T. E. Nichols (2003). "Validating cluster size inference: random field and permutation methods." Neuroimage **20**(4): 2343-2356.

He, Y., Z. Chen and A. Evans (2008). "Structural insights into aberrant topological patterns of large-scale cortical networks in Alzheimer's disease." The Journal of Neuroscience **28**(18): 4756-4766.

He, Y., Z. J. Chen and A. C. Evans (2007). "Small-world anatomical networks in the human brain revealed by cortical thickness from MRI." Cerebral Cortex **17**(10): 2407-2419.

Heine, L., A. Soddu, F. Gómez, A. Vanhaudenhuyse, L. Tshibanda, M. Thonnard, V. Charland-Verville, M. Kirsch, S. Laureys and A. Demertzi (2012). "Resting state networks and consciousness." Frontiers in psychology **3**: 295.

Holmes, A. P., R. Blair, J. Watson and I. Ford (1996). "Nonparametric analysis of statistic images from functional mapping experiments." Journal of Cerebral Blood Flow & Metabolism **16**(1): 7-22.

Hooijmans, C. R., P. Pasker-de Jong, R. de Vries and M. Ritskes-Hoitinga (2012). "The effects of long-term omega-3 fatty acid supplementation on cognition and Alzheimer's pathology in animal models of Alzheimer's disease: a systematic review and meta-analysis." Journal of Alzheimer's Disease **28**(1): 191-209.

Hoover, W. B. and R. P. Vertes (2007). "Anatomical analysis of afferent projections to the medial prefrontal cortex in the rat." Brain Structure and Function **212**(2): 149-179.

Hutton, C., E. De Vita, J. Ashburner, R. Deichmann and R. Turner (2008). "Voxel-based cortical thickness measurements in MRI." NeuroImage **40**(4): 1701-1710.

Jednorog, K., A. Marchewka, I. Altarelli, A. K. Monzalvo Lopez, M. van Ermingen-Marbach, M. Grande, A. Grabowska, S. Heim and F. Ramus (2015). "How reliable are gray matter disruptions in specific reading disability across multiple countries and languages? insights from a large-scale voxel-based morphometry study." Human brain mapping **36**(5): 1741-1754.

Jenkinson, M., C. F. Beckmann, T. E. Behrens, M. W. Woolrich and S. M. Smith (2012). "Fsl." NeuroImage **62**(2): 782-790.

Jernigan, T. L., S. L. Archibald, C. Fennema-Notestine, A. C. Gamst, J. C. Stout, J. Bonner and J. R. Hesselink (2001). "Effects of age on tissues and regions of the cerebrum and cerebellum." Neurobiology of aging **22**(4): 581-594.

Jia, H., P. T. Yap, G. Wu, Q. Wang and D. Shen (2011). "Intermediate templates guided groupwise registration of diffusion tensor images." NeuroImage **54**(2): 928-939.

Jiang, L., Q. Liang and Y. Shi (2012). "Pure docosahexaenoic acid can improve depression behaviors and affect HPA axis in mice." Cellulose **50**: 50.

Johnson, G. A., A. Ali-Sharief, A. Badea, J. Brandenburg, G. Cofer, B. Fubara, S. Gewalt, L. W. Hedlund and L. Upchurch (2007). "High-throughput morphologic phenotyping of the mouse brain with magnetic resonance histology." NeuroImage **37**(1): 82-89.

Johnson, G. A., A. Badea, J. Brandenburg, G. Cofer, B. Fubara, S. Liu and J. Nissanov (2010). "Waxholm space: an image-based reference for coordinating mouse brain research." NeuroImage **53**(2): 365-372.

Keers, R., I. Pedroso, G. Breen, K. J. Aitchison, P. M. Nolan, S. Cichon, M. M. Nöthen, M. Rietschel, L. C. Schalkwyk and C. Fernandes (2012). "Reduced anxiety and depression-like behaviours in the circadian period mutant mouse afterhours." PloS one **7**(6): e38263.

Kelly, C., R. Toro, A. Di Martino, C. L. Cox, P. Bellec, F. X. Castellanos and M. P. Milham (2012). "A convergent functional architecture of the insula emerges across imaging modalities." Neuroimage **61**(4): 1129-1142.

Kelly, L., B. Grehan, A. Della Chiesa, S. M. O'Mara, E. Downer, G. Sahyoun, K. A. Massey, A. Nicolaou and M. A. Lynch (2011). "The polyunsaturated fatty acids, EPA and DPA exert a protective effect in the hippocampus of the aged rat." Neurobiology of aging **32**(12): 2318. e2311-2318. e2315.

Khan, A. R., L. Wang and M. F. Beg (2015). "Unified voxel-and tensor-based morphometry (UVTBM) using registration confidence." Neurobiology of aging **36**: S60-S68.

Khundrakpam, B. S., A. Reid, J. Brauer, F. Carbonell, J. Lewis, S. Ameis, S. Karama, J. Lee, Z. Chen and S. Das (2013). "Developmental changes in organization of structural brain networks." Cerebral Cortex **23**(9): 2072-2085.

Kim, J., B. Avants, S. Patel, J. Whyte, B. H. Coslett, J. Pluta, J. A. Detre and J. C. Gee (2008). "Structural consequences of diffuse traumatic brain injury: a large deformation tensor-based morphometry study." NeuroImage **39**(3): 1014-1026.

Klein, A., J. Andersson, B. A. Ardekani, J. Ashburner, B. Avants, M.-C. Chiang, G. E. Christensen, D. L. Collins, J. Gee and P. Hellier (2009). "Evaluation of 14 nonlinear deformation algorithms applied to human brain MRI registration." NeuroImage **46**(3): 786-

802.

Klein, A., S. S. Ghosh, B. Avants, B. T. Yeo, B. Fischl, B. Ardekani, J. C. Gee, J. J. Mann and R. V. Parsey (2010). "Evaluation of volume-based and surface-based brain image registration methods." NeuroImage **51**(1): 214-220.

Kotani, S., E. Sakaguchi, S. Warashina, N. Matsukawa, Y. Ishikura, Y. Kiso, M. Sakakibara, T. Yoshimoto, J. Guo and T. Yamashima (2006). "Dietary supplementation of arachidonic and docosahexaenoic acids improves cognitive dysfunction." Neuroscience research **56**(2): 159-164.

Kovacevic, N., J. T. Henderson, E. Chan, N. Lifshitz, J. Bishop, A. C. Evans, R. M. Henkelman and X. J. Chen (2005). "A three-dimensional MRI atlas of the mouse brain with estimates of the average and variability." Cereb Cortex **15**(5): 639-645.

Kröger, E., R. Verreault, P.-H. Carmichael, J. Lindsay, P. Julien, É. Dewailly, P. Ayotte and D. Laurin (2009). "Omega-3 fatty acids and risk of dementia: the Canadian Study of Health and Aging." The American journal of clinical nutrition **90**(1): 184-192.

Kubera, K. M., F. Sambataro, N. Vasic, N. D. Wolf, K. Frasch, D. Hirjak, P. A. Thomann and R. C. Wolf (2014). "Source-based morphometry of gray matter volume in patients with schizophrenia who have persistent auditory verbal hallucinations." Progress in Neuro-Psychopharmacology and Biological Psychiatry **50**: 102-109.

Labrousse, V. F., A. Nadjar, C. Joffre, L. Costes, A. Aubert, S. Gregoire, L. Bretillon and S. Laye (2012). "Short-term long chain omega3 diet protects from neuroinflammatory processes and memory impairment in aged mice." PloS one **7**(5): e36861.

Lang, U. E. and S. Borgwardt (2013). "Molecular mechanisms of depression: perspectives on new treatment strategies." Cellular Physiology and Biochemistry **31**(6): 761-777.

Lassi, G., L. Priano, S. Maggi, C. Garcia-Garcia, E. Balzani, N. El-Assawy, M. Pagani, F. Tinarelli, D. Giardino and A. Mauro (2016). "Deletion of the Snord116/SNORD116 alters sleep in mice and patients with Prader-Willi syndrome." Sleep **9**(3): 637-644.

Lee, D., S. Ruffins, Q. Ng, N. Sane, S. Anderson and A. Toga (2010). "MBAT: a scalable informatics system for unifying digital atlasing workflows." BMC Bioinformatics **11**(608): 1471-2105.

Lee, J., C. Ehlers, F. Crews, M. Niethammer, F. Budin, B. Paniagua, K. Sulik, J. Johns, M. Styner and I. Oguz (2011). "Automatic cortical thickness analysis on rodent brain." Proc Soc Photo Opt Instrum Eng **15**: 7962481-79624811.

Lerch, J. P., J. B. Carroll, A. Dorr, S. Spring, A. C. Evans, M. R. Hayden, J. G. Sled and R. M. Henkelman (2008). "Cortical thickness measured from MRI in the YAC128 mouse model of Huntington's disease." NeuroImage **41**(2): 243-251.

Lerch, J. P., L. Gazdzinski, J. Germann, J. G. Sled, R. M. Henkelman and B. J. Nieman (2012). "Wanted dead or alive? The tradeoff between in-vivo versus ex-vivo MR brain imaging in the mouse." Front Neuroinform **6**: 6.

Lerch, J. P., J. G. Sled and R. M. Henkelman (2011). MRI phenotyping of genetically altered mice. Magnetic Resonance Neuroimaging, Springer**:** 349-361.

Lerch, J. P., K. Worsley, W. P. Shaw, D. K. Greenstein, R. K. Lenroot, J. Giedd and A. C. Evans (2006). "Mapping anatomical correlations across cerebral cortex (MACACC) using cortical thickness from MRI." Neuroimage **31**(3): 993-1003.

Lerch, J. P., A. P. Yiu, A. Martinez-Canabal, T. Pekar, V. D. Bohbot, P. W. Frankland, R. M. Henkelman, S. A. Josselyn and J. G. Sled (2011). "Maze training in mice induces MRI-detectable brain shape changes specific to the type of learning." Neuroimage **54**(3): 2086-2095.

Li, Q., C. Cheung, R. Wei, E. S. Hui, J. Feldon, U. Meyer, S. Chung, S. E. Chua, P. C. Sham and E. X. Wu (2009). "Prenatal immune challenge is an environmental risk factor for brain and behavior change relevant to schizophrenia: evidence from MRI in a mouse model." PLoS One **4**(7): e6354.

Liska, A., A. Galbusera, A. J. Schwarz and A. Gozzi (2015). "Functional connectivity hubs of the mouse brain." Neuroimage.

Luchtman, D. W. and C. Song (2013). "Cognitive enhancement by omega-3 fatty acids from child-hood to old age: findings from animal and clinical studies." Neuropharmacology **64**: 550-565.

Lynch, A. M., D. J. Loane, A. M. Minogue, R. M. Clarke, D. Kilroy, R. E. Nally, Ó. J. Roche, F. O'Connell and M. A. Lynch (2007). "Eicosapentaenoic acid confers neuroprotection in the amyloid-β challenged aged hippocampus." Neurobiology of aging **28**(6): 845-855.

Ma, Y., D. Smith, P. R. Hof, B. Foerster, S. Hamilton, S. J. Blackband, M. Yu and H. Benveniste (2008). "In Vivo 3D Digital Atlas Database of the Adult C57BL/6J Mouse Brain by Magnetic Resonance Microscopy." Front Neuroanat **2**(1).

Maher, F., D. Martin and M. Lynch (2004). "Increased IL-1β in cortex of aged rats is accompanied by downregulation of ERK and PI-3 kinase." Neurobiology of aging **25**(6): 795-806.

Maheswaran, S., H. Barjat, S. T. Bate, P. Aljabar, D. L. Hill, L. Tilling, N. Upton, M. F. James, J. V. Hajnal and D. Rueckert (2009). "Analysis of serial magnetic resonance images of mouse brains using image registration." NeuroImage **44**(3): 692-700.

Maheswaran, S., H. Barjat, D. Rueckert, S. T. Bate, D. R. Howlett, L. Tilling, S. C. Smart, A. Pohlmann, J. C. Richardson, T. Hartkens, D. L. Hill, N. Upton, J. V. Hajnal and M. F. James (2009). "Longitudinal regional brain volume changes quantified in normal aging and Alzheimer's APP x PS1 mice using MRI." Brain Res **13**: 19-32.

Martin, D. S., P. E. Lonergan, B. Boland, M. P. Fogarty, M. Brady, D. F. Horrobin, V. A. Campbell and M. A. Lynch (2002). "Apoptotic changes in the aged brain are triggered by interleukin-1β-induced activation of p38 and reversed by treatment with eicosapentaenoic acid." Journal of Biological Chemistry **277**(37): 34239-34246.

Maruszak, A., A. Pilarski, T. Murphy, N. Branch and S. Thuret (2014). "Hippocampal neurogenesis in Alzheimer's disease: is there a role for dietary modulation?" Journal of Alzheimer's Disease **38**(1): 11-38.

Masliah, E., L. Crews and L. Hansen (2006). "Synaptic remodeling during aging and in Alzheimer's disease." Journal of Alzheimer's Disease **9**(3 Supplement): 91-99.

Mechelli, A., K. J. Friston, R. S. Frackowiak and C. J. Price (2005). "Structural covariance in the human cortex." The Journal of Neuroscience **25**(36): 8303-8310.

Minervini, M., C. Rusu, M. Damiano, V. Tucci, A. Bifone, A. Gozzi and S. A. Tsaftaris (2014). "Large-scale analysis of neuroimaging data on commercial clouds with content-aware resource allocation strategies." International Journal of High Performance Computing

Applications: 1094342013519483.

Modinos, G., S. G. Costafreda, M.-J. van Tol, P. K. McGuire, A. Aleman and P. Allen (2013). "Neuroanatomy of auditory verbal hallucinations in schizophrenia: a quantitative meta-analysis of voxel-based morphometry studies." Cortex **49**(4): 1046-1055.

Montembeault, M., S. Joubert, J. Doyon, J. Carrier, J.-F. Gagnon, O. Monchi, O. Lungu, S. Belleville and S. M. Brambati (2012). "The impact of aging on gray matter structural covariance networks." Neuroimage **63**(2): 754-759.

Mueller, S., D. Keeser, M. F. Reiser, S. Teipel and T. Meindl (2012). "Functional and structural MR imaging in neuropsychiatric disorders, part 2: application in schizophrenia and autism." AJNR Am J Neuroradiol **33**(11): 2033-2037.

Nadler, J., S. S. Moy, G. Dold, N. Simmons, A. Perez, N. Young, R. Barbaro, J. Piven, T. Magnuson and J. Crawley (2004). "Automated apparatus for quantitation of social approach behaviors in mice." Genes, Brain and Behavior **3**(5): 303-314.

Nakamoto, K., T. Nishinaka, M. Mankura, W. Fujita-Hamabe and S. Tokuyama (2010). "Antinociceptive effects of docosahexaenoic acid against various pain stimuli in mice." Biological and Pharmaceutical Bulletin **33**(6): 1070-1072.

Nestler, E. J. and S. E. Hyman (2010). "Animal models of neuropsychiatric disorders." Nat Neurosci **13**(10): 1161-1169.

Nichols, T. E. and A. P. Holmes (2002). "Nonparametric permutation tests for functional neuroimaging: a primer with examples." Human brain mapping **15**(1): 1-25.

Nieman, B. J., N. A. Bock, J. Bishop, X. J. Chen, J. G. Sled, J. Rossant and R. M. Henkelman (2005). "Magnetic resonance imaging for detection and analysis of mouse phenotypes." NMR Biomed **18**(7): 447-468.

Oarada, M., T. Tsuzuki, T. Gonoi, M. Igarashi, K. Kamei, T. Nikawa, K. Hirasaka, T. Ogawa, T. Miyazawa and K. Nakagawa (2008). "Effects of dietary fish oil on lipid peroxidation and serum triacylglycerol levels in psychologically stressed mice." Nutrition **24**(1): 67-75.

Oguz, I. and M. Sonka (2014). "LOGISMOS-B: layered optimal graph image segmentation of multiple objects and surfaces for the brain." IEEE Trans Med Imaging **33**(6): 1220-1235.

Oh, S. W., J. A. Harris, L. Ng, B. Winslow, N. Cain, S. Mihalas, Q. Wang, C. Lau, L. Kuan and A. M. Henry (2014). "A mesoscale connectome of the mouse brain." Nature **508**(7495): 207-214.

Pagani, M., A. Bifone and A. Gozzi (2016). "Structural covariance networks in the mouse brain." Neuroimage.

Pagani, M., M. Damiano, A. Galbusera, S. A. Tsaftaris and A. Gozzi (2016). "Semi-automated registration-based anatomical labelling, voxel based morphometry and cortical thickness mapping of the mouse brain." Journal of neuroscience methods **267**: 62-73.

Patrick, R. P. and B. N. Ames (2015). "Vitamin D and the omega-3 fatty acids control serotonin synthesis and action, part 2: relevance for ADHD, bipolar disorder, schizophrenia, and impulsive behavior." The FASEB Journal **29**(6): 2207-2222.

Pezawas, L., A. Meyer-Lindenberg, E. M. Drabant, B. A. Verchinski, K. E. Munoz, B. S. Kolachana, M. F. Egan, V. S. Mattay, A. R. Hariri and D. R. Weinberger (2005). "5-HTTLPR polymorphism impacts human cingulate-amygdala interactions: a genetic susceptibility

mechanism for depression." Nature neuroscience **8**(6): 828-834.

Pottala, J. V., K. Yaffe, J. G. Robinson, M. A. Espeland, R. Wallace and W. S. Harris (2014). "Higher RBC EPA+ DHA corresponds with larger total brain and hippocampal volumes WHIMS-MRI Study." Neurology **82**(5): 435-442.

Puri, B., S. Counsell, G. Hamilton, A. Richardson and D. Horrobin (2001). "Eicosapentaenoic acid in treatment-resistant depression associated with symptom remission, structural brain changes and reduced neuronal phospholipid turnover." International journal of clinical practice **55**(8): 560-563.

Quinn, J. F., R. Raman, R. G. Thomas, K. Yurko-Mauro, E. B. Nelson, C. Van Dyck, J. E. Galvin, J. Emond, C. R. Jack and M. Weiner (2010). "Docosahexaenoic acid supplementation and cognitive decline in Alzheimer disease: a randomized trial." Jama **304**(17): 1903-1911.

Raji, C. A., K. I. Erickson, O. L. Lopez, L. H. Kuller, H. M. Gach, P. M. Thompson, M. Riverol and J. T. Becker (2014). "Regular fish consumption and age-related brain gray matter loss." American journal of preventive medicine **47**(4): 444-451.

Rao, J., R. Ertley, J. DeMar, S. Rapoport, R. Bazinet and H. Lee (2007). "Dietary n-3 PUFA deprivation alters expression of enzymes of the arachidonic and docosahexaenoic acid cascades in rat frontal cortex." Molecular psychiatry **12**(2): 151-157.

Reid, A. T., F. Hoffstaedter, G. Gong, A. R. Laird, P. Fox, A. C. Evans, K. Amunts and S. B. Eickhoff (2016). "A seed-based cross-modal comparison of brain connectivity measures." Brain Structure and Function: 1-21.

Renault, J. and A. Aubert (2006). "Immunity and emotions: lipopolysaccharide increases defensive behaviours and potentiates despair in mice." Brain, behavior, and immunity **20**(6): 517-526.

Riedel, G., S. Kang, D. Choi and B. Platt (2009). "Scopolamine-induced deficits in social memory in mice: reversal by donepezil." Behavioural brain research **204**(1): 217-225.

Rimol, L. M., M. S. Panizzon, C. Fennema-Notestine, L. T. Eyler, B. Fischl, C. E. Franz, D. J. Hagler, M. J. Lyons, M. C. Neale and J. Pacheco (2010). "Cortical thickness is influenced by regionally specific genetic factors." Biological psychiatry **67**(5): 493-499.

Rimol, L. M., M. S. Panizzon, C. Fennema-Notestine, L. T. Eyler, B. Fischl, C. E. Franz, D. J. Hagler, M. J. Lyons, M. C. Neale, J. Pacheco, M. E. Perry, J. E. Schmitt, M. D. Grant, L. J. Seidman, H. W. Thermenos, M. T. Tsuang, S. A. Eisen, W. S. Kremen and A. M. Dale (2010). "Cortical thickness is influenced by regionally specific genetic factors." Biol Psychiatry **67**(5): 493-499.

Ruehle, S., F. Remmers, H. Romo-Parra, F. Massa, M. Wickert, S. Wörtge, M. Häring, N. Kaiser, G. Marsicano and H.-C. Pape (2013). "Cannabinoid CB1 receptor in dorsal telencephalic glutamatergic neurons: distinctive sufficiency for hippocampus-dependent and amygdala-dependent synaptic and behavioral functions." The Journal of Neuroscience **33**(25): 10264-10277.

Salimi-Khorshidi, G., S. M. Smith and T. E. Nichols (2011). "Adjusting the effect of nonstationarity in cluster-based and TFCE inference." Neuroimage **54**(3): 2006-2019.

Salmond, C., J. Ashburner, F. Vargha-Khadem, A. Connelly, D. Gadian and K. Friston (2002). "Distributional assumptions in voxel-based morphometry." Neuroimage **17**(2): 1027-1030.

Salvador, R., J. Suckling, M. R. Coleman, J. D. Pickard, D. Menon and E. Bullmore (2005). "Neurophysiological architecture of functional magnetic resonance images of human brain." Cerebral cortex **15**(9): 1332-1342.

Samieri, C., P. Maillard, F. Crivello, C. Proust-Lima, E. Peuchant, C. Helmer, H. Amieva, M. Allard, J.-F. Dartigues and S. C. Cunnane (2012). "Plasma long-chain omega-3 fatty acids and atrophy of the medial temporal lobe." Neurology **79**(7): 642-650.

Sannino, S., A. Gozzi, A. Cerasa, F. Piras, D. Scheggia, F. Manago, M. Damiano, A. Galbusera, L. C. Erickson, D. De Pietri Tonelli, A. Bifone, S. A. Tsaftaris, C. Caltagirone, D. R. Weinberger, G. Spalletta and F. Papaleo (2014). "COMT Genetic Reduction Produces Sexually Divergent Effects on Cortical Anatomy and Working Memory in Mice and Humans." Cereb Cortex **21**: 21.

Sawiak, S., N. Wood, G. Williams, A. Morton and T. Carpenter (2009). SPMMouse: A new toolbox for SPM in the animal brain. ISMRM 17th Scientific Meeting & Exhibition, April.

Sawiak, S. J., N. I. Wood, G. B. Williams, A. J. Morton and T. A. Carpenter (2013). "Voxel-based morphometry with templates and validation in a mouse model of Huntington's disease." Magnetic Resonance Imaging **31**(9): 1522-1531.

Schipper, P., A. J. Kiliaan and J. R. Homberg (2011). "A mixed polyunsaturated fatty acid diet normalizes hippocampal neurogenesis and reduces anxiety in serotonin transporter knockout rats." Behavioural pharmacology **22**(4): 324-334.

Schmitt, J., R. Lenroot, G. Wallace, S. Ordaz, K. Taylor, N. Kabani, D. Greenstein, J. Lerch, K. Kendler and M. Neale (2008). "Identification of genetically mediated cortical networks: a multivariate study of pediatric twins and siblings." Cerebral Cortex **18**(8): 1737-1747.

Schmitt, J. E., R. K. Lenroot, S. E. Ordaz, G. L. Wallace, J. P. Lerch, A. C. Evans, E. C. Prom, K. S. Kendler, M. C. Neale and J. N. Giedd (2009). "Variance decomposition of MRI-based covariance maps using genetically informative samples and structural equation modeling." Neuroimage **47**(1): 56-64.

Seeley, W. W., V. Menon, A. F. Schatzberg, J. Keller, G. H. Glover, H. Kenna, A. L. Reiss and M. D. Greicius (2007). "Dissociable intrinsic connectivity networks for salience processing and executive control." The Journal of Neuroscience **27**(9): 2349-2356.

Sforazzini, F., A. Bertero, L. Dodero, G. David, A. Galbusera, M. L. Scattoni, M. Pasqualetti and A. Gozzi (2016). "Altered functional connectivity networks in acallosal and socially impaired BTBR mice." Brain Structure and Function **221**(2): 941-954.

Sforazzini, F., A. J. Schwarz, A. Galbusera, A. Bifone and A. Gozzi (2014). "Distributed BOLD and CBV-weighted resting-state networks in the mouse brain." Neuroimage **87**: 403-415.

Shamy, J. L., C. Habeck, P. R. Hof, D. G. Amaral, S. G. Fong, M. H. Buonocore, Y. Stern, C. A. Barnes and P. R. Rapp (2011). "Volumetric correlates of spatiotemporal working and recognition memory impairment in aged rhesus monkeys." Cerebral Cortex **21**(7): 1559-1573.

Sinn, N., C. Milte and P. R. Howe (2010). "Oiling the brain: a review of randomized controlled trials of omega-3 fatty acids in psychopathology across the lifespan." Nutrients **2**(2): 128-170.

Spocter, M. A., W. D. Hopkins, A. R. Garrison, A. L. Bauernfeind, C. D. Stimpson, P. R. Hof and C. C. Sherwood (2010). "Wernicke's area homologue in chimpanzees (Pan troglodytes)

and its relation to the appearance of modern human language." Proceedings of the Royal Society of London B: Biological Sciences **277**(1691): 2165-2174.

Spreng, R. N. and G. R. Turner (2013). "Structural covariance of the default network in healthy and pathological aging." The Journal of neuroscience **33**(38): 15226-15234.

Squillace, M., L. Dodero, M. Federici, S. Migliarini, F. Errico, F. Napolitano, P. Krashia, A. Di Maio, A. Galbusera, A. Bifone, M. L. Scattoni, M. Pasqualetti, N. B. Mercuri, A. Usiello and A. Gozzi (2014). "Dysfunctional dopaminergic neurotransmission in asocial BTBR mice." Transl Psychiatry **4**: e427.

Steffens, D. C., E. Otey, G. S. Alexopoulos, M. A. Butters, B. Cuthbert, M. Ganguli, Y. E. Geda, H. C. Hendrie, R. R. Krishnan and A. Kumar (2006). "Perspectives on depression, mild cognitive impairment, and cognitive decline." Archives of general psychiatry **63**(2): 130-138.

Su, K.-P. (2009). "Biological Mechanism of Antidepressant Effect of Omega–3 Fatty Acids: How Does Fish Oil Act as a 'Mind-Body Interface'?" Neurosignals **17**(2): 144-152.

Sublette, M. E., S. P. Ellis, A. L. Geant and J. J. Mann (2011). "Meta-analysis of the effects of eicosapentaenoic acid (EPA) in clinical trials in depression." The Journal of clinical psychiatry **72**(12): 1577-1584.

Szulc, K. U., J. P. Lerch, B. J. Nieman, B. B. Bartelle, M. Friedel, G. A. Suero-Abreu, C. Watson, A. L. Joyner and D. H. Turnbull (2015). "4D MEMRI atlas of neonatal FVB/N mouse brain development." Neuroimage.

Tan, Z., W. Harris, A. Beiser, R. Au, J. Himali, S. Debette, A. Pikula, C. DeCarli, P. Wolf and R. Vasan (2012). "Red blood cell omega-3 fatty acid levels and markers of accelerated brain aging." Neurology **78**(9): 658-664.

Teles-Grilo Ruivo, L. and J. Mellor (2013). "Cholinergic modulation of hippocampal network function." Frontiers in Synaptic Neuroscience **5**.

Thomas, C. and C. I. Baker (2013). "Teaching an adult brain new tricks: a critical review of evidence for training-dependent structural plasticity in humans." Neuroimage **73**: 225-236.

Titova, O. E., P. Sjögren, S. J. Brooks, J. Kullberg, E. Ax, L. Kilander, U. Riserus, T. Cederholm, E.-M. Larsson and L. Johansson (2013). "Dietary intake of eicosapentaenoic and docosahexaenoic acids is linked to gray matter volume and cognitive function in elderly." Age **35**(4): 1495-1505.

Trépanier, M.-O., K. E. Hopperton, S. K. Orr and R. P. Bazinet (2015). "N-3 polyunsaturated fatty acids in animal models with neuroinflammation: An update." European journal of pharmacology.

Tucci, V., T. Kleefstra, A. Hardy, I. Heise, S. Maggi, M. H. Willemsen, H. Hilton, C. Esapa, M. Simon, M. T. Buenavista, L. J. McGuffin, L. Vizor, L. Dodero, S. Tsaftaris, R. Romero, W. N. Nillesen, L. E. Vissers, M. J. Kempers, A. T. Vulto-van Silfhout, Z. Iqbal, M. Orlando, A. Maccione, G. Lassi, P. Farisello, A. Contestabile, F. Tinarelli, T. Nieus, A. Raimondi, B. Greco, D. Cantatore, L. Gasparini, L. Berdondini, A. Bifone, A. Gozzi, S. Wells and P. M. Nolan (2014). "Dominant beta-catenin mutations cause intellectual disability with recognizable syndromic features." J Clin Invest **124**(4): 1468-1482.

Tustison, N. J., P. A. Cook, A. Klein, G. Song, S. R. Das, J. T. Duda, B. M. Kandel, N. van Strien, J. R. Stone and J. C. Gee (2014). "Large-scale evaluation of ANTs and FreeSurfer cortical thickness measurements." Neuroimage **99**: 166-179.

Tyszka, J. M., D. P. Kennedy, R. Adolphs and L. K. Paul (2011). "Intact bilateral resting-state networks in the absence of the corpus callosum." The Journal of Neuroscience **31**(42): 15154-15162.

Ullmann, J. F., C. Watson, A. L. Janke, N. D. Kurniawan and D. C. Reutens (2013). "A segmentation protocol and MRI atlas of the C57BL/6J mouse neocortex." NeuroImage **78**: 196-203.

Valk, S. L., A. Di Martino, M. P. Milham and B. C. Bernhardt (2015). "Multicenter mapping of structural network alterations in autism." Human brain mapping **36**(6): 2364-2373.

van de Rest, O., J. M. Geleijnse, F. J. Kok, W. A. van Staveren, C. Dullemeijer, M. G. OldeRikkert, A. T. Beekman and C. De Groot (2008). "Effect of fish oil on cognitive performance in older subjects A randomized, controlled trial." Neurology **71**(6): 430-438.

Varteresian, T. and H. Lavretsky (2014). "Natural products and supplements for geriatric depression and cognitive disorders: an evaluation of the research." Current psychiatry reports **16**(8): 1-9.

Videbech, P. and B. Ravnkilde (2004). "Hippocampal volume and depression: a meta-analysis of MRI studies." American Journal of Psychiatry **161**(11): 1957-1966.

Vinot, N., M. Jouin, A. Lhomme-Duchadeuil, P. Guesnet, J.-M. Alessandri, F. Aujard and F. Pifferi (2011). "Omega-3 fatty acids from fish oil lower anxiety, improve cognitive functions and reduce spontaneous locomotor activity in a non-human primate." PloS one **6**(6): e20491.

Virtanen, J. K., D. S. Siscovick, R. N. Lemaitre, W. T. Longstreth, D. Spiegelman, E. B. Rimm, I. B. King and D. Mozaffarian (2013). "Circulating omega-3 polyunsaturated fatty acids and subclinical brain abnormalities on MRI in older adults: the Cardiovascular Health Study." Journal of the American Heart Association **2**(5): e000305.

Vu, N. Q. and H. J. Aizenstein (2013). "Depression in the elderly: brain correlates, neuropsychological findings, and role of vascular lesion load." Current opinion in neurology **26**(6): 656-661.

Whalley, L. J., I. J. Deary, J. M. Starr, K. W. Wahle, K. A. Rance, V. J. Bourne and H. C. Fox (2008). "n–3 Fatty acid erythrocyte membrane content, APOE ε4, and cognitive variation: an observational follow-up study in late adulthood." The American journal of clinical nutrition **87**(2): 449-454.

White, L., T. Andrews, C. Hulette, A. Richards, M. Groelle, J. Paydarfar and D. Purves (1997). "Structure of the human sensorimotor system. II: Lateral symmetry." Cerebral Cortex **7**(1): 31-47.

Willis, L. M., B. Shukitt-Hale and J. A. Joseph (2009). "Dietary polyunsaturated fatty acids improve cholinergic transmission in the aged brain." Genes & nutrition **4**(4): 309-314.

Winkler, A. M., G. R. Ridgway, M. A. Webster, S. M. Smith and T. E. Nichols (2014). "Permutation inference for the general linear model." Neuroimage **92**: 381-397.

Winters, B. D. and T. J. Bussey (2005). "Removal of cholinergic input to perirhinal cortex disrupts object recognition but not spatial working memory in the rat." European Journal of Neuroscience **21**(8): 2263-2270.

Witte, A. V., L. Kerti, H. M. Hermannstädter, J. B. Fiebach, S. J. Schreiber, J. P. Schuchardt, A. Hahn and A. Flöel (2013). "Long-chain omega-3 fatty acids improve brain function and structure in older adults." Cerebral Cortex: bht163.

Worsley, K. J., A. C. Evans, S. Marrett and P. Neelin (1992). "A three-dimensional statistical analysis for CBF activation studies in human brain." Journal of Cerebral Blood Flow & Metabolism **12**(6): 900-918.

Wu, K.-L. and M.-S. Yang (2005). "A cluster validity index for fuzzy clustering." Pattern Recognition Letters **26**(9): 1275-1291.

Xie, Z., D. Yang, D. Stephenson, D. Morton, C. Hicks, T. Brown and T. Bocan (2010). "Characterizing the regional structural difference of the brain between tau transgenic (rTg4510) and wild-type mice using MRI." Med Image Comput Comput Assist Interv **13**(Pt 1): 308-315.

Xu, L., K. M. Groth, G. Pearlson, D. J. Schretlen and V. D. Calhoun (2009). "Source-based morphometry: The use of independent component analysis to identify gray matter differences with application to schizophrenia." Human brain mapping **30**(3): 711-724.

Yehuda, S. (2012). "Polyunsaturated fatty acids as putative cognitive enhancers." Medical hypotheses **79**(4): 456-461.

Yehuda, S., S. Rabinovitz, R. L. Carasso and D. I. Mostofsky (2002). "The role of polyunsaturated fatty acids in restoring the aging neuronal membrane." Neurobiology of aging **23**(5): 843-853.

Yurko-Mauro, K., D. McCarthy, D. Rom, E. B. Nelson, A. S. Ryan, A. Blackwell, N. Salem, M. Stedman and M. Investigators (2010). "Beneficial effects of docosahexaenoic acid on cognition in age-related cognitive decline." Alzheimer's & Dementia **6**(6): 456-464.

Yushkevich, P. A., J. Piven, H. C. Hazlett, R. G. Smith, S. Ho, J. C. Gee and G. Gerig (2006). "User-guided 3D active contour segmentation of anatomical structures: significantly improved efficiency and reliability." NeuroImage **31**(3): 1116-1128.

Zhang, J., Q. Peng, Q. Li, N. Jahanshad, Z. Hou, M. Jiang, N. Masuda, D. R. Langbehn, M. I. Miller, S. Mori, C. A. Ross and W. Duan (2010). "Longitudinal characterization of brain atrophy of a Huntington's disease mouse model by automated morphological analyses of magnetic resonance images." NeuroImage **49**(3): 2340-2351.

Zielinski, B. A., J. S. Anderson, A. L. Froehlich, M. B. Prigge, J. A. Nielsen, J. R. Cooperrider, A. N. Cariello, P. T. Fletcher, A. L. Alexander and N. Lange (2012). "scMRI reveals large-scale brain network abnormalities in autism." PloS one **7**(11): e49172.

Zielinski, B. A., E. D. Gennatas, J. Zhou and W. W. Seeley (2010). "Network-level structural covariance in the developing brain." Proceedings of the National Academy of Sciences **107**(42): 18191-18196.

7. Publication List

Published Manuscripts

[1] **Pagani M**, Bifone A, Gozzi A (2016). Networks of anatomical covariance in the mouse brain, NeuroImage, 129:55-63.

[2] **Pagani M**, Damiano M, Galbusera A, Tsaftaris SA, Gozzi A (2016). Semi-automated registration-based anatomical labelling, voxel based morphometry and cortical thickness mapping of the mouse brain, J Neurosci Methods, 11:62-73.

[3] Cutuli D, **Pagani M**, Caporali P, Galbusera A, Laricchiuta D, Foti F, Neri C, Spalletta G, Caltagirone C, Petrosini L, Gozzi A. (2016). Effects of omega-3 fatty acid supplementation on cognitive functions and neural substrates: a voxel-based morphometry study in aged mice, Front Aging Neurosci, 4:8-38.

[4] Lassi G, Priano L, Maggi S, Garcia-Garcia C, Balzani E, El-Assawy N, **Pagani M**, Tinarelli F, Giardino D, Mauro A, Peters J, Gozzi A, Grugni G, Tucci V. (2015). Deletion of Snord116 Alters Sleep in Mice and Patients with Prader-Willi Syndrome. Sleep, 39:637-44.

Submitted Manuscript

[5] **Pagani M**, Galbusera A, Gozzi A (2017). Aberrant striatal anatomy and gray matter connectivity networks in mice lacking autism-associated gene CNTANP2.

[6] Pucilowska J, Vithayathil J, **Pagani M**, Kelly C, Karlo JC, Robol C, Brambilla R, Gozzi A, and Landreth GE (2017). Pharmacological inhibition of ERK Rescues Pathophysiology associated with 16p11.2 Chromosomal Deletion in Mice.

[7] Michetti C, Caruso A, **Pagani M**, Sabbioni M, Medrihan L, David G, Galbusera A, Morini M, Gozzi A, Benfenati F and Scattoni ML. Differential effects of Synapsins I-II and III on ASD-like phenotype.

[8] Sannino S., Padula MC, Manago' F, Schaer M, Schneider M, Scariati E, Sloan-Bena F, Mereu M, Contarini G, **Pagani M**, Gozzi A, Eliez S, Papaleo F (2017). Sex-dichotomous COMT genetic effects start to appear in adolescence: a translational study in 22q11.2DS patients and COMT knockout mice.

Conference Proceedings

[9] **Pagani M**, Damiano M, Galbusera A, Tsaftaris SA, Gozzi A (2016). An automated pipeline for mouse brain morphometric MRI. 24th Annual Meeting of the ISMRM, Singapore (SGP).

[10] **Pagani M**, Bifone A, Gozzi A (2016). Gray matter networks of the mouse brain. 24th Annual Meeting of the ISMRM, Singapore (SGP).

[11] Bertero A, **Pagani M**, David G, Liska A, Galbusera A, Pasqualetti M, Gozzi A (2016). Default-mode network hypo-connectivity in a mouse model of human chromosome 16p11.2 micro-deletion. ISMRM, 24th Annual Meeting of the ISMRM, Singapore (SGP).

[12] Pesoli M, Cutuli D, **Pagani M**, Caporali P, Galbusera A, Laricchiuta D, Foti F, Neri C, Spalletta G, Caltagirone C, Petrosini L, Gozzi A (2016). Effects of omega-3 fatty acid supplementation on cognitive functions and neural substrates: a voxel-based morphometry study in aged mice. 10th FENS Forum of Neuroscience, Copenhagen (DK)

[13] **Pagani M**, Bifone A, Gozzi A (2015). Networks of anatomical covariance of the mouse brain. 32nd Annual Meeting of the ESMRMB, Edinburgh (UK).

[14] **Pagani M**, Cutuli D, Liska A, Caporali P, Laricchiuta D, Foti F, Neri C, Petrosini L, Gozzi A (2015). Neural and cognitive substrates of omega-3 supplementation: a VBM study in aged mice. ISMRM Italian Chapter 2015 Meeting, Verona (ITA).

[15] **Pagani M**, Bifone A, Gozzi A (2015). Structural covariance networks in the mouse brain. Images of the Mind, Milano (ITA).

[16] Michetti C, Morini M, Caruso A, Sabbioni M, **Pagani M**, Gergely D, Blesa M, Gozzi A, Benfenati F, Scattoni ML (2015). Behavioural and neuroanatomical characterisation of synapsin-II mouse. Congresso Nazionale della Società Italiana di Fisiologia, Genova (ITA).

[17] **Pagani M**, Cutuli D, Liska A, Caporali P, Laricchiuta D, Foti F, Neri C, Petrosini L, Gozzi A (2014). Neural and cognitive substrates of omega-3 supplementation: a VBM study in aged mice. 23rd Annual Meeting of the ISMRM, Toronto (CA).

APPENDIX A

Complete list of all the 198 VOIs used to parcellate the mouse brains and to create clusters (**Figure 34**) with similar pairwise correlation of gray matter volume

Cluster membership	Brain region	Hemisphere
A	area 29c	right
A	area 29c	left
A	medial parietal association cortex	right
A	area 30	right
A	area 30	left
A	secondary visual cortex, mediolateral area	right
A	secondary visual cortex, mediomedial area	right
A	primary visual cortex, monocular area	right
A	area 29b	right
A	area 29a	right
A	area 29b	left
A	area 29a	left
A	primary visual cortex, binocular area	right
A	secondary visual cortex, lateral part	right
A	temporal association area	right
A	secondary visual cortex, lateral part	left
A	primary visual cortex, binocular area	left
A	dorsal subiculum	right
A	dorsal subiculum	left
A	primary visual cortex	right
A	primary visual cortex	left
A	secondary visual cortex, mediomedial area	left
A	lateral parietal association cortex	left
A	primary somatosensory, trunk region	left
A	medial parietal association cortex	left
A	parietal cortex, posterior area, rostral part	left
A	lateral parietal association cortex	right
A	primary somatosensory, trunk region	right
A	parietal cortex, posterior area, rostral part	right
A	secondary auditory cortex, dorsal area	right
A	primary auditory cortex	right
A	secondary auditory cortex, ventral area	right
A	primary auditory cortex	left
A	secondary auditory cortex, dorsal area	left
A	secondary auditory cortex, ventral area	left
A	secondary visual cortex, mediolateral area	left
A	primary visual cortex, monocular area	left

A	dorsolateral entorhinal cortex	left
A	dorsal intermediate entorhinal cortex	left
B	area 24a	right
B	area 24a	left
B	ectorhinal cortex	left
B	perirhinal cortex	left
B	temporal association area	left
B	subiculum transition area	left
B	hippocampus	right
B	subiculum transition area	right
B	hippocampus	left
B	ectorhinal cortex	right
B	perirhinal cortex	right
B	parasubiculum	left
B	parasubiculum	right
B	presubiculum	right
B	postsubiculum	left
B	postsubiculum	right
B	caudomedial entorhinal cortex	right
B	dentate gyrus	left
B	stratum granulosum of hippocampus	left
B	dentate gyrus	right
B	stratum granulosum of hippocampus	right
B	medial entorhinal cortex	left
B	ventral intermediate entorhinal cortex	left
B	medial entorhinal cortex	right
B	ventral intermediate entorhinal cortex	right
B	stratum lucidum of hippocampus	right
B	stratum lucidum of hippocampus	left
B	presubiculum	left
B	caudomedial entorhinal cortex	left
B	cortex-amygdala transition zones	right
B	cortex-amygdala transition zones	left
B	lateral septal nucleus	left
B	lateral septal nucleus	right
B	dorsolateral entorhinal cortex	right
B	dorsal intermediate entorhinal cortex	right
C	primary somatosensory cortex	right
C	frontal cortex area 3	right
C	secondary motor cortex	right
C	area 24b	right
C	secondary motor cortex	left
C	area 24b	left
C	primary motor cortex	right
C	primary motor cortex	left

C	secondary somatosensory cortex	left
C	primary somatosensory, upper limb region	left
C	primary somatosensory, jaw region	left
C	primary somatosensory cortex	left
C	frontal cortex area 3	left
C	primary somatosensory, shoulder region	left
C	primary somatosensory, hindlimb region	left
C	area 24a'	left
C	area 24a'	right
C	primary somatosensory, hindlimb region	right
C	primary somatosensory, forelimb region	right
C	primary somatosensory, shoulder region	right
C	primary somatosensory, dysgranular zone	right
C	primary somatosensory, barrel field	right
C	area 24b'	left
C	area 24b'	right
C	primary somatosensory, dysgranular zone	left
C	primary somatosensory, forelimb region	left
C	primary somatosensory, barrel field	left
C	primary somatosensory, jaw region	right
C	primary somatosensory, upper limb region	right
C	dorsolateral orbital cortex	left
C	lateral orbital cortex	left
C	lateral orbital cortex	right
C	dorsolateral orbital cortex	right
C	frontal association cortex	left
C	frontal association cortex	right
C	area 32	left
C	area 32	right
C	medial orbital cortex	right
C	medial orbital cortex	left
C	ventro orbital cortex	left
C	ventro orbital cortex	right
C	claustrum, dorsal part	right
C	claustrum, ventral part	right
C	insula	right
C	secondary somatosensory cortex	right
D	caudoputamen	right
D	claustrum	left
D	piriform cortex	left
D	dorsal nucleus of the endopiriform	left
D	claustrum, ventral part	left
D	claustrum, dorsal part	left
D	insula	left
D	area 25	right

D	area 25	left
D	dorsal tenia tecta	right
D	dorsal tenia tecta	left
D	ventral nucleus of the endopiriform claustrum	left
D	amygdala	right
D	ventral nucleus of the endopiriform claustrum	right
D	intermediate nucleus of the endopiriform claustrum	left
D	accumbens nucleus, shell	right
D	nucleus accumbens, core	right
D	bed nucleus of the stria terminalis	left
D	bed nucleus of the stria terminalis	right
D	medial septal nucleus	left
D	medial septal nucleus	right
D	basal forebrain	right
D	thalamus	right
D	thalamus	left
D	globus pallidus	right
D	piriform cortex	right
D	dorsal nucleus of the endopiriform	right
D	amygdala	left
D	caudoputamen	left
D	claustrum	right
D	intermediate nucleus of the endopiriform claustrum	right
D	accumbens nucleus, shell	left
D	nucleus accumbens, core	left
D	globus pallidus	left
D	basal forebrain	left
D	hypothalamus	right
D	hypothalamus	left
D	midbrain	left
D	midbrain	right
D	mammillary bodies	right
D	mammillary bodies	left
D	olfactory tubercole	left
D	interpedunclar nucleus	left
D	interpedunclar nucleus	right
D	olfactory tubercole	right
D	ventral tenia tecta	right
D	subependymale zone rhinocele	left
D	subependymale zone rhinocele	right
D	ventral tenia tecta	left
E	olfactory bulbs	right
E	olfactory bulbs	left
E	periaqueductal gray	left
E	periaqueductal gray	right

E	superior colliculus	right
E	superior colliculus	left
E	inferior colliculus	right
E	inferior colliculus	left
E	amygdalopiriform transition area	right
E	posteromedial cortical amygdaloid nucleus	right
E	posterolateral cortical amygdaloid nucleus	right
E	rostral amigdalopiriform area	right
E	amygdalopiriform transition area	left
E	posteromedial cortical amygdaloid nucleus	left
E	posterolateral cortical amygdaloid nucleus	left
E	rostral amigdalopiriform area	left
F	cerebellar cortex	right
F	cerebellar cortex	left
F	pontine nucleus	left
F	pontine nucleus	right
F	superior olivary complex	left
F	superior olivary complex	right
F	pons	left
F	pons	right
F	cuneate nucleus	right
F	cuneate nucleus	left
F	inferior olivary complex	right
F	inferior olivary complex	left
F	medulla	left
F	medulla	right